

**FIRST-PRINCIPLES STUDY OF
ELECTROMECHANICAL AND POLAR
PROPERTIES IN PEROVSKITE OXIDES
AND HALF-HEUSLER SEMICONDUCTORS**

BY ANINDYA ROY

A dissertation submitted to the
Graduate School—New Brunswick
Rutgers, The State University of New Jersey
in partial fulfillment of the requirements
for the degree of
Doctor of Philosophy
Graduate Program in Physics and Astronomy

Written under the direction of
Professor David Vanderbilt
and approved by

New Brunswick, New Jersey

October, 2011

ABSTRACT OF THE DISSERTATION

First-principles study of electromechanical and polar properties in perovskite oxides and half-Heusler semiconductors

by Anindya Roy

Dissertation Director: Professor David Vanderbilt

This thesis discusses electromechanical and polar properties in two well-known classes of materials, perovskite oxides and half-Heusler compounds, using first-principles calculations. Certain features of the *ab initio* codes, such as the capability to calculate polarization based on the modern theory of polarization, or to apply a finite electric field, are central to the problems presented in this thesis. Hence these formalisms are discussed, following a brief opening section on the basic methodology of density-functional theory. The first problem presented in this thesis concerns the nonlinear piezoelectric response of ferroelectric PbTiO_3 for the case of a polarization-enhancing electric field applied along the tetragonal axis. The dependence of the c/a ratio on electric field is found to be almost linear in the range up to 500 MV/m, contrary to what expected from Landau-Devonshire theory, but in qualitative agreement with a recent experiment. In the

second problem we study the energy landscape and ferroelectric states of double perovskites of the form $AA'BB'O_6$ in which the atoms on both the A and B sites are arranged in rock-salt order. If a ferroelectric instability occurs, the energy landscape will tend to have minima with the polarization along tetrahedral directions, leading to a rhombohedral phase, or along Cartesian directions, leading to an orthorhombic phase. We are not aware of compounds naturally occurring in this structure, although they might be synthesized experimentally. In the final problem, we use a first-principles rational-design approach to search a large materials family, half-Heusler compounds to identify semiconductors, and then compute their piezoelectric properties. This previously-unrecognized class of piezoelectrics may benefit greatly from calculations such as those presented here. Our work may provide guidance for experimental verification of existing compounds and for the experimental realization of other potential candidates.

Acknowledgements

I consider myself exceptionally lucky to have had David Vanderbilt as my advisor. His understanding of Physics, ability as a scientist and as a teacher are well known in the community. This combination may not be so rare, but the support and the sensitivity he showed while guiding me towards my PhD, and the values he imparted in me in the process, are of the highest quality. You have set an example worth striving for, but hard to reach!

I thank all my collaborators for enriching my understanding of Physics, Karin Rabe, Massimiliano Stengel and Joseph Bennett in particular.

I would like to thank Don Hamann, Nicola Spaldin and Craig Fennie, among many others for discussions, suggestions and inspirations. I am grateful to all the current and previous group members for numerous productive group meetings and the ensuing discussions we had. I am indebted to the members of the Condensed Matter group at Rutgers and the faculty members I interacted with during my graduate courses.

I thank my parents, muni and dada (my sister-in-law and brother), and Amrita, my little niece, for letting me be so far away from them to pursue what I want. Your sacrifice and support mean a lot to me.

Finally, I would like to thank my friends and office mates: Aatish, Alex, Aline, Adina, Andrei, Bonny, Bidisha, Chioun, Chuck, Daniel, Darakhshan, Deepak, George, GJ, Hridis, John, Kasturi, Kshitij, Lizzie, Lucia, Maryam, Purba, Rebecca, Senia, Shambhavi, Sinisa, Steffen, Sushmita, Tahir, Vijay, Robin and Jenna. Your friendships and support made it all worthwhile. My graduate-school

experience wouldn't have been such a happy one without you! You enriched my life. My apologies to all whom I might have left out accidentally.

Dedication

'I am who I am because of who we all are' - Ubuntu philosophy.

I dedicate this thesis to all who made me who I am today.

Table of Contents

Abstract	ii
Acknowledgements	iv
Dedication	vi
List of Tables	ix
List of Figures	xi
1. Introduction	1
2. Preliminary ideas: density-functional theory, modern theory of polarization and related applications	3
2.1. Introduction: A quick glance at density-functional theory	3
2.2. Treatment of polarization and related concepts in DFT	11
2.3. Modern theory of polarization	12
2.4. Implementation of finite electric field formalism in DFT	23
2.5. Implementation of fixed electric displacement field formalism in DFT	29
3. First-principles study of high-field piezoelectricity in tetragonal PbTiO₃	36
3.1. Introduction	36
3.2. Computational details	40
3.3. Results	42
3.4. Summary	55

4. Theory of prospective perovskite ferroelectrics with double rock-salt order	57
4.1. Introduction	57
4.2. Tetrahedral $AA'BB'O_6$ double perovskites with rock-salt order	59
4.3. Computational details	66
4.4. Results	67
4.5. Summary	79
5. Half-Heusler semiconductors as piezoelectrics	80
5.1. Introduction	80
5.2. Structure of half-Heusler and related compounds	83
5.3. Computational details	89
5.4. Results	92
5.5. Summary	108
Bibliography	109
Appendix A.	114
Curriculum Vita	127

List of Tables

4.1. Possible cation ordering in double perovskites with examples and the corresponding high-symmetry space groups. ‘(R)’, ‘(C)’ and ‘(L)’ denote rock-salt, columnar and layered ordering in the left most column.	62
4.2. Compounds for which calculations have been carried out. Second column gives the acronym that we use to identify the compound. Lattice constants are calculated in the high-symmetry $F\bar{4}3m$ structure and are reported in terms of an effective 5-atom cubic cell dimension. “Average” refers to the average computed lattice constant of the ABO_3 , $A'BO_3$, $AB'O_3$, and $A'B'O_3$ parent materials. .	67
4.3. Frequency and principal character of lowest zone-center mode, and same for next-higher mode, in the $F\bar{4}3m$ structure for $AA'BB'O_6$ materials.	69
4.4. Calculated polarization and total-energy reduction (relative to the high-symmetry $F\bar{4}3m$ structure, per 10-atom cell) for distorted structures of CBTZ, KCZN, and PSTZ. Last four columns present results obtained from the models discussed in Sec. 4.4.3 (values in parentheses are exact by construction, as they were used as input to the fit).	70
4.5. Lattice constants, energy (relative to FM state per 20-atom unit cell) and fraction of parallel nearest-neighbor (NN) and next-nearest-neighbor (NNN) spins for three magnetic structures of $SrCaTiMnO_6$.	77

5.1.	Structure and prototypes for Half-Heusler compounds and other related compounds. Here A and D form one rocksalt sublattice, while B and C form the other rocksalt sublattice. If any site is vacant, we represent that as [X], meaning the position of X is empty.	88
5.2.	Properties of experimentally synthesized half-Heuslers, grouped by family. Experimental lattice constants are from the ICSD. Also presented are the theoretical lattice constant a , band gap E_{gap} , piezoelectric coefficient d_{14} , electromechanical coupling coefficient k_{14} , and free-stress static dielectric constant ϵ_0 .	98
5.3.	Top twelve half-Heusler compounds, ranked according to piezoelectric coefficient d_{14} .	99
5.4.	Best sixty five remaining half-Heusler compounds, ranked according to piezoelectric coefficient d_{14} . None of the initial top twelve presented in Table 5.3 remain after considering band gap, stability, cost and toxicity.	100
5.5.	List of unstable half-Heusler compounds. Phonon frequency at Γ point is not included, since in no instability is found at Γ for any of the combinations. The minimum phonon frequency is noted for the X , L and W point.	106
A.1.	Lattice parameter, band gap, Born effective charges, static dielectric constant and space group as reported in ICSD if available. The unstable combinations are marked with \dagger .	114
A.2.	Piezoelectric constant, elastic constants, lowest phonon frequency at X , L and W points, and electromechanical coupling factor. The unstable combinations are marked with \dagger .	120

List of Figures

2.1.	The flow chart showing the algorithm to perform total-energy calculation of a periodic crystal using plane-wave basis sets.	10
2.2.	Attempt to define polarization using the dipole moment of a fictitious crystal. The direction of the dipole moment is dependent on how one draws the unit cell.	13
2.3.	The periodic crystal potential energy is tilted in presence of an electric field. The total potential is aperiodic and unbounded. . .	25
2.4.	Zener tunneling and Δk . The arrow in the left half of the figure is approximately $L_t = E_g/\mathcal{E}$. The double arrow in the right half of the figure is a representative $L_p = 2\pi/\Delta k$	26
2.5.	Two methods of making a sandwich out of two materials between the electrodes/probes at the top and the bottom. In case (a) electric field and polarization field are not the same on top and at the bottom, whereas the displacement field is. In (b), displacement field and polarization field are not the same, but electric field is the same on left and right of the composite. It is assumed that there is no free charge at the interface.	30
2.6.	Showing different boundary conditions as a constant (a) electric (b) displacement and (c) polarization field is applied. While case (a) corresponds to applying a constant bias across the sample, and case (b) corresponds to an open-circuit condition, there is no immediate physical analogy to case (c).	31

3.1.	Out-of-plane strain response to applied electric field, relative to zero-field ferroelectric state, under in-plane epitaxial constraint. Experiment: data of Grigoriev et al. (2008) for several PZT 20/80 capacitors of varying thickness. Theoretical points with fitted lines: computed results for pure PbTiO_3 using two computer codes. Inset shows the ABINIT results over a more extended range of fields.	42
3.2.	Variation of properties of tetragonal PbTiO_3 with electric field under in-plane epitaxial constraint. (a) Piezoelectric coefficient d_{33} (calculated with both codes). (b) Out-of-plane displacements of ions from zero-field positions (calculated with ABINIT).	45
3.3.	Variation of properties of tetragonal PbTiO_3 with electric field under in-plane epitaxial constraint, calculated with ABINIT. (a) Born effective charges. (b) Polarization.	47
3.4.	Field-induced strain, relative to zero-field zero-pressure state, for tetragonal PbTiO_3 under in-plane epitaxial constraint, calculated with LAUTREC.	49
3.5.	Field-induced strain, relative to out-of-plane lattice constant of zero-field zero-pressure state, for tetragonal PbTiO_3 under free-stress (0 GPa) and negative-pressure (-1 and -2 GPa) boundary conditions, calculated with LAUTREC. Top curves: out-of-plane strain. Bottom curves: in-plane strain.	50
3.6.	Variation of properties of tetragonal PbTiO_3 with electric field under free-stress boundary conditions, calculated with LAUTREC. (a) Piezoelectric coefficient d_{33} . (b) Out-of-plane displacements of ions from zero-field positions.	51

4.1. Structure of AA'BB'O ₆ double perovskites, with A (red circles) and A' (magenta squares) atoms forming one rock-salt framework, and B (blue diamonds) and B' (green triangles) atoms forming a second interpenetrating one. Oxygen atoms are not shown, although one oxygen octahedron is outlined to clarify that the local bonding environment is still roughly octahedral. Dashed lines illustrate the tetrahedral point symmetry.	63
4.2. Symmetry-determined possibilities for directions of energy minima in the space of polarization, represented by red dots. Fig. (a)-(c) cubic composition leading to high-symmetry <i>Pm3m</i> structure, and (d)-(f) tetrahedral composition leading to high-symmetry <i>F43m</i> structure.	65
4.3. (a) Type-I and (b) type-II configuration of SCTM.	77
5.1. The <i>ABC</i> half-Heusler structure type: <i>A</i> (green) and <i>B</i> (orange) are arranged in a rocksalt lattice, with the tetrahedral coordination of <i>C</i> (blue) by <i>A</i> shown.	82
5.2. Green triangles denote species A, magenta squares B, and red circles C in this and subsequent figures in this section. (a) Zincblende structure and (b)-(d) three configurations of the half-Heusler structure. Compared to ZnS, there are extra red circles forming a rock-salt sublattice with magenta squares to stuff the zincblende structure into a half-Heusler structure. All belong to space group <i>F43m</i> . For underline notation, see text.	84
5.3. Two structures with the chemical formula of full-Heusler compounds: (a) <i>Fm3m</i> symmetry and (b) <i>F43m</i> symmetry. (c) Mixed-Heusler structure with <i>F43m</i> symmetry.	85

5.4.	Other variants of the same structure type. (a) Space group $Pm\bar{3}m$ (b) Space group $Fd\bar{3}m$ (c) Space group $Fm\bar{3}m$ and (d) Space group $Im\bar{3}m$	86
5.5.	Deviation of electronegativity and pseudopotential radius of the tetrahedrally coordinated species of lowest-energy configurations (red crosses) and the two higher-energy configurations (blue circles) for all nonmetallic cases.	94
5.6.	Deviation of electronegativity and pseudopotential radius of the tetrahedrally coordinated species for the lowest-energy configura- tions of insulators (red crosses) and metals (blue circles). All 792 combinations are plotted.	95
5.7.	Cell parameters (in Å) of insulating ABC combinations as well as their range of band gaps (in eV) are depicted as open black circles. Known combinations, from Table 5.2, are highlighted as filled red circles.	96
5.8.	Electromechanical coupling factor k_{14} of insulating ABC combina- tions as a function of piezoelectric constant d_{14} . Known combina- tions, from Table 5.2, are highlighted as filled red circles	96
5.9.	Deviation of electronegativity and pseudopotential radius of the tetrahedrally coordinated species for the lowest-energy configura- tions of all insulators (red crosses), the best-ranked sixty five com- binations (blue circles), and the unstable combinations (green tri- angles).	102
5.10.	Induced polarization in epitaxially constrained half-Heusler com- pounds.	105

Chapter 1

Introduction

Density-functional theory (DFT) has become an important tool for physicists, chemists and materials scientists alike. It is used to confirm experimental findings, estimate material properties when experiments are hard to perform, or even design novel materials with desired features. Among many properties that one may calculate using DFT, electromechanical and polar properties such as piezoelectricity, ferroelectricity etc. form an important subset. Many insulators exhibit these properties, and some of them find applications in devices. In this thesis, we discuss such properties for three different cases, in Chapters 3, 4 and 5. We devote chapter 2 as the necessary background required to perform calculations presented in subsequent chapters.

We begin Chapter 2 with a short introduction and mathematical summary of density-functional theory. In Sec. 2.3 we briefly discuss the modern theory of polarization, and in Sec. 2.4, the formalism for implementation of finite electric fields in *ab initio* codes. In the final section of this chapter, Sec. 2.5, the formalism for implementation of a fixed displacement field is discussed.

In Chapter 3, we present our first principles calculation of the nonlinear piezoelectric response of ferroelectric PbTiO_3 for the case of a polarization-enhancing electric field applied along the tetragonal axis. The details of our computations are described in Sec. 3.2, followed by Sec. 3.3, where we present our results and compare them with experiments. We also relax the experimental conditions, and explore further possibilities. This work is summarized in Sec. 3.4.

Chapter 4 is on our first-principles work to predict the energy landscape and ferroelectric states of double perovskites of the form $AA'BB'O_6$ in which the atoms on both the A and B sites are arranged in rock-salt order. In Sec. 4.2, we discuss various types of cation ordering in double perovskites, emphasizing the importance of the specific arrangement we have here in connection to the focus of our work. Theoretical methods and computational details are given in Sec. 4.3, followed by the main results in Sec. 4.4. In this section we also present a comparison with an empirical model, followed by consideration of some other related factors. Sec. 4.5 contains the summary and conclusions to this work.

In Chapter 5 we explore the half-Heusler class of compounds for their piezoelectric properties using first-principles methods. In Sec. 5.2 we discuss possible structural variants based on the half-Heusler structure. This is followed by details of our computational methods of this high-throughput work in Sec. 5.3. We present our results in Sec. 5.4, compare them with the known half-Heusler compounds from the Inorganic Crystal Structure Database, try to shortlist candidates which may be more useful for experimental realization, and make an attempt to understand their piezoelectric behavior in terms of electronegativity and the size of the individual constituents of the potential half-Heusler candidates. This work is summarized in Sec. 5.5.

The contents of Chapters 3, 4 and 5 are based on Roy et al. (2010), Roy & Vanderbilt (2011) and Roy et al. (2011), respectively.

Chapter 2

Preliminary ideas: density-functional theory, modern theory of polarization and related applications

2.1 Introduction: A quick glance at density-functional theory

The attempt to decode nature by studying material properties has been a fundamental feature of modern science. An ever-growing industrialized world arguably gained from this understanding, fueling further efforts to push the boundaries of our knowledge in this field. While the identification of the electron as a particle in the late nineteenth century can be regarded as the first step, real progress began with the discovery of quantum mechanics in the early 1920's. The same decade saw the development of the band theory of solids (Bloch 1929), and the first set of quantitative calculations by Hartree, Hylleraas, and soon after, by Fock (Hartree 1928; Hylleraas 1929, 1930; Fock 1930). They pioneered the idea of the self-consistent field method, where electrons are considered to move in a central potential created by other electrons and nuclei. Some of the concepts developed during this time are still in use today. Various aspects of quantum-chemistry calculations were refined in the next few decades, namely, new basis sets were constructed to deal with the electrons close to the core of the nucleus, as well as far from it, and many empirical and semi-empirical ways to model the effect of the core (consisting of the nucleus and electrons in the core region) on the valence

electrons were developed. In the majority of these methods, the wave functions of the valence electrons were the fundamental quantity to solve for, involving $3N$ position variables for an N -electron system.

A paradigm shift took place when the work of Hohenberg, Kohn and Mermin (Hohenberg & Kohn 1964; Mermin 1965) suggested that any property of an interacting many-electron system is determined by its ground-state density. The following year a practical method to approximate this density was proposed by Kohn and Sham (Kohn & Sham 1965), and formally the journey of density-functional theory (DFT) began. The use of DFT was modest at best for the next 15 years. Advances in various fronts during this time, especially in the eighties, however, caused the revolution of DFT that took place in the following decades. Among these, pseudopotential theory (a way to model the complicated Coulombic term of core electrons and the nucleus of the atom, and the Pauli repulsion from the core states, with a simpler function producing the same effect beyond a certain distance), iterative minimization techniques, plane-wave basis sets, the supercell approximation to take care of certain aperiodicities, and methods to model a part of the electron-electron interaction, formally known as the exchange-correlation energy, were particularly important. All these developments were assisted by advances in computer technology, which allowed scientists to explore increasingly larger systems.

Newer features enhanced the capabilities of DFT further. For example, the introduction of ultrasoft pseudopotentials (Vanderbilt 1990) made calculations quicker, while density-functional perturbation theory (DFPT) (Zein 1984; Baroni et al. 1987, 2001; Wu et al. 2005) allowed many quantum-mechanical perturbations to be treated under the framework of DFT. An understanding of how to treat electric polarization and related applications involving electric field were similarly important (King-Smith & Vanderbilt 1993; Resta 1994; Souza et al. 2002; Umari

& Pasquarello 2002).

Thus it became possible to calculate scores of material properties using DFT. The agreement between calculations and experiments have variable, but often predictable accuracy. For example, DFT calculations routinely predict lattice parameters within 1-2% of the experimental observations. The trust in this theory has grown formidably in recent years, and it is often used to estimate material properties when performing experiments is costly, difficult, or downright impossible. Another great advantage of a theoretical tool like DFT is that it allows one to study experimentally unstable situations, such as higher-energy structures, or intermediate molecular configurations with bond angles which do not correspond to stable compounds, to gain knowledge about the reaction or phase transition pathways. Recent advances in experimental techniques and better computational facilities have added one more fascinating possibility: that of designing sophisticated new materials starting at the atomic level. One or more compounds can be deposited as films on a substrate with different properties to take advantage of, say, their lattice mismatch. Combined with other properties such as ferroelectricity or ferromagnetism, this composite may exhibit radically different properties not present in its constituents.

Of course, on its own, DFT is not an all-encompassing theory, and it has its share of limitations. It is a zero-temperature theory with certain approximations. Strongly correlated electron systems cannot be studied with this tool, nor can systems with van der Waals interaction (though recent developments may change the latter). Band gaps of semiconductors are systematically underestimated by DFT, while real systems are often too big for the present DFT algorithms and computational capabilities. Having said that, with continuous improvement in terms of features added and the accessible system size, along with theories which go beyond DFT (e.g., dynamical mean field theory to account for the strong

correlation (Georges et al. 1996)), we have much to look forward to in the future. There are useful references mentioned in the beginning of the next subsection, which the interested reader might find helpful for an in-depth view of the subject.

This chapter is organized as follows: In the remainder of this section (Sec. 2.1.1), we will go through a quick introduction to the fundamental equations forming the core of DFT. Sec. 2.2 is on polarization, and the development of the mathematical structure as it is implemented in DFT. In Sec. 2.4 we describe how this same formalism is extended to the case of finite electric field. Sec. 2.5 takes this idea further, and the fixed displacement field implementation is discussed. To carry out calculations in practice under different electric boundary conditions, one needs to account for the forces on the ions and the strains on the unit cell, which change the positions of ions and the shape and size of unit cells. We devote Sec. 2.4.1 and Sec. 2.5.1 to discussing how the stresses and forces are taken care of within the finite electric field and fixed displacement field approaches.

2.1.1 Basic mathematical structure of DFT

With an increase in computational power and the development of new theoretical tools, first-principles calculations have become very popular in predicting material properties (Martin 2004; Payne et al. 1992; Taylor & Heinonen 2002). We start with the adiabatic approximation, or Born-Oppenheimer approximation, which assumes that the electrons respond quickly to any ionic displacement, meaning ionic coordinates are effectively fixed when solving for electrons. Under this approximation, the lattice dynamical properties of a system are determined by the wave function Φ , obtained from the Schrödinger equation

$$\left(- \sum_I \frac{\hbar^2}{2M_I} \frac{\partial^2}{\partial \mathbf{R}_I^2} + E(\mathbf{R}) \right) \Phi(\mathbf{R}) = \varepsilon \Phi(\mathbf{R}), \quad (2.1)$$

where \mathbf{R}_I is the coordinate of the I th nucleus (\mathbf{R} here refers to the ionic coordinates in general). The first term on the left-hand side represents the kinetic energy of the ions, and $E(\mathbf{R})$ is known as the Born-Oppenheimer energy surface. $E(\mathbf{R})$ is the clamped-ion energy of the system, which is a function of \mathbf{R}_I in the above equation. The electronic Hamiltonian $H_{\text{BO}}(\mathbf{R})$, of which $E(\mathbf{R})$ is the ground state eigenvalue, is given by

$$H_{\text{BO}}(\mathbf{R}) = -\frac{\hbar^2}{2m} \sum_i \frac{\partial^2}{\partial \mathbf{r}_i^2} + \frac{e^2}{2} \sum_{i \neq j} \frac{1}{|\mathbf{r}_i - \mathbf{r}_j|} - \sum_{iI} \frac{Z_I e^2}{|\mathbf{r}_i - \mathbf{R}_I|} + \frac{e^2}{2} \sum_{I \neq J} \frac{Z_I Z_J}{|\mathbf{R}_I - \mathbf{R}_J|}. \quad (2.2)$$

Here e and m refer to the electronic charge and mass respectively, and Z_I is the charge on the I th nucleus. H_{BO} is a function of electronic coordinates $\{\mathbf{r}_i\}$, and parametrically dependent on $\{\mathbf{R}_I\}$ for a fixed set of ionic coordinates. The first term on the right-hand side represents the electronic kinetic energy, the second the interaction between electrons, the third that between ions and electrons and the last one is the ion-ion interaction. We do not include the kinetic energy of the ions at the moment, although it is important, say, for the determination of the total energy of the system.

Density-functional theory (DFT) is based on the Hohenberg-Kohn theorem, which states that any property of a many-electron system is a unique functional of the ground-state density of the electrons. We apply this to the ground-state energy itself, and write it as

$$E[n] = \langle \psi_0[n] | T + V_{\text{ext}} + V | \psi_0[n] \rangle, \quad (2.3)$$

where V_{ext} is the external potential to the ground state with wave function ψ_0 , density n_0 and energy E_0 . When the density equals the ground-state density n_0 ,

E finds its minimum E_0 . This means that, if we know the functional form of $E[n]$, we can minimize it to find the ground-state energy. We see that Eq. (2.3) can be written as

$$E[n] = F[n] + \int n(\mathbf{r})V_{\text{ext}}(\mathbf{r})d\mathbf{r}, \quad (2.4)$$

where $F[n] = \langle \psi[n] | T + V | \psi[n] \rangle$ is the *same* functional (its value is not the same) for all interacting N -electron systems with fixed N .

However it does not provide us with any method of finding the energy functional. This issue is tackled with the help of Kohn-Sham theory. It maps the interacting energy functional into a non-interacting N -electron problem where $F[n]$ is rewritten as

$$F[n] = T_0[n] + \frac{e^2}{2} \int \frac{n(\mathbf{r})n(\mathbf{r}')}{|\mathbf{r} - \mathbf{r}'|} d\mathbf{r}d\mathbf{r}' + E_{\text{xc}}[n]. \quad (2.5)$$

Here T_0 is the kinetic energy of the non-interacting electrons, the second term is the electrostatic interaction of the electron charge density, and the exchange-correlation energy E_{xc} is defined through this equation. Minimizing $E[n]$ with the constraint that the total number of electrons remains constant results in an effective one-electron Schrödinger-like equation

$$\left(-\frac{\hbar^2}{2m} \frac{\partial^2}{\partial \mathbf{r}^2} + V_{\text{SCF}}(\mathbf{r}) \right) \psi_n(\mathbf{r}) = \epsilon_n \psi_n(\mathbf{r}) \quad (2.6)$$

with a potential which gives rise to the same ground state density.

This constructed potential V_{SCF} is given by

$$V_{\text{SCF}}(\mathbf{r}) = V_{\text{ion}}(\mathbf{r}) + e^2 \int \frac{n(\mathbf{r}')}{|\mathbf{r} - \mathbf{r}'|} d\mathbf{r}' + \frac{\delta E_{\text{xc}}}{\delta n(\mathbf{r})}, \quad (2.7)$$

or,

$$V_{\text{SCF}}(\mathbf{r}) = V_{\text{ion}}(\mathbf{r}) + V_{\text{H}}(\mathbf{r}) + V_{\text{xc}}(\mathbf{r}). \quad (2.8)$$

Here $V_{\text{H}}(\mathbf{r})$ is the Hartree potential and $V_{\text{xc}}(\mathbf{r})$ is the exchange-correlation potential. V_{SCF} is in turn dependent on the density, and consequently the Kohn-Sham equation (Eq. (2.6)) has to be solved self-consistently. There have been important theoretical advances in approximating the electron exchange-correlation, the most famous being the local-density approximation (LDA).

The potential that a valence electron feels is finally approximated with pseudopotentials. The resulting wave functions mimic the actual wave functions only beyond a certain distance from the nucleus, the effect of tightly bound core charges being smoothed out. This greatly enhances the computational efficiency of this method. In most of the popular computer codes, these equations are solved using plane-wave basis functions, where the Kohn-Sham equation takes a simple form. The kinetic energy becomes diagonal, and the different potential terms are expressed by their Fourier transforms. We present this in the form of a flowchart in Fig. 2.1. Again, another approximation creeps in as a finite number of plane waves are used, but in most cases a compromise between accuracy and computational time is not too hard to reach.

This section has taken a quick look at the basic formulae of DFT. Instead of delving further into it, now we switch gears to talk about implementation of certain other concepts in the next sections of this chapter, related to polarization and electric field. Some of our calculations also require an understanding and operating knowledge of other extensions based on DFT, such as density-functional perturbation theory (DFPT), which we are not going to discuss. Instead, we choose to present the framework of the modern theory of polarization, and the

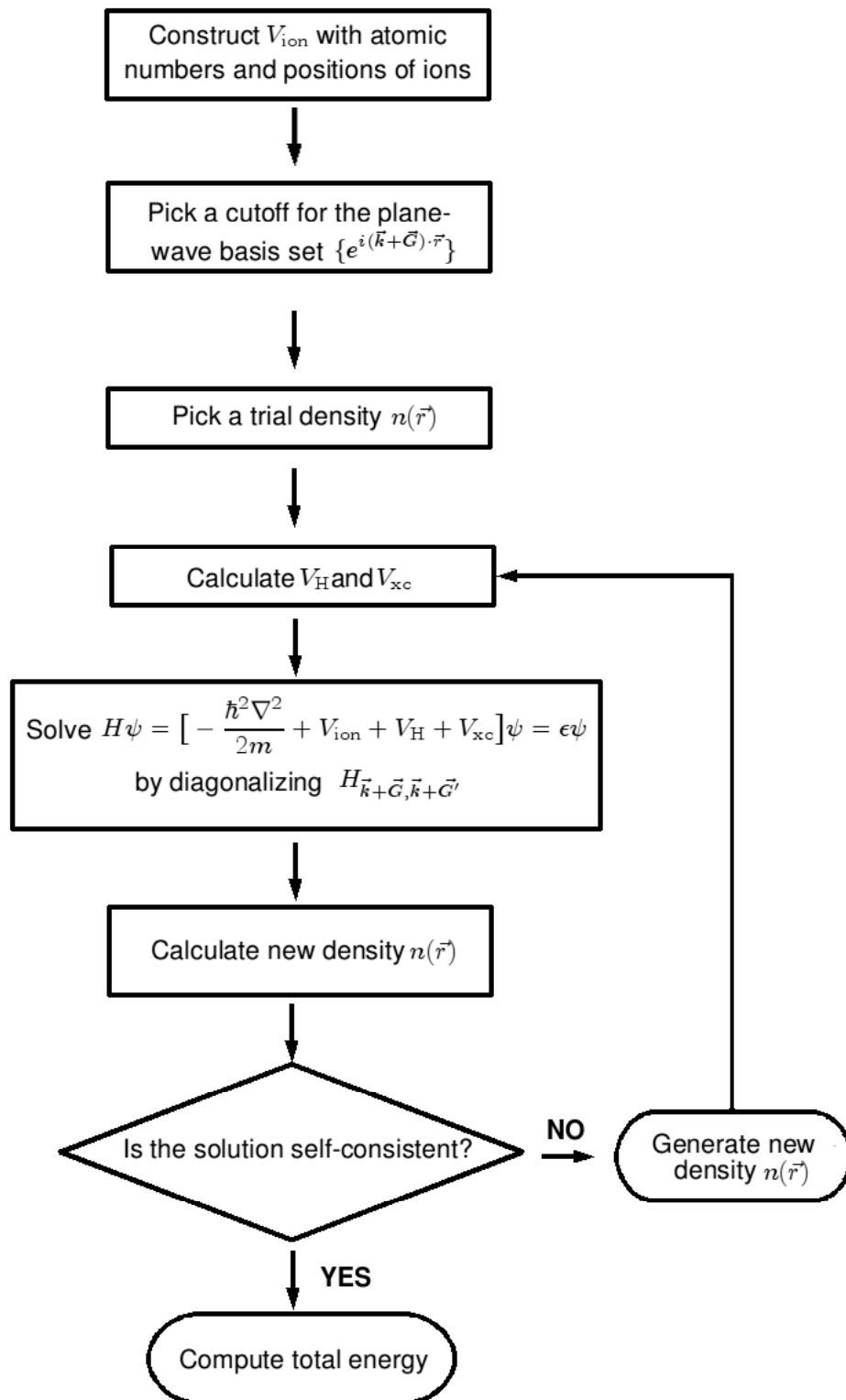


Figure 2.1: The flow chart showing the algorithm to perform total-energy calculation of a periodic crystal using plane-wave basis sets.

formalism for applying a finite electric field or a fixed displacement field in the context of DFT calculations, as the unifying theme connecting all the problems presented in the rest of the chapters.

2.2 Treatment of polarization and related concepts in DFT

It is possible to study many bulk properties of dielectric materials, such as ferroelectricity, piezoelectricity, pyroelectricity, effective charges, dielectric constant etc. under the framework of DFT. However, it is essential then, to be able to apply an electric field and know how to handle the induced polarization. All the problems studied in this thesis are applications to the calculation of some of the above quantities mentioned. Hence, a basic understanding of the theoretical tools necessary to determine these quantities is important, which we set as the goal of the remainder of this introductory chapter.

Polarization is a familiar concept in undergraduate physics, but it proved to be quite a challenging problem to formulate it properly for periodic crystals. Once it was known how to solve this problem following the work of King-Smith & Vanderbilt (1993), many other quantities that relied on the knowledge of polarization could also be determined. The treatment of finite electric fields, developed independently by Souza et al. (2002) and shortly after by Umari & Pasquarello (2002), is one prominent application. A formalism for calculations at a fixed displacement field, developed by Stengel et al. (2009a), is another such area. DFPT methods, known before 1993, which allowed application of an electric field as a perturbation effect, enabled one to calculate many of the above properties. But there are many problems, for example, the treatment of structural phase transitions with finite electric field, which cannot be studied by applying an infinitesimal electric field as allowed under DFPT. Depending on the electric boundary conditions of the

experiment (or theory), application of a finite displacement field, rather than the electric field, may be the appropriate choice. Recently this capacity was added to some DFT codes too.

2.3 Modern theory of polarization

Polarization is an important quantity often appearing in the description of an insulator. However, trying to define polarization for a crystal proved to be a long-standing problem. In this section we follow the treatment along the lines of Resta & Vanderbilt (2007), Vanderbilt & Resta (2006) and Resta (1994) in the context of zero electric field.

In a finite system one defines the polarization \mathbf{P} in terms of the dipole moment \mathbf{d} as

$$\mathbf{P} = \frac{1}{V_{\text{tot}}} \int_{\text{all space}} d\mathbf{r} \rho(\mathbf{r}) \mathbf{r}, \quad (2.9)$$

where V_{tot} is the total sample volume. For such a system there might be a contribution from the surfaces, which would be hard to disentangle from the bulk charge distribution, leading to practical difficulty in calculation. Besides, if a surface charge density $\Delta\sigma$ appears on one surface due to some change, $-\Delta\sigma$ surface charge would appear on the opposite surface. The dipole moment between these two surfaces would scale as the sample volume, changing the total polarization. This would occur despite the fact that nothing has changed in the bulk. Clearly such a definition cannot stand for a bulk quantity. For a periodic charge distribution it is tempting to try to solve the problem by choosing a unit cell with volume Ω , using the formula

$$\mathbf{P} = \frac{1}{\Omega} \int_{\Omega} d\mathbf{r} \rho(\mathbf{r}) \mathbf{r}. \quad (2.10)$$

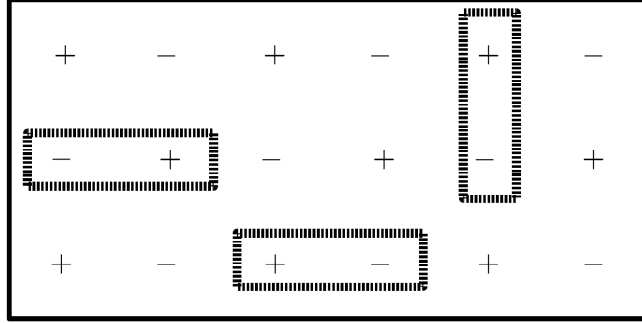


Figure 2.2: Attempt to define polarization using the dipole moment of a fictitious crystal. The direction of the dipole moment is dependent on how one draws the unit cell.

However, in this case, the polarization would depend on the way the cell boundary is drawn and where the cell is placed. This formula works only in the extreme case of the Clausius-Mossotti model, where all charges are concentrated as point charges and the cell boundary goes over zero charge density region always. This is an unavoidable shortcoming, since the electronic charge density is not concentrated at points (as the ‘-’ symbols in Fig. 2.2), and rather is a continuous quantity.

All theoretical definitions of polarization discussed so far above have run into problems. For a change, let us take a cue from experiments on how polarization is measured there. In experiments it is the *change* in polarization that one measures by measuring the current \mathbf{j}_{int} that flows through the bulk (and in the external circuit). This current is a uniquely determinable quantity.

$$\Delta \mathbf{P}(t) = \int_{t_1}^{t_2} dt' \left(\frac{\partial \mathbf{P}}{\partial t'} \right) = \int_{t_1}^{t_2} dt' \frac{1}{\omega} \int_{\Omega} d^3 \mathbf{r} \mathbf{j}_{\text{int}}(\mathbf{r}, t'). \quad (2.11)$$

Extending this definition to parameters other than time, one can define an adiabatic change of polarization as

$$\Delta \mathbf{P} = \int_{\lambda_1}^{\lambda_2} \frac{\partial \mathbf{P}}{\partial \lambda} d\lambda = \mathbf{P}(\lambda_2) - \mathbf{P}(\lambda_1), \quad (2.12)$$

Eq. (2.12) can be divided into an ionic part and an electronic part, i.e., $\Delta\mathbf{P} = \Delta(\mathbf{P}_{\text{ion}} + \mathbf{P}_{\text{el}})$. Here the \mathbf{P}_{ion} is taken to be the contribution from the positive nuclei, with the polarization due to all the electrons being accounted for in the \mathbf{P}_{el} part. \mathbf{P}_{ion} is given by

$$\mathbf{P}_{\text{ion}} = \frac{1}{\Omega} \sum_s Z_s \mathbf{r}_s, \quad (2.13)$$

where Z_s is the bare ionic charge of the atom s at atomic coordinate \mathbf{r}_s in unit cell. Since there is no obvious choice of origin to be made, one can always add a lattice vector \mathbf{R} to the ionic position \mathbf{r}_s in Eq. (2.13): $\mathbf{P}_{\text{ion}} = \frac{1}{\Omega} \sum_s Z_s (\mathbf{r}_s + \mathbf{R})$. This makes the polarization (the ionic part, for the time being) a well-defined quantity modulo $e\mathbf{R}/\Omega$. This $e\mathbf{R}/\Omega$ is commonly known as the *quantum of polarization*. In the subsequent analysis we will see how this quantum of polarization reappears for the case of diffused-charge system (electrons) as well to make it multivalued. Before moving on, we note that in the pseudopotential context, \mathbf{P}_{ion} is not just the contribution of the positive nuclei, but rather is a collection of the positive nuclei and the tightly bound core electrons. As a whole this combination is still small and spherical enough to be considered as a point charge. This renders \mathbf{P}_{el} to be the contribution from the valence electrons only, which is what we are going to discuss next.

First, let us make a slight change of notation, and refer to the electronic contribution to polarization, \mathbf{P}_{el} , as just \mathbf{P} . We are primarily interested in derivatives of polarization with respect to λ , where λ could be a sublattice displacement, strain, etc. As already stated in the beginning of this section, it is possible to calculate all of the above without applying an electric field. One main point of the modern theory of polarization is to show that such changes in polarizations are dependent only on the endpoints of the paths (modulo a quantum).

Without going into details of the DFPT we quote some important formulas here for easy understanding of the subsequent mathematics. The details of the skipped part can be found in references already mentioned.

To construct the theory of polarization using DFPT we start with the case of a finite sample where \mathbf{P} is given by

$$\mathbf{P} = -\frac{e}{L^3} \sum_i \langle \psi_i | \mathbf{r} | \psi_i \rangle. \quad (2.14)$$

This is very similar to Eq. (2.9), L^3 being the volume of the finite sample. Since we are looking for the change in polarization (first-order change $\mathbf{P}^{(1)}$) as explained above, the quantity to look for would be

$$\mathbf{P}^{(1)} = -\frac{e}{L^3} \sum_i \langle \psi_i^{(0)} | \mathbf{r} | \psi_i^{(1)} \rangle + \text{c.c.}, \quad (2.15)$$

where $\psi^{(1)}$ is the first-order change in wave function, and $\psi^{(0)}$ is the unperturbed wave function. $|\psi_i^{(1)}\rangle$ is obtained from first-order perturbation theory as

$$|\psi_i^{(1)}\rangle = \sum_{j \neq i} \frac{|\psi_j^{(0)}\rangle \langle \psi_j^{(0)} |}{E_i^{(0)} - E_j^{(0)}} V^{(1)} |\psi_i^{(0)}\rangle, \quad (2.16)$$

where $V^{(1)}$ is the first-order (in λ) perturbing potential. When we want to extend this definition in Eq. (2.15) for periodic crystals, we have to reexpress \mathbf{r} , since matrix elements of \mathbf{r} between Bloch functions are ill defined. Using the definition of the velocity operator

$$\mathbf{v} = -\frac{i}{\hbar} [\mathbf{r}, H], \quad (2.17)$$

one can rewrite $r_\alpha|\psi_i^{(0)}\rangle = |\tilde{\psi}_{\alpha,i}\rangle$ as

$$|\tilde{\psi}_{\alpha,i}\rangle = \sum_{j \neq i} \frac{|\psi_j^{(0)}\rangle \langle \psi_j^{(0)}|}{E_i^{(0)} - E_j^{(0)}} (i\hbar v_\alpha) |\psi_i^{(0)}\rangle. \quad (2.18)$$

However, both Eqs. (2.16) and (2.18) involve sums over unoccupied states and converge slowly. Corresponding Sternheimer equations

$$(E_i^{(0)} - H)Q_i|\psi_i^{(1)}\rangle = Q_i V^{(1)}|\psi_i^{(0)}\rangle \quad (2.19)$$

and

$$(E_i^{(0)} - H)Q_i|\tilde{\psi}_{\alpha,i}\rangle = Q_i(i\hbar v_\alpha)|\psi_i^{(0)}\rangle, \quad (2.20)$$

are much faster to converge and commonly used instead. Here $Q_i = 1 - |\psi_i^{(0)}\rangle \langle \psi_i^{(0)}|$. Using this definition of Q_i , together with another iteration loop which would determine $V^{(1)}$ for each step, Eq. (2.19) can be solved iteratively for $|\psi_i^{(1)}\rangle$. ($V^{(1)}$ is dependent on the first-order change in density $n^{(1)}(\mathbf{r}) = \sum_i \psi_i^{(0)*}(\mathbf{r})\psi_i^{(1)}(\mathbf{r}) + \text{c.c.}$) Eq. (2.20) can be solved similarly for $|\tilde{\psi}_{\alpha,i}\rangle$. With the help of the above, Eq. (2.15) becomes

$$P_\alpha^{(1)} = -\frac{e}{L^3} \sum_i \langle \tilde{\psi}_{\alpha,i} | \psi_i^{(1)} \rangle + \text{c.c.} \quad (2.21)$$

Finally we are in a position to extend this theory to a periodic crystal. The states denoted by i are replaced by the band index n and the Bloch vector \mathbf{k} . The index m denotes the unoccupied bands in the following equations. The index “(0)” for unperturbed wave functions is dropped as well. Eq. (2.21) then

looks like

$$\mathbf{P}^{(1)} = \frac{i\hbar e}{(2\pi)^3} \sum_n \sum_{m \neq n} \int_{\text{BZ}} d\mathbf{k} \frac{\langle \psi_{n\mathbf{k}} | \mathbf{v} | \psi_{m\mathbf{k}} \rangle \langle \psi_{m\mathbf{k}} | \psi_{n\mathbf{k}}^{(1)} \rangle}{E_{n\mathbf{k}}^{(0)} - E_{m\mathbf{k}}^{(0)}} + \text{c.c.}, \quad (2.22)$$

or, written in terms of change with respect to λ ,

$$\partial_\lambda \mathbf{P} = \frac{i\hbar e}{(2\pi)^3} \sum_n \sum_{m \neq n} \int_{\text{BZ}} d\mathbf{k} \frac{\langle \psi_{n\mathbf{k}} | \mathbf{v} | \psi_{m\mathbf{k}} \rangle \langle \psi_{m\mathbf{k}} | \partial_\lambda \psi_{n\mathbf{k}} \rangle}{E_{n\mathbf{k}}^{(0)} - E_{m\mathbf{k}}^{(0)}} + \text{c.c.}, \quad (2.23)$$

where $\partial_\lambda \equiv \partial/\partial\lambda$. We express this in the \mathbf{k} -basis, where the Schrödinger equation becomes $H_{\mathbf{k}}|u_{n\mathbf{k}}\rangle = E_{n\mathbf{k}}|u_{n\mathbf{k}}\rangle$, $|u_{n\mathbf{k}}\rangle = e^{-i\mathbf{k}\cdot\mathbf{r}}\psi_{n\mathbf{k}}(\mathbf{r})$ and $H_{\mathbf{k}} = e^{-i\mathbf{k}\cdot\mathbf{r}}He^{i\mathbf{k}\cdot\mathbf{r}} = (1/2m_e)(\mathbf{p} + \hbar\mathbf{k})^2 + e^{-i\mathbf{k}\cdot\mathbf{r}}Ve^{i\mathbf{k}\cdot\mathbf{r}}$. Using the perturbation theory the first-order change in $|u_{n\mathbf{k}}\rangle$ is give by

$$|\nabla_{\mathbf{k}}u_{n\mathbf{k}}\rangle = \sum_{m \neq n} \frac{(\nabla_{\mathbf{k}}H_{\mathbf{k}})|u_{m\mathbf{k}}\rangle}{E_{n\mathbf{k}} - E_{m\mathbf{k}}} \quad (2.24)$$

We see that we can express $\nabla_{\mathbf{k}}H_{\mathbf{k}} = -i[\mathbf{r}, H_{\mathbf{k}}]$ and use the definition of the velocity operator, Eq. (2.17), to write the matrix element $\langle \psi_{n\mathbf{k}} | \mathbf{v} | \psi_{m\mathbf{k}} \rangle$ as

$$\langle \psi_{n\mathbf{k}} | \mathbf{v} | \psi_{m\mathbf{k}} \rangle = -i\hbar^{-1} \langle u_{n\mathbf{k}} | [\mathbf{r}, H_{\mathbf{k}}] | u_{m\mathbf{k}} \rangle = \hbar \langle u_{n\mathbf{k}} | (\nabla_{\mathbf{k}}H_{\mathbf{k}}) | u_{m\mathbf{k}} \rangle \quad (2.25)$$

Then Eq. (2.23) can be rewritten as

$$\partial_\lambda \mathbf{P} = \frac{ie}{(2\pi)^3} \sum_n \sum_{m \neq n} \int_{\text{BZ}} d\mathbf{k} \frac{\langle u_{n\mathbf{k}} | (\nabla_{\mathbf{k}}H_{\mathbf{k}}) | u_{m\mathbf{k}} \rangle \langle u_{m\mathbf{k}} | \partial_\lambda u_{n\mathbf{k}} \rangle}{E_{n\mathbf{k}} - E_{m\mathbf{k}}} + \text{c.c.}, \quad (2.26)$$

using Eq. (2.24), which becomes

$$\partial_\lambda \mathbf{P} = \frac{ie}{(2\pi)^3} \sum_n \int_{\text{BZ}} d\mathbf{k} \langle \nabla_{\mathbf{k}}u_{n\mathbf{k}} | \partial_\lambda u_{n\mathbf{k}} \rangle + \text{c.c.} \quad (2.27)$$

At this stage we have lost the sum over the unoccupied states m . Now we can

integrate over λ on both sides of Eq. (2.27) to get

$$\mathbf{P}(\lambda) = \frac{-ie}{(2\pi)^3} \sum_n \int_{\text{BZ}} d\mathbf{k} \langle u_{\lambda, n\mathbf{k}} | \nabla_{\mathbf{k}} | u_{\lambda, n\mathbf{k}} \rangle, \quad (2.28)$$

where we have used an integration by parts and the relation that $\nabla_{\mathbf{k}} \langle u_{n\mathbf{k}} | u_{n\mathbf{k}} \rangle = 0$. Here we have to keep in mind that the $|u_{n\mathbf{k}}\rangle$ functions are implicitly dependent on λ , though we suppress that notation in the following. The integrand in Eq. (2.28) is purely imaginary, and \mathbf{P} can be written as

$$\mathbf{P} = \frac{e}{(2\pi)^3} \text{Im} \sum_n \int_{\text{BZ}} d\mathbf{k} \langle u_{n\mathbf{k}} | \nabla_{\mathbf{k}} | u_{n\mathbf{k}} \rangle. \quad (2.29)$$

This is however just the electronic contribution to polarization, and to get the total polarization we have to add the ionic part, given by Eq. (2.13), as already mentioned in the beginning. The result expressed in Eq. (2.29) is one of the most important results of the modern theory of polarization (King-Smith & Vanderbilt 1993; Vanderbilt & Resta 2006; Resta & Vanderbilt 2007): the electronic part of the polarization can be expressed as a Brillouin zone integration of the operator $i\nabla_{\mathbf{k}}$, which intuitively is similar to the \mathbf{r} operator. However, $i\nabla_{\mathbf{k}} |u_{n\mathbf{k}}\rangle$ depends on the choice of the relative phases of the wave functions. We elaborate this point below for a single band in the case of a 1D crystal of lattice constant a . Let $P = -e\phi/2\pi$, then

$$\phi = -\text{Im} \int_0^{2\pi/a} dk \langle u_k | \partial_k | u_k \rangle. \quad (2.30)$$

Let us consider another set of Bloch functions defined by $|\bar{\psi}_k\rangle = e^{-i\beta(k)} |\psi_k\rangle$, where $\beta(k)$ is a smooth real function of k . This gauge transformation manifests

in Eq. (2.30) as

$$\langle \bar{u}_k | \partial_k | \bar{u}_k \rangle = \langle u_k | \partial_k | u_k \rangle - i \frac{d\beta}{dk}. \quad (2.31)$$

This last term might make it appear ill-defined, but the integral is well defined. This depends on the fact that the wave functions are periodic: $|\psi_{2\pi/a}\rangle = |\psi_0\rangle$ (periodic gauge), which would mean $\beta(2\pi/a) = \beta(0) + 2\pi m$, where m is an integer. This contributes a quantum of polarization ea/Ω (or, $e\mathbf{R}/\Omega$ according to our earlier notation) in the definition of electronic polarization. The quantum-mechanical treatment of the electronic charge distribution gives rise to the same uncertainty modulo $e\mathbf{R}/\Omega$ for ionic polarization given in Eq. (2.13). Thus, the total polarization, from both the ionic and the electronic part inherits this multivalued nature. However, the ambiguity in the value of polarization through the possibility of adding an undetermined quanta of polarization does not lead to great practical difficulty. For the electronic part, we rarely have changes big enough in either state of polarization to add up to a quantum of polarization by mistake. In cases for which there could be confusion (say, the paraelectric to ferroelectric transition of PbTiO_3), one can divide up the transition in smaller pieces and track the polarization along this path to avoid adding an extra quantum of polarization. Alternatively, one can use Wannier function expressions for the same purpose, which we are not discussing here. Similarly, the shift in ionic coordinates in the initial and the final states could be checked to avoid an inadvertent inclusion of an extra lattice vector in one of the states, which could add one or more quanta of polarization to the \mathbf{P}_{ion} part.

2.3.1 Discrete k -space formalism

For practical computation one has to make the k -space discrete, and the integrations over the Brillouin zone in Eq. (2.27) and Eq. (2.29) are replaced by sums. Again, we work out the one-dimensional case with the previous notation, $P_n = (e/2\pi)\phi_n$, where n denotes the band index. We introduce $k_j = 2\pi j/Ma$ as the j 'th k -point. Then $u_{n,k+dk}$ is expanded as

$$u_{n,k+dk} = u_{nk} + dk(\partial_k u_{nk}) + \mathcal{O}(dk^2). \quad (2.32)$$

We introduce this expansion in $\phi_n = \text{Im} \int_0^{2\pi/a} dk \langle u_{nk} | \partial_k | u_{nk} \rangle$, keeping only the leading term. This turns the above equation into

$$\phi_n = \text{Im} \ln \prod_{j=0}^{M-1} \langle u_{n,k_j} | u_{n,k_{j+1}} \rangle, \quad (2.33)$$

using Eq. (2.32) and the expansion of $\ln(1+x)$ for small x .

We have only M independent states $|u_{n,k_0}\rangle$ to $|u_{n,k_{M-1}}\rangle$ in the discrete space, with $|u_{n,k_0}\rangle = e^{2\pi i x/a} |u_{n,k_M}\rangle$. Thus we can think of the Brillouin zone as a closed space (a loop in 1D and a torus in 2D). According to Eq. (2.33) we calculate the global product of wave functions

$$\dots \langle u_{n,k_1} | u_{n,k_2} \rangle \langle u_{n,k_2} | u_{n,k_3} \rangle \langle u_{n,k_3} | u_{n,k_4} \rangle \dots \quad (2.34)$$

Taking the imaginary part of the \ln of Eq. (2.34) is similar to calculating the phase of this product, called the ‘‘Berry phase’’ (Berry 1984). In 3D the Brillouin zone is a 3-torus, and $|\psi_{n,\mathbf{k}}\rangle = |\psi_{n,\mathbf{k}+\mathbf{G}_j}\rangle$, where \mathbf{G}_j is the reciprocal vector in the j direction. The Berry phase in direction j is given by $\phi_{n,j} = (\Omega/e)\mathbf{G}_j \cdot \mathbf{P}_n$, \mathbf{P}_n

being the contribution from the band n . Hence,

$$\phi_{nj} = \frac{1}{\Omega_{\text{BZ}}} \text{Im} \int_{\text{BZ}} d^3k \langle u_{n\mathbf{k}} | \mathbf{G}_j \cdot \nabla_{\mathbf{k}} | u_{n\mathbf{k}} \rangle. \quad (2.35)$$

If we assume there are $N_{\mathbf{k}_{\parallel}}$ k -points along the reciprocal direction j and a total of $N_{\mathbf{k}_{\perp}}$ k -points in the directions perpendicular to it, to find the polarization along that reciprocal direction one calculates the Berry phase for all $N_{\mathbf{k}_{\perp}}$ points separately and then takes an average. In other words,

$$\phi_{nj} = \frac{1}{N_{\mathbf{k}_{\perp}}} \sum_{\mathbf{k}_{\perp}} \phi_{nj}(\mathbf{k}_{\perp}) \quad (2.36)$$

and the total polarization for the band n is given by

$$\mathbf{P}_n = \frac{e}{2\pi\Omega} \sum_j \phi_{n,j} \mathbf{R}_j, \quad (2.37)$$

\mathbf{R}_j being the primitive lattice vector corresponding to \mathbf{G}_j .

When one extends the above formalism to the multiband case, there is a sum over bands for Eq. (2.30):

$$\phi_{\text{tot}} = \sum_{n=1}^L \phi_n = -\text{Im} \sum_{n=1}^L \int_0^{2\pi/a} dk \langle u_{nk} | \partial_k | u_{nk} \rangle. \quad (2.38)$$

Defining $A_{mn}(k) = \langle u_{mk} | i\partial | u_{nk} \rangle$, we rewrite Eq. (2.38) as

$$\phi_{\text{tot}} = \int_0^{2\pi/a} dk \text{Tr}[A(k)], \quad (2.39)$$

where $\text{Tr}[A(k)] = \sum_m A_{mm}(k)$, the trace of the matrix $A(k)$. Discretizing over k -space as in the single-band case, and using the expansion of $\ln(1+x)$, the above

equation becomes

$$\phi_{\text{tot}} = i \sum_{j=0}^{M-1} \text{Tr}[S(k_j, k_{j+1}) - \mathbb{I}_{L \times L}], \quad (2.40)$$

where the overlap matrix $S_{nm}(k_j, k_{j+1}) = \langle u_{mk_j} | u_{nk_{j+1}} \rangle$ and $\mathbb{I}_{L \times L}$ is the $L \times L$ identity matrix. Using the linear algebra relation $\text{Tr}[M - \mathbb{I}] \approx \ln \det M$ up to the leading order, Eq. (2.40) is transformed to

$$\phi_{\text{tot}} = -\text{Im} \sum_{j=0}^{M-1} \ln \det S(k_j, k_{j+1}) \quad (2.41)$$

It is now relatively simple to write down the relevant formulas for 3D. Let us discretize the k -space with a mesh of $N_k = N_1 \times N_2 \times N_3$. Then the polarization parallel to a reciprocal direction would be

$$P_{\parallel}(\lambda) = \frac{e}{(2\pi)^3} \int dk_{\perp} \sum_{j=1}^{N_k} \text{Im} \{ \ln \det S(\mathbf{k}_j, \mathbf{k}_{j+1}) \}. \quad (2.42)$$

Next we introduce f as the spin degeneracy of electrons, which would count contributions from electrons towards polarization irrespective of their spin states: $P \cdot \mathbf{b}_i = (fe/\Omega)\phi^{(i)}$, where

$$\phi^{(i)} = \frac{1}{N_{\perp}^{(i)}} \sum_{l=1}^{N_{\perp}^{(i)}} \text{Im} \ln \prod_{j=0}^{N_i-1} \det S(\mathbf{k}_j^{(i)}, \mathbf{k}_{j+1}^{(i)}), \quad (2.43)$$

in the direction of primitive reciprocal lattice vector \mathbf{b}_i .

This is the general method by which the polarization is calculated in electronic-structure calculation codes based on the modern theory of polarization. In this context, we touched upon certain concepts such as the origin of quantum of polarization, choosing the right branch while determining the electronic contribution to polarization etc. In the next section we sketch briefly how first-principles

calculations are performed in presence of a finite electric field.

2.4 Implementation of finite electric field formalism in DFT

In this section we follow the treatment primarily as outlined in Souza et al. (2002) and Nunes & Gonze (2001). In the presence of an electric field the Hamiltonian becomes

$$H = \frac{p^2}{2m_e} + V_{\text{per}}(\mathbf{r}) + e\boldsymbol{\mathcal{E}} \cdot \mathbf{r}, \quad (2.44)$$

where $V_{\text{per}}(\mathbf{r})$ has the periodicity of the crystal. This periodicity is lost when one adds the term with the electric field $\boldsymbol{\mathcal{E}}$, as shown in Fig. 2.3 for a one-dimensional crystal: the total potential $V(x+a) \neq V(x)$. Hence the Bloch theorem cannot be applied directly. Theoretically the Hamiltonian does not have a ground state. Fig. 2.4 explains the physical picture from another angle, where the lowest conduction band (CB) and the highest valence band (VB) are shown as functions of spatial positions, tilted in the presence of an electric field. For an insulator of gap E_g , the energy would be lowered if one takes an electron from the top of the VB to the bottom of the CB, by crossing a distance $> L_t = E_g/\mathcal{E}$. This phenomenon is known as *Zener tunneling*. However, it is still possible to study the effects of an infinitesimal field using DFPT. It is much more difficult when one is interested in a finite electric field. Let us imagine we adiabatically apply an electric field to a dielectric crystal in its ground state. If the field is small enough to cause little Zener tunneling, we can expect the electronic charge density $\rho(\mathbf{r})$ to remain periodic, though there is some rearrangement inside the cell as the electronic wave functions respond to the field. This would give rise to a state which would exist long enough for the relevant properties of insulators to

be studied.

This periodicity in charge density is imposed as a requirement to develop the methodology. We introduce here the field-polarized Bloch functions $\{\psi_{n\mathbf{k}}(\mathbf{r})\}$, where $\psi_{n\mathbf{k}}(\mathbf{r}) = e^{i\mathbf{k}\cdot\mathbf{r}}u_{n\mathbf{k}}(\mathbf{r})$, and $u_{n\mathbf{k}}(\mathbf{r}) = u_{n\mathbf{k}}(\mathbf{r} + \mathbf{R})$. These are obtained by minimizing the electric enthalpy functional

$$\mathcal{F}[u_{n\mathbf{k}}; \mathcal{E}] = E_{KS}[u_{n\mathbf{k}}] - \Omega \mathbf{P}[u_{n\mathbf{k}}] \cdot \mathcal{E} \quad (2.45)$$

where E_{KS} is the usual zero-field energy functional introduced earlier and \mathbf{P} is the usual Berry-phase polarization. These $\{u_{n\mathbf{k}}\}$ have to be obtained in the presence of the electric field \mathcal{E} . The first term in Eq. (2.45) is thus implicitly dependent on \mathcal{E} , and the polarized Bloch functions are not eigenstates of the Hamiltonian (Eq. (2.44)). However, we want the density matrix $\rho(\mathbf{r}, \mathbf{r}')$ to be periodic:

$$\rho(\mathbf{r}, \mathbf{r}') = \rho(\mathbf{r} + \mathbf{R}, \mathbf{r}' + \mathbf{R}). \quad (2.46)$$

This is guaranteed if we write the density matrix in terms of one-particle wave functions having Bloch form, i.e.,

$$\rho(\mathbf{r}, \mathbf{r}') = (1/N_k) \sum_{n\mathbf{k}} \psi_{n\mathbf{k}}^*(\mathbf{r}') \psi_{n\mathbf{k}}(\mathbf{r}), \quad (2.47)$$

where n runs over the same number of Bloch-like states at all \mathbf{k} .

Using Eq. (2.42) we rewrite Eq. (2.45) as

$$\mathcal{F}[u_{n\mathbf{k}}; \mathcal{E}] = \frac{f}{N_k} \sum_{j=1}^{N_k} \left[\sum_{n=1}^N \langle u_{n\mathbf{k}_j} | H_{KS}(\mathbf{k}_j) | u_{n\mathbf{k}_j} \rangle - \frac{e\mathcal{E}}{\Delta k} \text{Im}\{\ln \det[S(k_j, k_{j+1})]\} \right], \quad (2.48)$$

where $\Delta k = 2\pi/aN_k$.

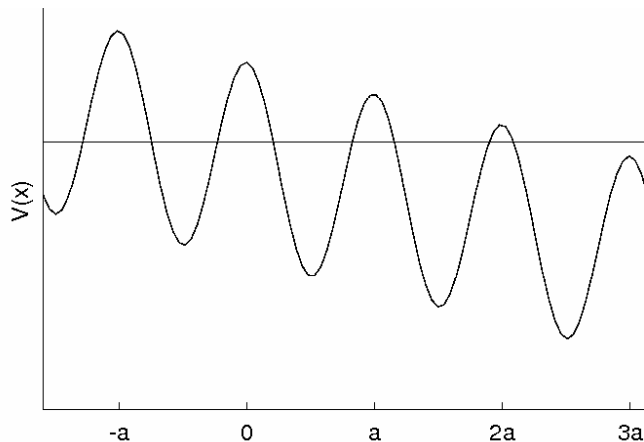


Figure 2.3: The periodic crystal potential energy is tilted in presence of an electric field. The total potential is aperiodic and unbounded.

While these Bloch-like functions ensure that the charge density and other local quantities are periodic under translation by a vector \mathbf{R} in the polarized ground state, they are not eigenstates of the Hamiltonian.

Usually the discrete k -space is introduced for convenience of computation, but in the case of treating electric fields it is essential in order to avoid runaway solutions. For a given k point mesh, \mathcal{F} will have minima if the \mathcal{E} is small enough. There are two relevant length scales in this problem, one of which we already talked about, $L_t = E_g/\mathcal{E}$, the Zener tunneling distance. The other length scale is defined as $L_p = 2\pi/\Delta k$, shown as the distance between the vertical lines bounding the shaded region in the right half of Fig. 2.4. This is inversely proportional to the k -point mesh size. Heuristically, L_p is the size of the box in which we require the charge-density periodicity to hold for the Zener tunneling to be suppressed. If $L_t \ll L_p$, Zener tunneling would occur frequently enough to render any solution impossible. On the other hand, solutions exist if this condition is reversed. We introduce a length scale L_c connected to the critical field \mathcal{E}_c beyond which Zener breakdown would occur for a given cell. It turns out that L_c is of the order of (and scales as) $L_t = E_g/\mathcal{E}$. Thus one has to go for a coarser k -point mesh to obtain a solution, a very different situation from most other first-principles calculations.

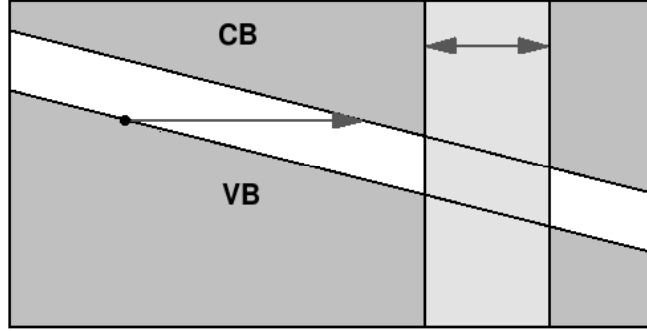


Figure 2.4: Zener tunneling and Δk . The arrow in the left half of the figure is approximately $L_t = E_g/\mathcal{E}$. The double arrow in the right half of the figure is a representative $L_p = 2\pi/\Delta k$.

This is the consequence of having long-lived resonance states as the solution, instead of a ground state. In other words, a very fine k -space mesh can lead to a runaway solution. This problem could be avoided by using sparser submeshes with fewer k points to compute the Berry-phase term for each of them, and finally averaging over all the submeshes.

The functional \mathcal{F} cannot be recast as the expectation value of a Hermitian operator, since the Berry-phase term in the definition of \mathcal{F} contains overlaps of states between adjacent k points, which makes it necessary to solve the problem using self consistency among all k points. This Berry-phase term in \mathcal{F} is the replacement of the usual scalar potential term $e\mathcal{E} \cdot \langle \mathbf{r} \rangle$. In this process \mathcal{F} has to be minimized using an available minimization technique, such as the band-by-band conjugate-gradient method.

2.4.1 Computation of force and stress at $\boldsymbol{\mathcal{E}} \neq 0$

Forces and stresses in the electronic-structure theory are determined using the Hellmann-Feynman theorem. The force $F_I = -\partial E/\partial \mathbf{R}_I$ corresponding to a parameter \mathbf{R}_I is given by

$$-\partial E/\partial \mathbf{R}_I = -\langle \psi | \frac{\partial H}{\partial \mathbf{R}_I} | \psi \rangle - \langle \frac{\partial \psi}{\partial \mathbf{R}_I} | H | \psi \rangle - \langle \psi | H | \frac{\partial \psi}{\partial \mathbf{R}_I} \rangle - \frac{\partial E_{II}}{\partial \mathbf{R}_I}, \quad (2.49)$$

where $\{|\psi\rangle\}$ form exact eigenstates of H , and E_{II} is the electrostatic ion-ion or nucleus-nucleus interaction. We see that the middle two terms on the right-hand side can be rewritten as $\lambda(\partial/\partial \mathbf{R}_I)\langle \psi | \psi \rangle$, with $\hat{H}|\psi\rangle = \lambda|\psi\rangle$. Since the wave functions are normalized, we have $\langle \psi | \psi \rangle = 1$ and the variation of this with \mathbf{R}_I would be 0. When we extend this formalism to the case with electric field, we see that at the stationary point of \mathcal{F} the terms involving the variation of the wave function ψ again vanish, and hence the force $-d\mathcal{F}/d\mathbf{r}_j$ simply becomes $-\partial \mathcal{F}/\partial \mathbf{r}_j$. Since Eq. (2.49) does not have an explicit dependence on \mathbf{r}_j , the force is given by the standard $\boldsymbol{\mathcal{E}} = 0$ Hellmann-Feynman expression obtained from E_{KS} .

An expression for the macroscopic stress tensor can be derived following similar arguments: $\sigma_{\alpha\beta} = (1/\Omega)\partial \mathcal{F}/\partial \eta_{\alpha\beta}$, where η is the homogeneous strain. However, there is a nontriviality involving how strain is defined under electric-field boundary conditions. When the cell is deformed under strain, we can choose to hold constant either the macroscopic field $\boldsymbol{\mathcal{E}}$ or the potential drop $V_i = -\boldsymbol{\mathcal{E}} \cdot \mathbf{a}_i$ across each lattice vector. Again, since the Berry phases do not depend on strain explicitly, it follows from the relation

$$2\pi \mathbf{P}_{\text{el}} \cdot \boldsymbol{\mathcal{E}} = \sum_{i=1}^3 (\boldsymbol{\mathcal{E}} \cdot \mathbf{a}_i) (\mathbf{P}_{\text{el}} \cdot \mathbf{b}_i) = \frac{fe}{\Omega} \sum_{i=1}^3 (\boldsymbol{\mathcal{E}} \cdot \mathbf{a}_i) \phi_{\text{el}}^{(i)} \quad (2.50)$$

that $\partial(\Omega \mathbf{P}_{\text{el}} \cdot \boldsymbol{\mathcal{E}})/\partial \eta_{\alpha\beta} = 0$ when $\mathbf{V} = (V_1, V_2, V_3)$ is fixed. The ionic term can

also be expressed in terms of a phase $\phi_{\text{ion}}^{(i)} = \Omega/(fe)\mathbf{P}_{\text{ion}} \cdot \mathbf{b}_i$. Consequently the stresses in the two cases are related by

$$\sigma_{\alpha\beta}^{(\mathcal{E})} = \sigma_{\alpha\beta}^{(\mathbf{V})} - \frac{fe}{2\pi\Omega} \sum_{i=1}^3 \mathcal{E}_{\alpha}(a_i)_{\beta} (\phi_{\text{el}}^{(i)} + \phi_{\text{ion}}^{(i)}). \quad (2.51)$$

Since the pressure is defined as $p = -(1/3)(\sigma_{11} + \sigma_{22} + \sigma_{33})$, we see from Eq. (2.51), using Eq. (2.50), that the pressure differs by $(\mathbf{P} \cdot \mathcal{E})/3$ between the constant- \mathcal{E} and the constant- \mathbf{V} cases. The stress $\sigma^{(\mathbf{V})}$ is given in terms of the polarized Bloch states by the same formula as for the zero-field ground-state calculation. It is a symmetric tensor. On the other hand, $\sigma^{(\mathcal{E})}$ has an antisymmetric part and depends on the choice of the branch cut made while determining the multivalued bulk quantity \mathbf{P} .

Other important quantities such as piezoelectric tensors can be determined with the help of the above formalism. The so-called *improper* piezoelectric tensor is given by $c_{\alpha\beta\gamma}^{(\mathcal{E})} = d\sigma_{\beta\gamma}^{(\mathcal{E})}/d\mathcal{E}_{\alpha}$, and the proper tensor is given by

$$c_{\alpha\beta\gamma}^{(\mathbf{V})} = \frac{d\sigma_{\beta\gamma}^{(\mathbf{V})}}{d\mathcal{E}_{\alpha}} = - \sum_{i=1}^3 \frac{d\sigma_{\beta\gamma}^{(\mathbf{V})}}{dV_i} a_{i,\alpha}. \quad (2.52)$$

Implementation of this method enables one to calculate Born effective charges from the finite-difference formula $eZ_{j\alpha\beta}^* = dF_{j\beta}/d\mathcal{E}_{\alpha}$, instead of $eZ_{j\alpha\beta}^* = dP_{\alpha}/dx_{j\beta}$, which one can calculate using the polarization routine. One can use a similar approach to determine the dielectric constant of a material. The dielectric constant is given by $\epsilon_{\alpha\beta} = \delta_{\alpha\beta} + \chi_{\alpha\beta}$, where $\chi_{\alpha\beta} = (1/\epsilon_0)dP_{\alpha}/d\mathcal{E}_{\beta}$ and ϵ_0 is the permittivity of free space. When ions are allowed to relax we get what is called the *static* dielectric constant, and keeping them fixed would give us just the electronic contribution, commonly referred to as ϵ_{∞} . Similarly, one can also find the quadratic susceptibility given by $\chi_{\alpha\beta\gamma}^{(2)} = (2/\epsilon_0)d^2P_{\alpha}/d\mathcal{E}_{\beta}d\mathcal{E}_{\gamma}$.

In this section we have discussed how the electronic band-structure formalism is extended to allow finite electric field calculations. As it becomes feasible to apply a finite electric field, one can calculate other quantities such as dielectric constants, piezoelectric effects, etc. at specific values of electric field, previously accessible only for infinitesimal fields using DFPT methods. However, there are limitations regarding the maximum field that can be applied without causing a runaway solution, corresponding to the choice of the k -point grid. The k -point grid has to be made coarser to allow for larger field, thus compromising the accuracy of the solution. Fortunately, the maximum field one can apply is reasonably high compared to most practical situations, as often one is faced with dielectric breakdown in real materials at much smaller fields.

2.5 Implementation of fixed electric displacement field formalism in DFT

The development of the modern theory of polarization fueled a lot of related activities in the electronic-structure-calculation community. The example of the finite electric field implementation has been discussed in the previous section. This was followed by implementation of calculations at a fixed polarization by Diéguez & Vanderbilt (2006). This is exciting since polarization acts as an order parameter in various Landau-Devonshire theories and other semiempirical theories. While the ability to calculate crystal properties *ab-initio* directly in terms of polarization is appealing, it is rather involved to constrain \mathbf{P} during self-consistent determination of electronic wave functions. With bigger supercells or complex structures it quickly becomes computationally impractical. Moreover, fixing \mathbf{P} does not correspond to physically realizable boundary conditions. In a composite heterostructure, the local \mathbf{P} can be different at different points, and fixing it to a

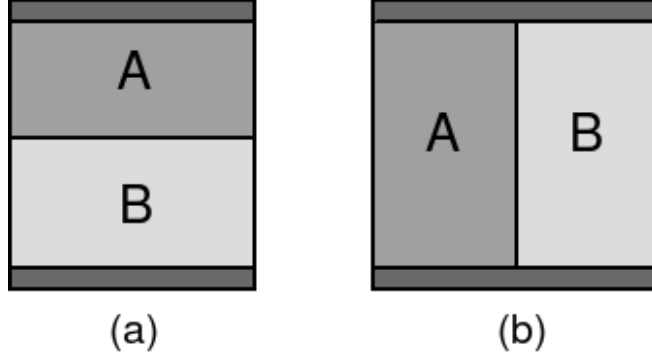


Figure 2.5: Two methods of making a sandwich out of two materials between the electrodes/probes at the top and the bottom. In case (a) electric field and polarization field are not the same on top and at the bottom, whereas the displacement field is. In (b), displacement field and polarization field are not the same, but electric field is the same on left and right of the composite. It is assumed that there is no free charge at the interface.

single average value is artificial. However, fixing the displacement field \mathbf{D} , as described in Stengel et al. (2009a), instead of \mathbf{P} provides an interesting alternative. It corresponds to a capacitor in an open-circuit condition, in contrast to a fixed- \mathcal{E} calculation corresponding to a closed-circuit condition under a fixed voltage V . As explained in Fig. 2.5, the electric field is the useful field to work with for case (b), but displacement field is more useful for case (a). However, case (a) is more common, given how composite materials are grown. Thus, the displacement field emerges as a more natural choice for such systems.

The starting point is the “internal energy” functional U ,

$$U(\mathbf{D}, v) = E_{\text{KS}}(v) + \frac{\Omega}{8\pi} [\mathbf{D} - 4\pi\mathbf{P}(v)]^2, \quad (2.53)$$

where Ω is the unit cell volume formed by primitive translation vectors \mathbf{a}_i and v denotes the ionic and electronic coordinates. $U(\mathbf{D}, v)$ is directly dependent on \mathbf{D} , and implicitly on v through both E_{KS} and \mathbf{P} . We ignore strain for the moment

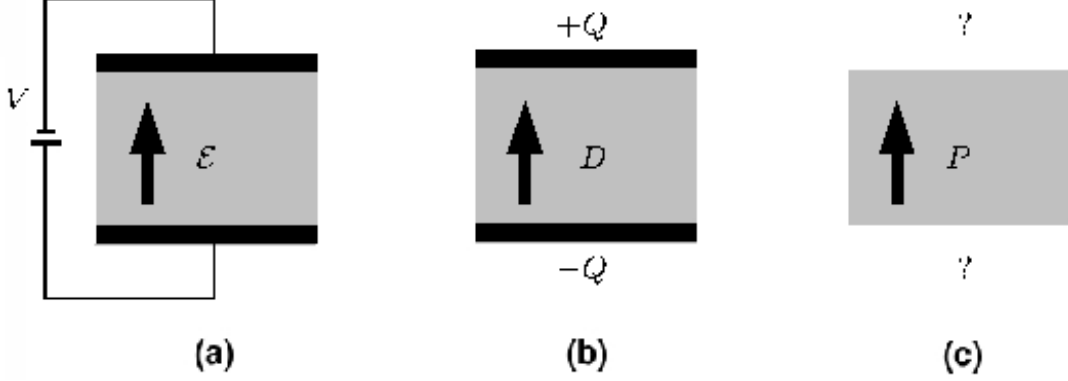


Figure 2.6: Showing different boundary conditions as a constant (a) electric (b) displacement and (c) polarization field is applied. While case (a) corresponds to applying a constant bias across the sample, and case (b) corresponds to an open-circuit condition, there is no immediate physical analogy to case (c).

(fixed \mathbf{a}_i) and the minimum of U at fixed \mathbf{D} is given by the extremum condition

$$\left(\frac{\partial U}{\partial v}\right)_{\mathbf{D}} = \frac{\partial E_{\text{KS}}}{\partial v} - \Omega(\mathbf{D} - 4\pi\mathbf{P}) \cdot \frac{\partial \mathbf{P}}{\partial v} = 0. \quad (2.54)$$

Comparison with the electric enthalpy function Eq. (2.45) tells us that

$$\left(\frac{\partial \mathcal{F}}{\partial v}\right)_{\boldsymbol{\mathcal{E}}} = \left(\frac{\partial U}{\partial v}\right)_{\mathbf{D}}, \quad (2.55)$$

if one sets $\boldsymbol{\mathcal{E}} = \mathbf{D} - 4\pi\mathbf{P}$. In fact, this is the identifying relation that \mathbf{D} indeed is the macroscopic displacement field. With this we can rewrite Eq. (2.53) as $U = E_{\text{KS}} + (\Omega/4\pi)\boldsymbol{\mathcal{E}}^2$, which is the expression of the internal energy of a periodic crystal under a uniform external field. Eq. (2.55) justifies how this method is very similar to a finite- $\boldsymbol{\mathcal{E}}$ calculation, except that the value of \mathbf{D} is kept fixed at the end of each iteration, rather than $\boldsymbol{\mathcal{E}}$. Forces are calculated similarly using the Hellmann-Feynman formalism. In an existing code capable of finite- $\boldsymbol{\mathcal{E}}$ calculation this requires few changes to be made.

2.5.1 Determination of the stress tensor

First let us define some notations heavily in this subsection. \mathbf{a}_i are the primitive lattice vectors, with $g_{ij} = \mathbf{a}_i \cdot \mathbf{a}_j$ as the metric tensor. \mathbf{b}_i differ from the conventional reciprocal vectors by a factor of 2π and satisfy $\mathbf{a}_i \cdot \mathbf{b}_j = \delta_{ij}$ (We specifically point out this difference in definition of \mathbf{b}_i with that in Eq. (2.43)). It follows that $\mathbf{b}_i \cdot \mathbf{b}_j = (g^{-1})_{ij}$. We define two sets of reduced variables. The first set is

$$p_i = \Omega \mathbf{b}_i \cdot \mathbf{P} \quad \Longleftrightarrow \quad \mathbf{P} = \frac{1}{\Omega} \sum_i p_i \mathbf{a}_i, \quad (2.56)$$

$$\varepsilon_i = \Omega \mathbf{b}_i \cdot \boldsymbol{\mathcal{E}} \quad \Longleftrightarrow \quad \boldsymbol{\mathcal{E}} = \frac{4\pi}{\Omega} \sum_i \varepsilon_i \mathbf{a}_i \quad (2.57)$$

$$d_i = \Omega \mathbf{b}_i \cdot \mathbf{D} \quad \Longleftrightarrow \quad \mathbf{D} = \frac{1}{\Omega} \sum_i d_i \mathbf{a}_i. \quad (2.58)$$

With this set of equations, $\mathbf{D} = \boldsymbol{\mathcal{E}} + 4\pi\mathbf{P}$ becomes $d_i = \varepsilon_i + p_i$. Note that d_i , ε_i and p_i have units of charge, and are related to free charge, total charge, and bound charge, respectively, found on a surface perpendicular to \mathbf{b}_i . Defined thus, we see that p_i is the Berry phase ϕ_i times a factor $e/2\pi$ (for a single spin state). The other set of reduced variables are in terms of the real-space coordinates:

$$\bar{p}_i = 4\pi \mathbf{a}_i \cdot \mathbf{P} \quad \Longleftrightarrow \quad \mathbf{P} = \frac{1}{4\pi} \sum_i \bar{p}_i \mathbf{b}_i \quad (2.59)$$

$$\bar{\varepsilon}_i = 4\pi \mathbf{a}_i \cdot \boldsymbol{\mathcal{E}} \quad \Longleftrightarrow \quad \boldsymbol{\mathcal{E}} = \sum_i \bar{\varepsilon}_i \mathbf{b}_i \quad (2.60)$$

$$\bar{d}_i = \mathbf{a}_i \cdot \mathbf{D} \quad \Longleftrightarrow \quad \mathbf{D} = \sum_i \bar{d}_i \mathbf{b}_i \quad (2.61)$$

This time the relation $\mathbf{D} = \boldsymbol{\mathcal{E}} + 4\pi\mathbf{P}$ becomes $\bar{d}_i = \bar{\varepsilon}_i + \bar{p}_i$. Now, \bar{d}_i , $\bar{\varepsilon}_i$ and \bar{p}_i have units of electric potential, and can be interpreted as the potential drops along the direction \mathbf{a}_i in the unit cell associated with the displacement field, the electric field, and the polarization field, respectively.

Finally, the interrelations among the barred and the unbarred quantities are given by

$$\bar{p}_i = \frac{4\pi}{\Omega} \sum_j g_{ij} p_j, \quad \bar{\varepsilon}_i = \frac{4\pi}{\Omega} \sum_j g_{ij} \varepsilon_j, \quad \bar{d}_i = \frac{4\pi}{\Omega} \sum_j g_{ij} d_j. \quad (2.62)$$

As already mentioned, the constrained- \mathbf{D} method is analogous to a capacitor under open-circuit condition, which connects it to the stress tensor. The difference in the component of the \mathbf{D} vector inside and outside the dielectric is the magnitude of the free surface charge. Under open condition the capacitor cannot exchange free charge with its environment, implying that the flux of the \mathbf{D} field remains constant even under an applied strain. These fluxes are defined as $(\mathbf{a}_i \times \mathbf{a}_j) \cdot \mathbf{D} = \Omega \mathbf{b}_i \cdot \mathbf{D} = d_i$. Gauss's law implies $d_i = -Q_i$, where Q_i are the free surface charges per unit area located on the surface normal to \mathbf{b}_i . It is worth underscoring that d_i , p_i and ε_i are all constants as the unit cell is strained, while \bar{d}_i , \bar{p}_i and $\bar{\varepsilon}_i$ are not.

With these definitions we can rewrite Eq. (2.53) as

$$U(\{d\}) = E_{\text{KS}} + \frac{2\pi}{\Omega} \sum_{ij} (d_i - p_i) g_{ij} (d_j - p_j). \quad (2.63)$$

Next, the fixed- $\{d\}$ stress tensor is defined as

$$\sigma_{\mu\nu}^{(d)} = \frac{1}{\Omega} \left(\frac{dU}{d\eta_{\mu\nu}} \right) \quad (2.64)$$

where $\eta_{\mu\nu}$ is the strain tensor. We note that $dg_{ij}/d\eta_{\mu\nu} = 2a_{i\mu}a_{j\nu}$, and $d\Omega/d\eta_{\mu\nu} = \Omega\delta_{\mu\nu}$. This transforms Eq. (2.64) as

$$\sigma_{\mu\nu}^{(d)} = \frac{1}{\Omega} \left(\frac{\partial E_{\text{KS}}}{\partial \eta_{\mu\nu}} \right) + \frac{2\pi}{\Omega^2} [2a_{i\mu}a_{j\nu}\varepsilon_i\varepsilon_j - \delta_{\mu\nu}g_{ij}\varepsilon_i\varepsilon_j] - \left(\frac{4\pi}{\Omega} \right)^2 \sum_i \bar{\varepsilon}_i \frac{\partial p_i}{\partial \eta_{\mu\nu}}, \quad (2.65)$$

or

$$\sigma_{\mu\nu}^{(d)} = \sigma_{\mu\nu}^{\text{KS}} + \sigma_{\mu\nu}^{\text{Max}} + \sigma_{\mu\nu}^{\text{aug}}, \quad (2.66)$$

where $\sigma_{\mu\nu}^{\text{KS}}$ is the expression of stress in absence of a field,

$$\sigma_{\mu\nu}^{\text{Max}} = \frac{2\pi}{\Omega^2} [2a_{i\mu}a_{j\nu}\varepsilon_i\varepsilon_j - \delta_{\mu\nu}g_{ij}\varepsilon_i\varepsilon_j] = \frac{2\mathcal{E}_\mu\mathcal{E}_\nu - \delta_{\mu\nu}\mathcal{E}^2}{8\pi} \quad (2.67)$$

is the Maxwell stress tensor, and the last term

$$\sigma_{\mu\nu}^{\text{aug}} = -\left(\frac{4\pi}{\Omega}\right)^2 \sum_i \bar{\varepsilon}_i \frac{\partial p_i}{\partial \eta_{\mu\nu}} \quad (2.68)$$

is the ‘‘augmented’’ part. This term appears only when specialized techniques like ultrasoft pseudopotentials (USPP) or the projector augmented-waves method (PAW) are used to replace the core electrons of nuclei. The technicalities leading to the appearance of this terms are discussed in Vanderbilt (1990) for USPP and Blöchl (1994) for PAW. It vanishes when the internal coordinates v are chosen as reduced coordinates and norm-conserving pseudopotentials are used. The choice of the reduced coordinate d_i , instead of \mathbf{D} , automatically makes sure that we obtain the proper piezoelectric tensors.

In this section the formalism to apply a fixed displacement field has briefly been discussed, corresponding to the practical electric boundary condition of an open-circuit capacitor. It is relatively simple to incorporate this feature into an electronic-structure code capable of performing calculations with finite electric field. The present section concludes this chapter, which gives an overview of the modern theory of polarization as implemented in DFT codes, and forms the backbone of further developments along this line. Implementation of formalisms for finite electric field and fixed displacement field are two such achievements that

are discussed here. In the following chapters we will see examples where these capabilities are used in various problems, which are inspired by real experiments or serve as inspiration for future experiments.

Chapter 3

First-principles study of high-field piezoelectricity in tetragonal PbTiO_3

3.1 Introduction

Piezoelectricity was discovered in the late nineteenth century and has been successfully described at the phenomenological macroscopic level since the early twentieth century. Piezoelectric materials find a variety of technological uses including sonar detection, electromechanical actuators and resonators, and high-precision applications such as in microbalances and scanning-probe microscopes. Most of these conventional applications depend on the linearity of the strain response to the applied electric field or vice versa. Application of large strains or strong electric fields may, however, generate a nonlinear response. Such nonlinearities are less well characterized and understood, despite the fact that they may have important practical implications for degrading or improving device performance.

The intrinsic nonlinear piezoelectric properties of a material may be difficult to access experimentally for two reasons. First, application of large stresses or strains may cause cracking or other forms of mechanical failure, while application of strong electric fields may cause dielectric breakdown, leading in either case to a limited ability to access the nonlinear regime. Second, most strong (and strongly nonlinear) piezoelectrics are ferroelectrics, whose spontaneous polarization is strongly modified by applied strains or fields. Real samples of ferroelectric

materials usually break up into domains having different directions of the spontaneous polarization, and the observed piezoelectric response may be dominated by extrinsic processes associated with changes in domain populations under applied strain or field. Studies of single-domain samples are difficult; even if such a sample is obtained, the domain may tend to reorient under applied strain or field. In the case of a strong applied electric field, one expects that the sample will eventually be poled into a single-domain state, so that a subsequent increase of the field strength will access the intrinsic piezoelectric response. However, one must still overcome the problems associated with dielectric breakdown mentioned earlier.

In the last two decades or so, predictive quantum-mechanical descriptions based on first-principles electronic-structure calculations have been successfully developed and applied to piezoelectric and ferroelectric materials (see Rabe & Ghosez (2007) for a recent review). These methods allow one to isolate the intrinsic contributions to the nonlinear piezoelectric behavior of a material by calculating the response explicitly. We apply such methods here to the study of tetragonal PbTiO_3 (PT) thin films under a strong electric field applied parallel to the polarization direction.

Our work is motivated in part by recent experimental and modeling studies of PT and $\text{PbZr}_x\text{Ti}_{1-x}\text{O}_3$ (PZT) thin films (Nagarajan et al. 2002; Chen et al. 2003; Grigoriev et al. 2008). Based on experimental measurements (Nagarajan et al. 2002) on PT and PZT films in fields up to ~ 50 MV/m, Landau-Devonshire models were developed to systematize the data and extrapolate to higher fields (Chen et al. 2003). For pure PT, these papers show d_{33} dropping by about 16% and 10% as the electric field is increased to 50 MV/m for the cases of free-stress and epitaxially-constrained samples respectively. (For the latter, the in-plane lattice constant was constrained to that of the SrTiO_3 substrate.) These results

are roughly in agreement with previous results of a first-principles calculation (Sai et al. 2002) for the free-stress case, although the methods used there involved approximations that are removed in the present work.

More recently, Grigoriev et al. (2008) measured the piezoelectric response of epitaxially constrained PZT 20/80 (i.e., $x=0.2$) films using a novel approach in which dielectric breakdown was avoided by the use of ultrashort electric-field pulses in a thin-film geometry. This allowed access to much larger electric fields than previously possible, up to about 500 MV/m compared with ~ 50 MV/m studied in the earlier experiments. The strain response showed almost no saturation up to the highest fields reached in the experiment, around 500 MV/m, contrasting with the conclusions of Nagarajan et al. (2002) and Chen et al. (2003). These results may suggest that the previous work, limited as it was to smaller fields and longer time scales, may have been more sensitive to extrinsic effects such as incomplete poling of the domains.

Clearly, information from predictive first-principles calculations would be very useful here. A preliminary application of such methods to the case of stress-free PT under strong applied electric fields (Stengel et al. 2009a) showed not only a lack of saturation, but even an enhancement of the piezoelectric response, with d_{33} increasing up to fields of about 550 MV/m. This unexpected (Nagarajan et al. 2002; Chen et al. 2003) enhancement was ascribed to a field-induced structural transition in which the PT crystal adopts a supertetragonal state at high fields, with an extreme axial c/a ratio of 1.2-1.3. Such a supertetragonal state was first identified theoretically by Tinte (Tinte et al. 2003) who predicted its occurrence in PT under conditions of fictitious negative pressure. Interestingly, a similarly strong tetragonal distortion was recently reported for other materials, e.g. BiCoO_3 in its bulk ground state (Belik et al. 2006) and BiFeO_3 films under a compressive epitaxial strain (Béa et al. 2009). These results suggest that the peculiar

electromechanical response of PT reported in Ref. (Stengel et al. 2009a) might be a rather general property of many perovskite materials. In particular, it is not unreasonable to think that, by understanding the interplay of composition, epitaxial strain, pressure and applied external fields, one might be able to *control* the crossover between the competing “normal” and “supertetragonal” phases in a given Pb- or Bi-based compound. This might produce exciting and unusual effects, such as giant piezoelectric responses and radical magnetoelectric couplings (for example, a magnetic moment collapse and insulator-to-semimetal transition under pressure was recently reported for BiCoO₃ (Ming et al. 2009)), with a wide range of implications for technology and fundamental science.

To help shed light on the above issues, in this work we extend the analysis of Stengel et al. (2009a) to study the impact of the elastic boundary conditions on the electromechanical response of PT. In particular, we address here the case of epitaxially constrained or stress-free films, with or without external pressure, and in a wide range of applied electric fields. For the case of an epitaxially constrained film, our first-principles calculations indicate that d_{33} of PT monotonically decreases with field, but only slowly: by about 2-3% up to 50 MV/m, 11-14% at 500 MV/m, and 40-50% at 1500 MV/m. Our results thus suggest that, based on intrinsic material properties, the strain enhancement can continue to quite large fields, with only a very slow saturation of d_{33} , at variance with previous expectations (Nagarajan et al. 2002; Chen et al. 2003) and strengthening the findings in Grigoriev et al. (2008). In the absence of an epitaxial constraint, we confirm the previous results of Stengel et al. (2009a), finding a maximum of d_{33} around 550 MV/m and then a gentle drop-off to about a third of its highest value at 1400 MV/m. We further investigate the field-induced strain response of the system under the application of a fictitious negative pressure.

In comparing our work with experimental studies, it is useful to keep in mind

the context and implicit assumptions of our calculations. Following the standard framework of density-functional theory, we treat pure defect-free PT in perfect tetragonal symmetry at zero temperature, with and without in-plane epitaxial constraint. We preserve the primitive periodicity, so that domain formation is excluded. We study the response of the system on a time scale on which lattice and strain response can occur, but domain dynamics cannot occur. We can go to much larger fields than can be accessed even by the pulsed-field methods, (Grigoriev et al. 2008) limited only by the intrinsic breakdown fields associated with our method for treating the electric field (Íñiguez & Vanderbilt 2002; Umari & Pasquarello 2002). We thus study a regime of intrinsic behavior that, we believe, is closer to that of Grigoriev et al. (2008) than that of Nagarajan et al. (2002); Chen et al. (2003).

This chapter is organized as follows. We briefly describe the computational details in Sec. 3.2. We then present the results of our calculations in Sec. 3.3 and compare them with experiment. We also describe further investigations of the system as we go beyond the experimental conditions, and discuss the implications of the work. We then summarize in Sec. 3.4.

3.2 Computational details

The calculations are performed using density-functional theory with two *ab-initio* computer code packages, ABINIT (Gonze et al. 2002, 2005, 2009) and LAUTREC.¹ We use the Ceperley-Alder (Ceperley 1978; Ceperley & Alder 1980) exchange-correlation, implemented in the Perdew-Zunger (Perdew & Zunger 1981) and Perdew-Wang (Perdew & Wang 1992) parameterizations for ABINIT and LAUTREC respectively. For ABINIT we use norm-conserving pseudopotentials

¹LAUTREC is a massively parallel “in-house” electronic-structure code.

generated using the method of Ramer and Rappe (Ramer & Rappe 1999) as implemented in the OPIUM package,² while in LAUTREC we use projector augmented-wave (PAW) potentials (Blöchl 1994). In both cases, the semicore $3s$ and $3p$ orbitals of Ti, and the $5d$ orbitals of Pb are treated as valence electrons. Plane-wave cutoffs of 50 and 30 Hartree are chosen for ABINIT and LAUTREC respectively (the PAW potentials being softer than the norm-conserving ones). The Brillouin zone is sampled by a $4 \times 4 \times 4$ Monkhorst-Pack (Monkhorst & Pack 1976) k -point mesh for ABINIT and a $6 \times 6 \times 6$ mesh for LAUTREC. A stress threshold of 2×10^{-2} GPa is used for cell relaxation,³ and forces on ions are converged below 2.5×10^{-3} eV/Å.

In ABINIT the electric polarization is calculated using the Berry-phase approach (King-Smith & Vanderbilt 1993) and is coupled to a fixed electric field \mathcal{E} (Souza et al. 2002; Stengel & Spaldin 2007). In LAUTREC the electric polarization is computed using the centers of the “hermaphrodite” Wannier orbitals (Stengel & Spaldin 2006, 2007) and the electric displacement field D is used as the independent electrical variable (Stengel & Spaldin 2007; Stengel et al. 2009a). In either case, the appropriate E or D field is applied, and the internal coordinates and unconstrained lattice constants are allowed to relax within the constraints of the enforced $P4mm$ tetragonal symmetry. In both cases, the results are presented as a function of E ; for the case of LAUTREC, this is determined at each D from the computed polarization using $E = D - 4\pi P$.

As we shall see, the results obtained using ABINIT and LAUTREC are generally consistent, but with some quantitative differences between them. Tests indicated that the codes produce almost identical results when using the same

²<http://opium.sourceforge.net>

³The Pulay error in the stress tensor was compensated by applying a fixed hydrostatic pressure of -0.4 GPa during the structural relaxations performed with LAUTREC. No correction was used in ABINIT, where the error was found to be smaller than our accuracy threshold.

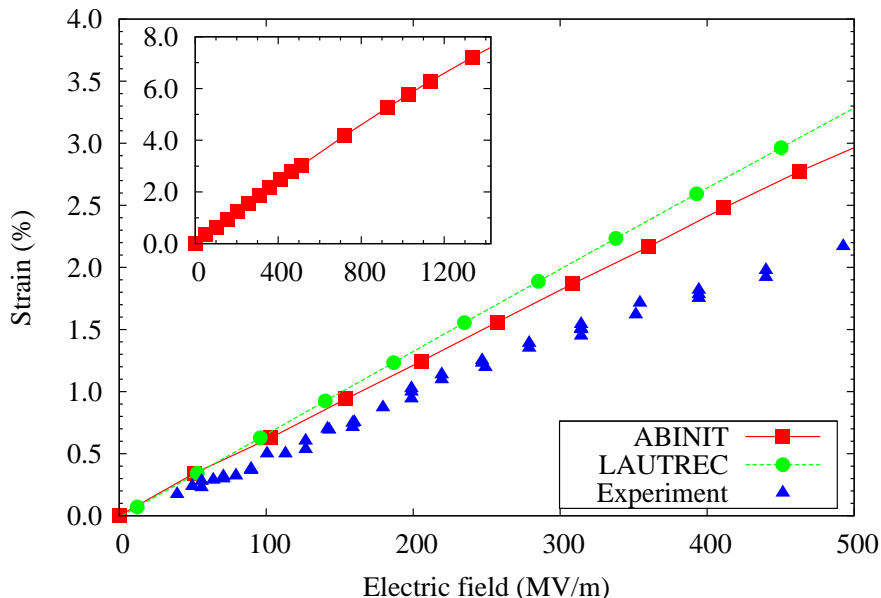


Figure 3.1: Out-of-plane strain response to applied electric field, relative to zero-field ferroelectric state, under in-plane epitaxial constraint. Experiment: data of Grigoriev et al. (2008) for several PZT 20/80 capacitors of varying thickness. Theoretical points with fitted lines: computed results for pure PbTiO_3 using two computer codes. Inset shows the ABINIT results over a more extended range of fields.

potentials, so we can ascribe these differences almost entirely to the different potentials used (norm-conserving for ABINIT vs. PAW for LAUTREC).

3.3 Results

3.3.1 Piezoelectric response with epitaxial constraint

Both the ABINIT and LAUTREC computer codes were used to compute the response of the PT system to electric fields up to 1400 MV/m applied parallel to the polarization (along the tetragonal axis). The epitaxial constraint was enforced by fixing the in-plane lattice constant a to remain at a value 1.14% smaller than the computed equilibrium a_0 of bulk tetragonal PT; this factor was chosen to facilitate comparison with the experiments of Grigoriev et al. (2008) in which the PZT 20/80 film was compressively strained by 1.14% relative to its bulk

equilibrium in-plane lattice constant by its epitaxial coherence with the SrTiO₃ (ST) substrate. Having computed the equilibrium a_0 to be 3.892 and 3.854 Å using ABINIT and LAUTREC respectively, we therefore set the constrained a to be 3.848 and 3.811 Å for the two codes respectively. (We have traced the shift of lattice constant between codes to the choice of Ti pseudopotential, but trends are well reproduced. For example, the respective c/a ratios for the two codes are 1.085 and 1.083 at the constrained a , and 1.047 and 1.044 at the equilibrium a_0 .) For each value of the applied field, we computed the relaxed structure subject to the epitaxial constraints, and computed the strain $\eta_3 = (c - c_0)/c_0$, where c is the z lattice constant at the given field and c_0 is the zero-field value.

The main panel of Fig. 3.1 shows the results in the range up to 500 MV/m, together with a comparison with the experimental data of Grigoriev et al. (2008) on PZT 20/80, while the inset shows the computed behavior over the full range. The higher fields, above ~ 500 MV/m, are still outside the range that is achievable experimentally, even with pulsed-field techniques. We find that the strain increases monotonically over the entire range up to 1400 MV/m, with only a small tendency to begin saturating at the highest fields. In the range up to 500 MV/m, the results look very nearly linear. We obtain an excellent fit to the results with a simple quadratic form $\eta(E) = a_1 E + a_2 E^2$ (where $\eta_3 = \eta$ and $E_3 = E$ henceforth). The fitted values are $a_2 \simeq -0.01$ (m/GV)² and a_1 lying between 0.063 m/GV and 0.071 m/GV, where the quoted range reflects the choice of computer code.

The slopes of the curves in Fig. 3.1 are, of course, related to the piezoelectric response of the material. At finite field it is possible to define two slightly different piezoelectric coefficients $\tilde{d}_{33} = d\eta/dE$ and $d_{33} = dc/dV$, where $V = cE$ is the potential drop across a unit cell; from $d\eta = c^{-1}dc$ it follows that the definitions are related by $d_{33}^{-1} = \tilde{d}_{33}^{-1} + E$. We report d_{33} values here, consistent with the conventions of Grigoriev et al. (2008). However, the two definitions coincide at $E = 0$

and differ by only about 2% at 500 MV/m, so the difference is not significant in what follows. The results are presented in Fig. 3.2(a); we find a monotonically decreasing trend with electric field for both ABINIT and LAUTREC. However, the fall-off is quite slow, decreasing by only about 2-3% up to a field of 50 MV/m.

Other properties of PT under applied field show a similar, nearly linear behavior. In Fig. 3.2(b) we present the variations of the internal coordinates as a function of applied field (here computed using ABINIT, but similar results are obtained with LAUTREC). As expected, Pb and Ti ions, being positively charged, displace along the direction of the applied electric field, while O atoms displace in the opposite direction, thus increasing the ferroelectric mode amplitude. The Born effective charges Z^* , shown in Fig. 3.3(a), are almost independent of field, with only a mild reduction in their magnitudes with increasing field. However, at zero field the Z^* values under the epitaxial constraint are noticeably smaller in magnitude than their free-stress counterparts (Zhong et al. 1994). Since the Z^* 's are almost constant, we expect the electric polarization to increase with field in proportion to the displacements shown in Fig. 3.2(b), and Fig. 3.3(b) shows that this is indeed the case. A satisfactory fit of the form $P(E) = c_0 + c_1 E + c_2 E^2$ is obtained with $c_0 = 0.94$ C/m², $c_1 = 0.39$ C/(GV)m and $c_2 = -0.072$ C/(GV)². None of these quantities show any anomalous change with electric field.

We now return to a discussion of the strain response. Our theory is in qualitative agreement with the recent pulse-field data (Grigoriev et al. 2008), which show a nearly linear behavior similar to that predicted theoretically. The theory has a somewhat larger slope; our zero-field d_{33} of ~ 68 pm/V can be compared with their 45 pm/V. The agreement seems reasonable given that the materials are different (PT vs. PZT 20/80). Hints of a hump-like nonlinearity in the experimental data of Grigoriev et al. (2008) around 200 MV/m are not supported by the theory; if such a feature is really present, we would argue that it must arise

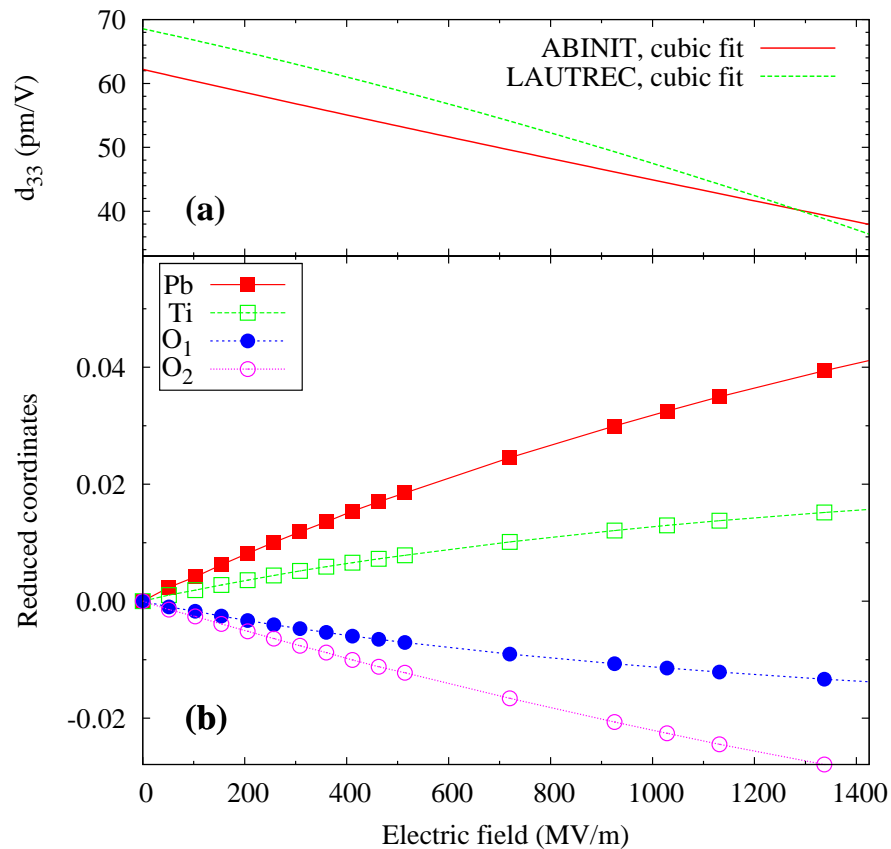


Figure 3.2: Variation of properties of tetragonal PbTiO_3 with electric field under in-plane epitaxial constraint. (a) Piezoelectric coefficient d_{33} (calculated with both codes). (b) Out-of-plane displacements of ions from zero-field positions (calculated with ABINIT).

from extrinsic effects not considered by the theory.

Our zero-field d_{33} is also significantly larger than the value of 45 pm/V obtained by the Landau-Devonshire theory for PZT 20/80 (Chen et al. 2003), which is in reasonable agreement with the zero-field value of Grigoriev *et al.* (For detailed comparisons, it should be kept in mind that the misfit of -0.5% reported in Chen et al. (2003) is only about half of that in Grigoriev et al. (2008).) However, our theoretical curves and the experimental data of Grigoriev *et al.* both show a much slower saturation of the strain response with field than was found by the Landau-Devonshire approach, where d_{33} was predicted to fall by about 15% already at 50 MV/m for PZT 20/80 with epitaxial constraint. Our d_{33} falls by only about 2-3% over the same range. The lack of saturation means that we predict large strains of about 3.0% at fields of around 500 MV/m, and we also predict a large polarization of about 1.10 C/m² at such fields. Possible reasons for the discrepancies between our results and those of the Landau-Devonshire theory will be discussed further in Sec. 3.3.3.

The Landau-Devonshire theory (Chen et al. 2003) also provided a zero-field value of 31 pm/V, falling by about 10% at 50 MV/m, for pure PT on an ST substrate. Recall that our calculations above were carried out at an in-plane lattice constant that was reduced by 1.14% relative to that of PT in order to model the strain state of PZT 20/80 in coherent epitaxy on a ST substrate. Therefore, in order to obtain a more direct comparison for the pure PT case, where the epitaxy with the ST substrate is almost perfect, we repeated our calculations with the in-plane lattice constant fixed to the theoretical equilibrium lattice constant of PT, finding a zero-field d_{33} of 50 pm/V. This is reduced somewhat from our value of 68 pm/V at -1.14% misfit, but still quite a bit larger than their value of 31 pm/V. Again, we find a very slow saturation (even slower than for the smaller in-plane lattice constant), in disagreement with the Landau-Devonshire theory.

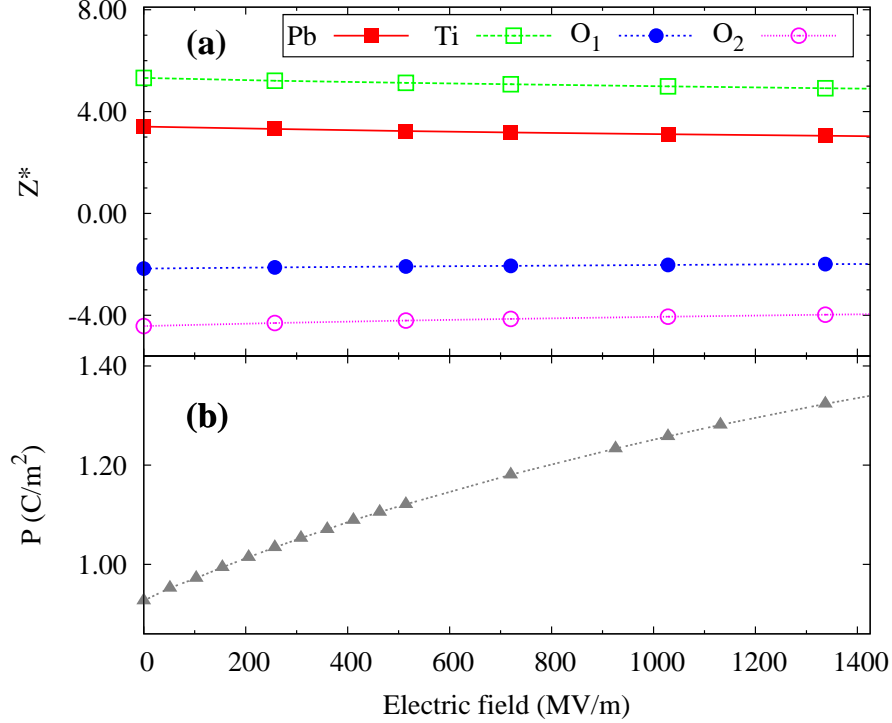


Figure 3.3: Variation of properties of tetragonal $PbTiO_3$ with electric field under in-plane epitaxial constraint, calculated with ABINIT. (a) Born effective charges. (b) Polarization.

3.3.2 Application of negative pressure and removal of epitaxial constraint

In this section we present the results of further investigations of the behavior of the system under modified elastic boundary conditions that are not directly relevant to the thin-film experiments. These investigations are motivated in part by previous *ab initio* calculations of Tinte et al. (2003) who showed that the c/a ratio and polarization of PT undergo an anomalous and strongly nonlinear variation as a function of an artificial applied negative pressure. The c/a ratio was found to increase gradually until the negative pressure reached about -4.8 GPa, where the c/a ratio rapidly increases to ~ 1.20 , with a subsequent slower increase up to ~ 1.25 at -7 GPa. Neither an electric field nor an epitaxial constraint were applied in that calculation, but the results nevertheless hint at a possible supertetragonal

state of PT that might be accessed under unusual boundary conditions. We also note that negative pressure is sometimes used to simulate the effect of chemical substitution, and that such an approach may be relevant here for providing hints about the behavior of PZT solid solutions. Zr and Ti belong to the same column of the Periodic Table, but Zr has a larger effective radius and will therefore tend to expand the lattice constant of PZT relative to pure PT; from the point of view of a Ti ion, this could produce a similar effect as is obtained from application of a negative pressure to pure PT.

Here, we explore the strain response as a function of both electric field and negative pressure, with and without the epitaxial constraint. The exercise is carried out in three steps. First, we apply a negative pressure in the presence of the epitaxial constraint, obtaining the strain response as a function of electric field. (In this case only the zz component of the stress tensor is relevant, and we could equally well say that we are applying a tensile uniaxial stress along c .) Second, we remove the negative pressure and repeat the calculations presented in Sec. 3.3.1, but without epitaxial constraint, so that the crystal is free to relax its in-plane lattice constants in response to the applied field. Finally, we combine the two steps described above and study the behavior as a function of electric field and negative hydrostatic pressure in the absence of any epitaxial constraint. Some results of this kind, both at zero and negative pressure, have already been presented in Stengel et al. (2009a).

Our present results for the application of negative pressure in the presence of the epitaxial constraint are shown in Fig. 3.4, where the strain plotted on the vertical axis is defined as relative to the c lattice constant at zero pressure and zero field. In this and subsequent figures we present calculations performed with the LAUTREC package. The zero-pressure curve duplicates the data presented in Fig. 3.1, while the ones at -1 and -2 show the enhancement in the strain

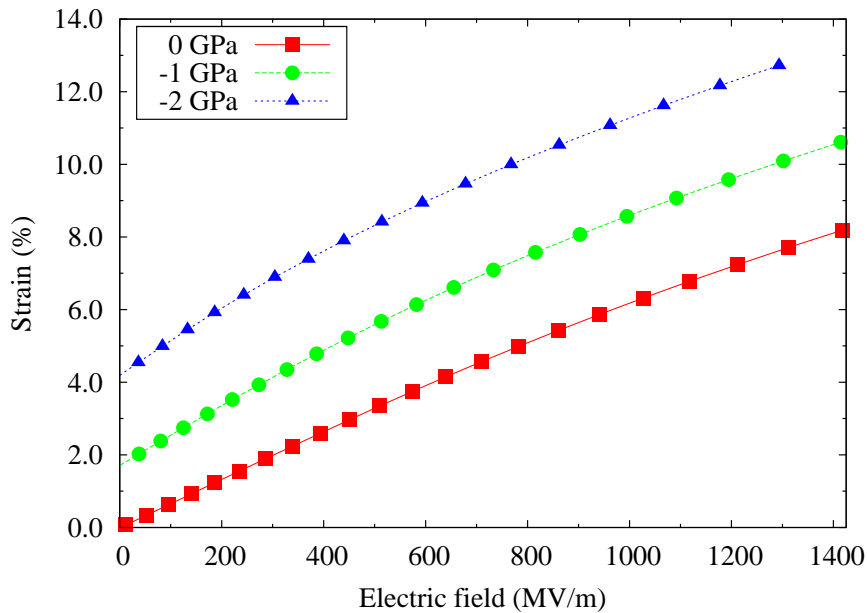


Figure 3.4: Field-induced strain, relative to zero-field zero-pressure state, for tetragonal PbTiO_3 under in-plane epitaxial constraint, calculated with LAUTREC.

caused by the negative pressure, which shifts the curves by about 2% per GPa. Otherwise they look rather similar, except that there is slightly more nonlinearity in the curves as the pressure becomes more negative.

The removal of the epitaxial constraint causes a much more drastic change in behavior, however, as shown by the square symbols (red curves) in Fig. 3.5. Both in-plane and out-of-plane strains are defined relative to the c lattice constant at zero field. As expected, the enhanced polarization and enhanced tetragonality induced by the field cause the out-of-plane lattice constant to grow, and the in-plane one to shrink, with increasing field. However, this variation shows an anomalous behavior: the change in strain starts out slowly at lower fields, accelerates and occurs most rapidly at a characteristic field $E_{\text{anom}} \simeq 550$ MV/m, and then slows again at higher fields. This anomalous behavior is most evident in the curve for the out-of-plane strain, but is also visible for the in-plane strain. The anomaly also shows up clearly in the behaviors of the piezoelectric coefficient and internal displacements (especially those of O_2), presented in Fig. 3.6(a) and (b)

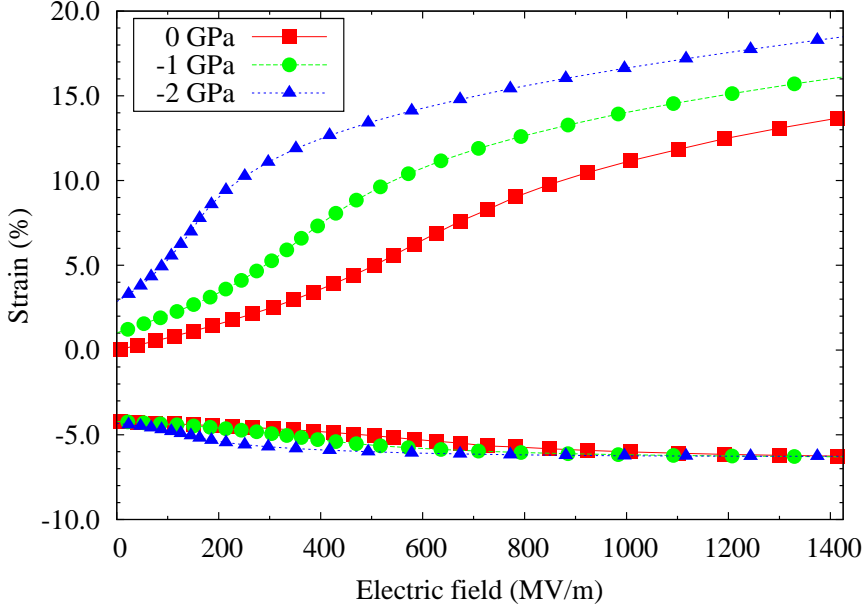


Figure 3.5: Field-induced strain, relative to out-of-plane lattice constant of zero-field zero-pressure state, for tetragonal PbTiO_3 under free-stress (0 GPa) and negative-pressure (-1 and -2 GPa) boundary conditions, calculated with LAUTREC. Top curves: out-of-plane strain. Bottom curves: in-plane strain.

respectively.

Finally, the remaining curves in Fig. 3.5 show how this behavior evolves as a negative pressure is applied. The anomaly becomes more pronounced as the pressure becomes more negative, with E_{anom} shifting to lower fields of about 375 and 150 MV/m at -1 and -2 GPa respectively. (This behavior was also presented in Stengel et al. (2009a) in terms of reduced electrical coordinates.) Very large strains (with c/a ratios approaching 1.25) occur at the largest fields and strongest negative pressures considered. The behaviors are similar to those already reported in Tinte et al. (2003) as a function of negative pressure alone, but here we find that the application of an electric field works cooperatively with the negative pressure to induce the crossover into the supertetragonal state (Stengel et al. 2009a).

Returning to the zero-pressure results, we can now compare these more directly with previous works in which the epitaxial constraint was absent. As was

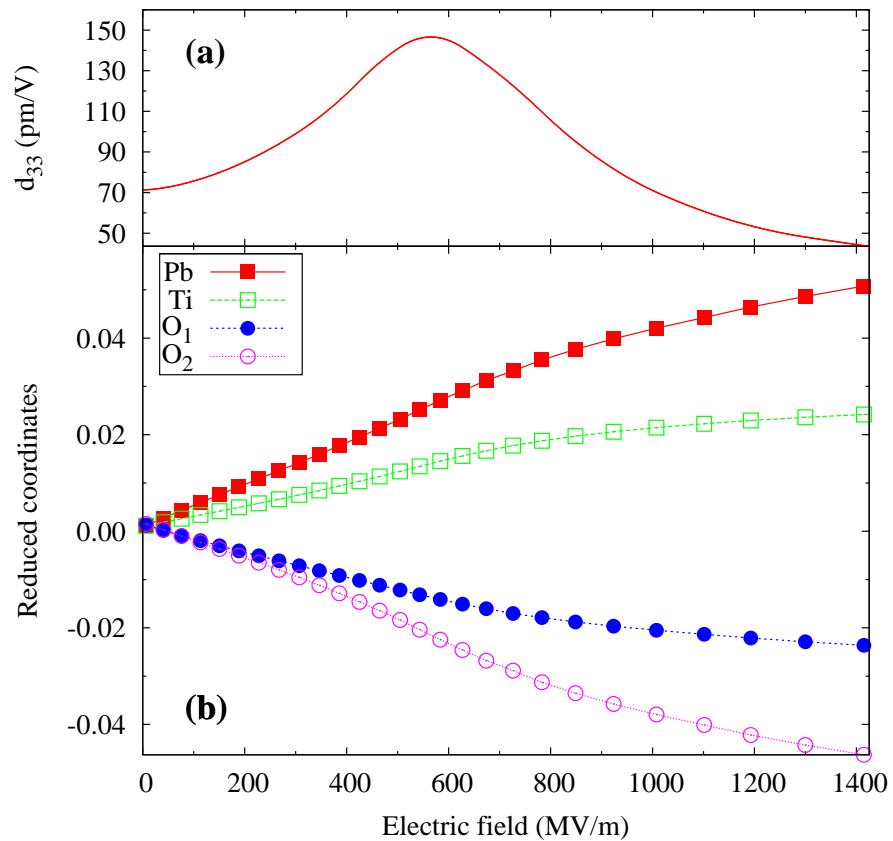


Figure 3.6: Variation of properties of tetragonal PbTiO_3 with electric field under free-stress boundary conditions, calculated with LAUTREC. (a) Piezoelectric coefficient d_{33} . (b) Out-of-plane displacements of ions from zero-field positions.

shown in Fig. 3.6(a), we find that d_{33} starts at about 70 pm/V at zero field, increases up to about 140 pm/V near $E_{\text{anom}} = 550$ MV/m, and then falls again at higher fields. The results of Sai et al. (2002) instead show d_{33} starting at 39 pm/V and decreasing monotonically as the field is increased. The discrepancy with respect to our results may be attributed to the more approximate methods used in Sai et al. (2002), where the electric field was applied in an approximation in which extra forces appear on the atoms in proportion to the Born effective charges computed at zero field (Sai et al. 2002; Fu & Bellaiche 2003). The Landau-Devonshire results of Chen et al. (2003) also show d_{33} decreasing monotonically with field, but starting from a zero-field value of 79 pm/V that is closer to ours. The comparison between their work and ours deserve further comment, as will be provided in the next section.

3.3.3 Discussion

In this section we discuss some of the factors that need to be considered when comparing our theoretical calculations with previous theory and experiment. We focus first on three important considerations, namely, the elastic boundary conditions (epitaxial vs. free-stress), the reference in-plane lattice constant, and the Zr content. We then discuss several other factors that may also play a significant role. Some comparisons have already been made along these lines in Sec. 3.3.1, but we concentrate here on possible mechanisms and physical explanations for the observed trends.

Reference in-plane lattice constant

When applying the epitaxial constraint, we have a choice of which in-plane lattice constant a to use for the comparison. As explained earlier, most of our results are reported for a value of a that is 1.14% smaller than the equilibrium lattice

constant of PT, to facilitate comparison with the experiment of Grigoriev et al. (2008) on PZT 20/80. If instead we repeat the calculations by fixing a to be that of tetragonal PT at its theoretical equilibrium lattice constant, as mentioned earlier near the end of Sec. 3.3.1, we find a zero-field d_{33} of about 50 pm/V, to be compared with the value of about 68 pm/V obtained at the smaller lattice constant with LAUTREC code. This trend is understandable since one may expect a larger d_{33} in a more tetragonal material. It is also consistent with the trend shown in Fig. 4(a) of Chen *et al.*, where d_{33} increases from 39 to 58 pm/V when the epitaxial constraint is made 1% more compressive.

Epitaxial vs. free-stress boundary conditions

Our work reinforces the expectation that the choice of epitaxial vs. free-stress elastic boundary conditions plays a crucial role in the piezoelectric response. This is true already at zero field, but the effect becomes enormous for elevated fields.

At zero field, one expects the free-stress d_{33} to exceed the epitaxial one, other things being equal. This can be understood as follows. If we start from the relaxed tetragonal ferroelectric PT crystal and apply an enhancing electric field along z with the in-plane a fixed, we can decompose the response according to a two-step process. First, we apply the field while allowing a and c to relax. We expect the degree of tetragonality to increase along with P , so that a shrinks while c grows, as confirmed by Fig. 3.5. Second, we enlarge a back to its zero-field value, again while allowing c to relax; since the Poisson ratio is positive, this should cause c to shrink. Thus, d_{33} should be smaller in the epi-constrained case. This is true in the work of Chen et al. (2003), where for example the zero-field d_{33} decreases from 79 to 31 pm/V for pure PT, and from 87 to 45 pm/V for PZT 20/80, when going from free-stress to epi-constrained boundary conditions. It is also confirmed in our calculations on pure PT; we find that the zero-field d_{33} decreases from 71 to

50 pm/V (LAUTREC values) in going from the free-stress to the epi-constrained case.

As indicated earlier, we find a drastic difference in the *non-linear* response when we remove the epitaxial constraint, with the smooth decrease of d_{33} in Fig. 3.2(a) replaced by the rapid increase and peak around 550 MV/m in Fig. 3.6(a). This peak is clearly a signature of the crossover into the supertetragonal state.

Zr content

Of course, it is important to keep track of the differences between pure PT and PZT with different Zr concentrations, as we have tried to do consistently above. As is well known, PZT is often preferred as a more practical material for experimental purposes and for applications because of reduced leakage currents and other beneficial properties. The work of Chen Chen et al. (2003) reports d_{33} increasing from 79 to 87 pm/V in going from pure PT to PZT 20/80 in the free-stress case, and from 31 to 39 pm/V in the epi-constrained case at zero misfit. If this trend is correct, it is in the wrong direction to explain the difference between our theory and the experiment of Grigoriev et al. (2008), since our d_{33} values for pure PT are larger than theirs for PZT 20/80. Other factors may be responsible for this discrepancy, as discussed in the next subsection. Ideally it would be advantageous if the pulsed-field experiments could be carried out on a series of samples of varying Zr content so that an extrapolation could be made to the pure-PT case, allowing a more direct comparison with theory.

Other factors

Here we comment briefly on a number of other factors that might play a role when comparing our results with experiment. Our theory is purely a zero-temperature

theory, and also completely neglects the effects of disorder arising from Zr configurations in PZT, or from defects such as oxygen vacancies even in pure PT. Both disorder and thermal fluctuations may tend to cause the local polarization direction to fluctuate about the global tetragonal axis, and it is well known that polarization rotation can generate large electromechanical responses in this class of materials (Fu & Cohen 2000). At larger length scales, it is also possible that the samples might not be in a perfect single-domain state, with the incomplete switching being caused by defects, roughness, or other imperfections in the thin-film samples. In such a case, the intrinsic piezoelectric response would be underestimated, while extrinsic contributions associated with domain-wall motion might also be present. For ultrathin films, depolarization effects and the influence of the perovskite-electrode interfaces (Stengel et al. 2009b,c) will also play an important role. We expect that these issues will be clarified as improved methods of sample preparation become available, and as systematic studies are done to see how the piezoelectric responses depend on film thickness and other properties.

3.4 Summary

In summary, we have studied the piezoelectric response of PbTiO_3 to a polarization-enhancing electric field applied along the tetragonal axis under several kinds of mechanical boundary conditions. In the epitaxially constrained regime we find hardly any saturation of the piezoelectric coefficient d_{33} up to a field of 500 MV/m, in agreement with recent experimental measurements and in contrast with the predictions of Landau-theory expansions. With the removal of the epitaxial constraint we find a remarkable non-linear effect, with d_{33} rising to twice its zero-field value at ~ 550 MV/m and then decreasing again for higher applied fields.

The comparison between ABINIT and LAUTREC shows fairly good agreement. Some quantitative discrepancies do exist (e.g., in equilibrium lattice constants); these can be traced to the sensitivity of PbTiO_3 to the choice of pseudopotentials. Nevertheless, the trends in the two calculations are very similar. Moreover, extensive tests show that the dissimilarities in the finite-field techniques (constrained- E with Berry phase in ABINIT vs. constrained- D with Wannier functions in LAUTREC) have little or no impact on the calculated properties, once the subtleties in the treatment of the electrical and strain variables have been properly accounted for.

Quantitative comparisons with experiment still present a formidable challenge, in part because it remains difficult to characterize the precise sample conditions underlying a given electrical measurement. However, significant progress has now been made on the theoretical side, and experimental control of film properties continues to improve. Thus, we hope that direct comparisons between theory and experiment regarding nonlinear piezoelectric behavior will provide an increasingly fruitful avenue for future investigations.

Chapter 4

Theory of prospective perovskite ferroelectrics with double rock-salt order

4.1 Introduction

Recent interest in novel materials has been stimulated by unprecedented advances both in experimental materials synthesis and in first-principles computational methods for predicting materials properties. Attention has focused in particular on functional materials that can be driven between various structural or electronic phases having distinct properties, as for example by the application of electric fields, magnetic fields, or strain.

Ferroelectric perovskites constitute a subset of these interesting compounds, with their switching behavior providing potential applications in non-volatile memories and their piezoelectric properties making them attractive as actuators and sensors. The perovskites are also of considerable interest in the search for multiferroics having strongly coupled polar and magnetic properties. Recent work has shown that many perovskite properties can be tuned through the application of epitaxial strain (Rabe 2005; Ederer & Spaldin 2005; Diéguez et al. 2005; Fennie & Rabe 2006; Lee & Rabe 2010).

Ferroelectric perovskite oxides can generally be classified into those derived from cubic symmetry, meaning that the actual or putative high-temperature symmetric phase is cubic, or those derived from tetragonal symmetry, meaning that the high-symmetry phase is tetragonal. Most well-known ferroelectrics, including

BaTiO₃, KNbO₃, PbTiO₃, and BiFeO₃ belong to the first class, while some layered ferroelectrics, such as SrBi₂Ta₂O₉, (Stachiotti et al. 2000; Tsai et al. 2003; Perez-Mato et al. 2004) belong to the latter. It is possible for the compositional ordering in tetragonal layered systems to break inversion symmetry, as for example in “tricolor” superlattices (Sai et al. 2000; Warusawithana et al. 2003; Lee et al. 2005; Wu et al. 2008). To our knowledge, however, there are no perovskite oxides in which the chemical composition corresponds to a *tetrahedral* high-symmetry structure. While some boracites (M₃B₇O₁₃X, where M is usually a divalent metal and X is usually a halogen) such as Ni₃B₇O₁₃I are realizations of this kind of tetrahedral ferroelectric system (Ascher et al. 1966; Schmid 1970; Nelmes 1974), it would be very interesting to see the same symmetry class represented in the better-known case of perovskite oxides.

The present work is motivated by the idea that perovskite oxides having a tetrahedral high-symmetry structure might be realized experimentally and might have interesting ferroelectric or other physical properties. With this in mind, we have carried out a computational study, based on first-principles density-functional calculations, of perovskites having a tetrahedral compositional symmetry. In particular, we focus on AA'BB'O₆ double perovskites in which both A and B sites exhibit rock-salt order. Of course, the local bonding environment, based on corner-sharing oxygen octahedra, would remain similar to other perovskites. While rock-salt order on the B site of a double perovskite is common, it is quite rare on the A site, where a 50% mixing of two atoms typically leads to (001) layered ordering if it orders at all. Nevertheless, even if the tetrahedral symmetry is not realized in the equilibrium phase diagram, we point out that experimental routes to the directed synthesis of such double-rock-salt tetrahedral AA'BB'O₆ perovskites may be available, as demonstrated for example in the recent work of Rijnders et al. (2010).

The chapter is organized as follows. Sec. 4.2 introduces the structure of the $AA'BB'O_6$ perovskite materials, describes the possible symmetry-determined directions of the polarization, and discusses possible domain types and their symmetries. This section begins with a subsection where we discuss various types of cation ordering in perovskites, which would help us appreciate the uniqueness of the double rock-salt ordering in $AA'BB'O_6$ perovskites. We then briefly detail our theoretical methods in Sec. 4.3. Next, Sec. 4.4 describes the results of our first-principles calculations and presents a comparison with a simple empirical model. We also discuss the effects of rotations of oxygen octahedra, and present some results concerning a Mn-containing double perovskite in which magnetic ordering is also an issue. Finally, in Sec. 4.5 we summarize our work and present our conclusions.

4.2 Tetrahedral $AA'BB'O_6$ double perovskites with rock-salt order

The five-atom perovskite with a chemical formula ABO_3 (or ABX_3 more generally) has cubic symmetry and belongs to the $Pm\bar{3}m$ space group. The B cations are usually smaller than the A cations, and they are octahedrally coordinated by the X anions. A cations have twelve X anion around them. Many properties that perovskites exhibit arise from, or get significantly modified when, various distortions, such as octahedral tilting, lower the symmetry from the high-symmetry cubic structure to a lower-symmetry structure. A good control over these distortions enables the fine tuning of material properties, and is an essential aspect of designing new materials. The variety of properties in perovskites is largely due to this structural flexibility that they possess. Equally important, however,

is the *compositional* flexibility perovskites show. This includes both ordered and disordered systems. It is possible to make chemical substitutions in all of A, B and X sites. While an increase in disorder degrades some responses (e.g., magnetotransport properties of half-metallic ferrimagnets, such as $\text{SR}_2\text{FeMoO}_6$ (Sarma 2001)), it enhances, or is responsible for certain other properties. An example is the conversion of normal ferroelectrics, with increase in Sc/Ta disorder in systems like $\text{Pb}_2\text{ScTaO}_6$, into relaxor ferroelectrics (Burton & Cockayne 1999).

The route to exploiting the compositional flexibility starts with doubling just one, or both, of the cations of the ABO_3 system, to make $\text{A}_2\text{BB}'\text{O}_6$, $\text{AA}'\text{B}_2\text{O}_6$, and $\text{AA}'\text{BB}'\text{O}_6$ systems. Of course one may continue with introducing more variety, or more of the same cations to make these systems more complex for specific purposes. In this short subsection, however, we keep our focus on systems in which the number of cations is doubled.

For either the A-site or the B-site cations, there are three possible arrangements: rock-salt ordering, columnar ordering, and layered ordering (Knapp & Woodward 2006; Davies et al. 2008; King & Woodward 2010). In the rock-salt ordering, the B and the B' (or the A and the A') atoms form a rock-salt lattice, a 3D checkerboard pattern. In such a lattice, starting with a cation site A (B), the next A (B) site is occupied by A' (B') in all three directions. However, if the A and the A' alternate in two directions, while having the same species in the remaining direction, we have a columnar arrangement. The definition is the same for B cations. Similarly, if A (B) and A' (B') atoms alternate only in one direction, we have layered ordering. The atoms alternate in the direction perpendicular to the layers.

There are two factors which primarily determine the nature and the degree of ordering - the electrostatic charges of the ions, and their relative sizes. If we assume that A and A' (or B and B') are differently charged, then from the

standpoint of electrostatic interactions alone, it is favorable to arrange them in the rock-salt order for both A and B sites. This is easy to understand: the rock-salt arrangement creates a maximum separation between similar atoms, and it pays to keep them as far apart as possible if there is a big charge difference between A and A' (or B and B'). Similar reasoning leads to the conclusion that the electrostatic interaction favors rock-salt ordering more than the columnar ordering, which in turn is favored more than the layered ordering.

While electrostatic interaction is important, compounds made of similarly charged A and A' (or B and B') cations, one big and the other small, often follow arrangements dictated by the size effects mediated by anion ordering. In a perovskite structure an anion is surrounded by two B-site cations and four A-site cations. The two B-site cations and the anion are arranged on a straight line, while the anion resides on the plane formed by the four A-site cations. If there is a substantial size difference for the B and B' ions, it is easier for the anion to shift towards the smaller of the B-site atoms, however, if A and A' are placed in rock-salt order, the anion cannot move in any direction (including the direction *off the plane*) to relieve this stress. It becomes a lot easier for the anion if the A-site cations are arranged in layers, which encourages the anion to move towards the layer containing the smaller of the A-site atoms. Actually two-thirds of the anions can take advantage of this, while the remaining one-third of anions are stuck in either the plane containing all A, or the one with all A'.

Such differences in the bonding environment are usually not preferred, although other types of structural adjustment, such as octahedral rotation, can help stabilize such situations. This explains why there are many fewer cases of A-site ordering compared to B-site ordering, and when we do see it, the overwhelming majority has rock-salt ordering for the B sites and layered ordering for the A sites. The columnar ordering for both A and B sites also involves such

Table 4.1: Possible cation ordering in double perovskites with examples and the corresponding high-symmetry space groups. ‘(R)’, ‘(C)’ and ‘(L)’ denote rock-salt, columnar and layered ordering in the left most column.

Site (ordering)	High-symmetry space group	Example	Comments
B(R)	$Fm\bar{3}m$	Ba ₂ MgWO ₆	
B(C)	$P4/mmm$	NdSrMn ³⁺ Mn ⁴⁺ O ₆	Disordered on A sites
B(L)	$P4/mmm$	La ₂ CuSnO ₆	
A(R)	$Fm\bar{3}m$	NaBaLiNiF ₆	Disordered on B sites
A(C)	$P4_2/nmc$	CaFeTi ₂ O ₆	
A(L)	$P4/mmm$	YBaMn ₂ O ₆	
B(R), A(L)	$P4/mmm$	NaLaMgWO ₆	
B(R), A(R)	$F\bar{4}3m$?	Current focus

difference in bonding environments for anions, and usually takes place with the help from other structural adjustments. In Table 4.1 we list examples of these arrangements, along with the space groups they belong to.

So far in this section we have discussed various possible double cation ordering of perovskites, without going into any detail about how such ordering affects their properties. In the remainder of this section we will investigate a unique and theoretically-possible polarization behavior and focus on a specific type of double ordering, namely, rock-salt ordering on both A and B sites, which allows such behavior.

We consider here a class of perovskite ferroelectrics whose compositional symmetry, and thus the high-temperature symmetric phase, is tetrahedral, instead of cubic or tetragonal. The simplest way to arrive at tetrahedral symmetry in the perovskite system is to populate both A and B sites with two different kinds of atoms (A and A', and B and B', respectively) arranged in rock-salt (three-dimensional checkerboard) order (Table 4.1). A recent survey (King & Woodward 2010) states that long-range A-site rock-salt ordering is known only for two compounds, neither of which has B-site order (Ducau et al. 1992). Thus, to our knowledge, no perovskite oxides exhibiting *simultaneous* A- and B-site rock-salt

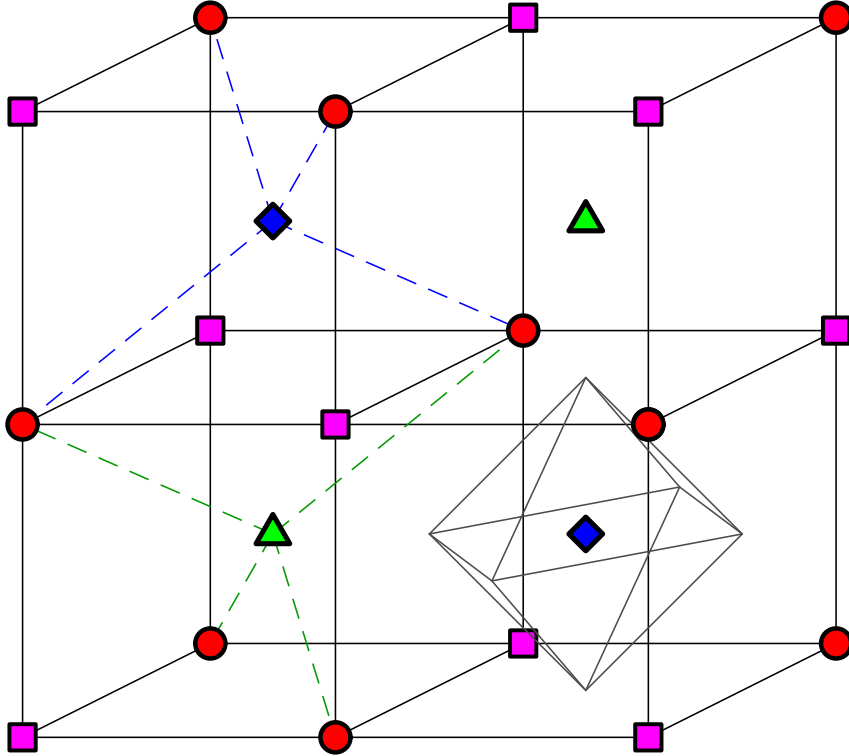


Figure 4.1: Structure of $AA'BB'O_6$ double perovskites, with A (red circles) and A' (magenta squares) atoms forming one rock-salt framework, and B (blue diamonds) and B' (green triangles) atoms forming a second interpenetrating one. Oxygen atoms are not shown, although one oxygen octahedron is outlined to clarify that the local bonding environment is still roughly octahedral. Dashed lines illustrate the tetrahedral point symmetry.

ordering has been reported. Nevertheless, we shall investigate their properties theoretically here.

The structure in question is illustrated in Fig. 4.1, in which oxygen atoms are suppressed for clarity. It can be seen that the point symmetry of each atom is tetrahedral, and since there is only one formula unit per primitive cell, this also establishes the crystal point group as tetrahedral, with the $F\bar{4}3m$ space group (216). This then identifies the parent high-symmetry structure, and can be compared with the $Pm3m$ high-symmetry structure that characterizes most ordinary perovskite ferroelectrics.

In such a tetrahedral ferroelectric, the symmetry of the energy landscape

$E(\mathbf{P})$ is such that E will be stationary with respect to the direction of \mathbf{P} for \mathbf{P} along $\langle 111 \rangle$, $\langle \bar{1}\bar{1}\bar{1} \rangle$, and $\langle 100 \rangle$ directions. If there are local minima along these directions, they correspond to the rhombohedral $R3m$ space group (160) in the first two cases, or the orthorhombic $Imm2$ space group (44) in the last case. This is illustrated in Fig. 4.2, where panels (a-c) illustrate the usual case of cubic perovskites, while panels (d-f) show the corresponding possibilities in the tetrahedral perovskite system. If the rhombohedral directions are energetically favored, as in panels (d-e), then there will be two distinct types of rhombohedral domains with different energies, and the dependence of the total energy on P for $\mathbf{P} = P\hat{n}$ along the body diagonal \hat{n} will display an asymmetric double-well potential. This is in sharp contrast with systems like $A_2BB'O_6$ or $AA'B_2O_6$, in which only one sublattice has rock-salt order; the symmetry is then that of panels (a-c), and the magnitude of the polarization does not change when the polarization is reversed during a domain switching event.

Even if these perovskites with double rock-salt order do not exist as equilibrium phases, it may be possible to synthesize them using atomic-layer epitaxy techniques. In order to access the desired compositional order, this would need to be done by epitaxial growth on the (111) perovskite surface orientation. As a proof of principle, Rijnders, Blok and Blank have recently reported such a growth of $SrCaTiMnO_6$ and $CaBiTiFeO_6$ films on $LaAlO_3$ and $SrTiO_3$ substrates (Rijnders et al. 2010). Interestingly, a symmetry analysis shows that a (111) uniaxial strain, of the kind that results from a lattice mismatch in this kind of epitaxial geometry, would convert the system to a polar space group by selecting out one of the body-diagonals as special, resulting in a polarization even when none is present in the high-symmetry tetrahedral structure. A related effect, in which improper ferroelectricity can be induced by octahedral rotations around a body-diagonal direction, will be discussed in Sec. 4.4.4.

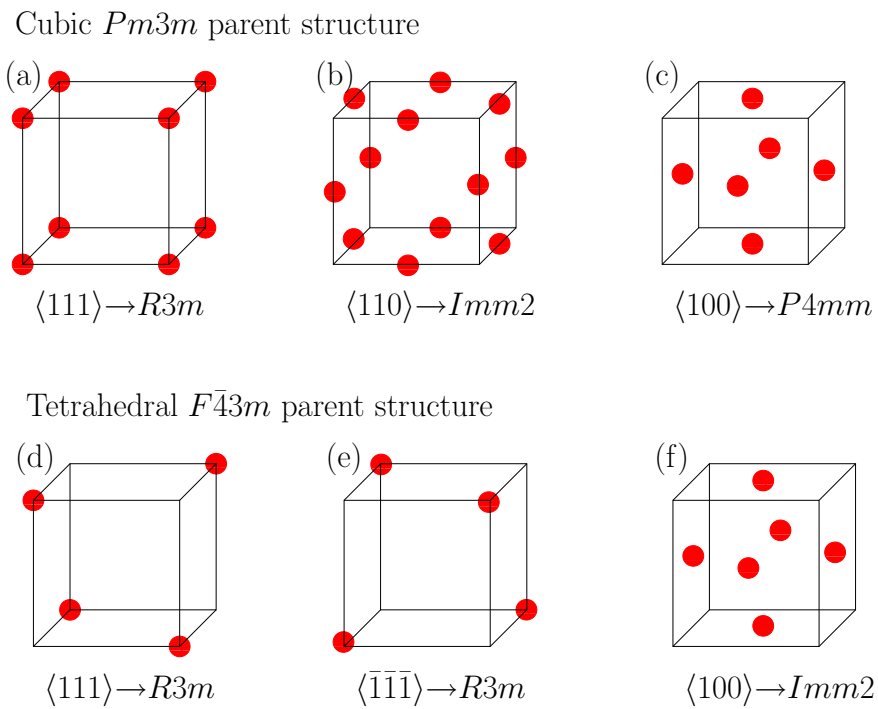


Figure 4.2: Symmetry-determined possibilities for directions of energy minima in the space of polarization, represented by red dots. Fig. (a)-(c) cubic composition leading to high-symmetry $Pm\bar{3}m$ structure, and (d)-(f) tetrahedral composition leading to high-symmetry $F\bar{4}3m$ structure.

4.3 Computational details

The calculations are performed using density-functional theory (DFT) as implemented in the ABINIT code package (Gonze et al. 2002, 2005, 2009). We use Ceperley-Alder (Ceperley 1978; Ceperley & Alder 1980) exchange-correlation in the Perdew-Wang(Perdew & Wang 1992) parameterization, and Troullier-Martin norm-conserving pseudopotentials constructed using the FHI98PP (M. Fuchs 1999) code. A plane-wave cutoff of 70 Hartree is applied. The Brillouin zone of the 10-atom fcc cell is sampled by a $6 \times 6 \times 6$ Monkhorst-Pack (Monkhorst & Pack 1976) k -point mesh, while that for the 20-atom unit cell is $6 \times 6 \times 4$. (Energy differences between a low-symmetry and a high-symmetry structures are always computed using an identical cell and k -point mesh.) A stress threshold of 2×10^{-2} GPa is used for cell relaxation, and forces on ions are converged below 2.5×10^{-3} eV/Å. The electric polarization is calculated using the Berry-phase approach (King-Smith & Vanderbilt 1993). To avoid any potential confusion in the branch choice for the polarization of non-orthogonal unit cells, we also estimated the polarization using the computed Born effective charge tensors and atomic displacements, finding good agreement.

In addition to ground-state relaxation calculations, we also use density-functional perturbation theory to compute the frequencies of the zone-center phonon modes, as an aid in identifying polar or nonpolar (e.g., octahedral rotation) instabilities. To this end, the phonon frequencies at the Γ point of the 10-atom cell (corresponding to both Γ and R points of a 5-atom cubic cell) were calculated, and the corresponding soft-mode eigenvectors were analyzed for any unstable modes having imaginary frequency. The plane-wave cutoff and other details were the same as for the ground-state calculations.

Table 4.2: Compounds for which calculations have been carried out. Second column gives the acronym that we use to identify the compound. Lattice constants are calculated in the high-symmetry $F\bar{4}3m$ structure and are reported in terms of an effective 5-atom cubic cell dimension. “Average” refers to the average computed lattice constant of the ABO_3 , $A'BO_3$, $AB'O_3$, and $A'B'O_3$ parent materials.

Compound	Alias	Lattice constant (a.u.)	
		Calculated	Average
$PbSnTiZrO_6$	PSTZ	7.47	7.47
$KCaZrNbO_6$	KCZN	7.55	7.55
$CaBaTiZrO_6$	CBTZ	7.54	7.53
$KSrTiNbO_6$	KSTN	7.35	7.33
$KBaTiNbO_6$	KBTN	7.47	7.48
$SrCaTiMnO_6$	SCTM	7.15	7.20

4.4 Results

4.4.1 High-symmetry states

As mentioned in Sec. 4.1, rock-salt ordering is not a common form of ordering on the A site of mixed perovskites, and we are not aware of any naturally-occurring $AA'BB'O_6$ double perovskites that exhibit rock-salt ordering on both A and B sites. Therefore, our first step has been to carry out a theoretical search for potential candidate materials of this kind. Even if the double rock-salt ordering is not the ground-state equilibrium structure for a given material, it could be a candidate for attempts at directed experimental synthesis. Thus, we have carried out calculations for a variety of compounds, placing each in the high-symmetry $F\bar{4}3m$ structure and minimizing the energy with respect to the lattice constant. We look for materials that are insulating, and select possible candidates showing a range of ionic sizes, or combinations of cationic charges. For example, we consider combinations where both parent perovskites have +2 and +4 cations, or those with one parent perovskite having +1 and +5 cations while the other has +2 and +4 cations. This search led us to focus on the six candidate materials that are

listed in Table 4.2. The second column of this Table gives the alias by which each compound will be denoted in the remainder of the chapter (“PSTZ” for PbSnTiZrO_6 , etc.).

The third column of Table 4.2 presents our calculated lattice constants for the $\text{AA}'\text{BB}'\text{O}_6$ double perovskites. In order to put these in context, we also calculate the cell constants of all relevant parent perovskites in their high-symmetry $Pm\bar{3}m$ structure. Then, for each of these six compounds, we average the calculated lattice constants of the four parent materials (even if some were occasionally metallic) and present the result as the last column of Table 4.2. In each case we find that the cell constant of the double perovskite is very close to average of the parents. For PSTZ, for example, we find that the parents PbTiO_3 , PbZrO_3 , SnTiO_3 and SnZrO_3 have cell constants of 7.30, 7.70, 7.23 and 7.66 a.u. respectively. The corresponding arithmetic average is 7.47 a.u., essentially the same as the calculated value for PSTZ. The fact that the agreement is so good for all six cases indicates that the volumes of the parent simple perovskites essentially determine the cell constants of the double perovskites in the rock-salt structure. (Note that the results reported for SCTM are calculated in the high-symmetry ferromagnetic spin state, even though the antiferromagnetic structure is lower in energy; we do this to stay in the spirit of reporting the high-symmetry behavior here. More realistic spin structures will be considered in Sec. 4.4.5.)

4.4.2 Exploration of polar instabilities

Next we look for ferroelectric instabilities in these systems by checking the high-symmetry $F\bar{4}3m$ structures to see if there are any phonon modes with imaginary frequency. Because of the high symmetry, all phonon modes at Γ have three-fold degeneracy. After identifying and discarding the triplet corresponding to the zero mode (uniform translation), we report the lowest relevant mode frequencies in the

Table 4.3: Frequency and principal character of lowest zone-center mode, and same for next-higher mode, in the $F\bar{4}3m$ structure for $AA'BB'O_6$ materials.

AA'BB'	Phonon I		Phonon II	
	ω (cm ⁻¹)	char.	ω (cm ⁻¹)	char.
PSTZ	182 <i>i</i>	O only	160 <i>i</i>	A', O
KCZN	195 <i>i</i>	O only	96 <i>i</i>	A', O
CBTZ	147 <i>i</i>	O only	75 <i>i</i>	A, O
KSTN	103 <i>i</i>	O only		
KBTN	149	A, A', O		
SCTM	172 <i>i</i>	O only		

second and fourth columns of Table 4.3. We also inspect the mode eigenvectors and report the character of these modes in the third and fifth columns of the Table.

We find that KBTN does not exhibit any unstable modes, suggesting that it is probably stable (or, at least, metastable) in the $F\bar{4}3m$ structure. Turning now to the other five materials, we see that there are *two* sets of unstable soft modes for the first three materials, while there is only one for KSTN and SCTM. Moreover, the most unstable mode always has character only on oxygen atoms, indicating that it corresponds to a pattern of octahedral tilts or rotations. Since this occurs at the Γ point of the 10-atom cell, it corresponds to an R -point instability of the 5-atom parent perovskite. (We shall consider rotational instabilities further in Sec. 4.4.4.) However, if we look at the other set of unstable modes for each of the first three materials, we observe a large contribution coming from the smaller of the A ions, signaling that they are polar (i.e., infrared-active) distortions. We henceforth focus our attention on an in-depth study of the first three materials, namely CBTZ, KCZN and PSTZ.

As discussed in Sec. 4.2, a ferroelectric distortion along one of the Cartesian directions leads to a polarized structure in the $Imm2$ space group, while the evolution of a polarization along the $\langle 111 \rangle$ or $\langle \bar{1}\bar{1}\bar{1} \rangle$ directions leads to the $R3m$

Table 4.4: Calculated polarization and total-energy reduction (relative to the high-symmetry $F\bar{4}3m$ structure, per 10-atom cell) for distorted structures of CBTZ, KCZN, and PSTZ. Last four columns present results obtained from the models discussed in Sec. 4.4.3 (values in parentheses are exact by construction, as they were used as input to the fit).

Material	Space group	<i>Ab-initio</i> results		Landau-Devonshire model			
		Polarization C/m ²	Energy meV	Fourth order meV	% error	Fifth order meV	% error
CBTZ	$R3m\langle 111 \rangle$	0.137	10.8	11.2	3	(10.8)	(0)
	$R3m\langle \bar{1}\bar{1}\bar{1} \rangle$	0.136	11.5	11.1	3	11.5	0
	$Imm2\langle 100 \rangle$	0.163	16.0	(16.0)	(0)	(16.0)	(0)
KCZN	$R3m\langle 111 \rangle$	0.186	24.9	26.4	6	(24.9)	(0)
	$R3m\langle \bar{1}\bar{1}\bar{1} \rangle$	0.184	27.2	26.0	4	27.5	1
	$Imm2\langle 100 \rangle$	0.219	36.6	(36.6)	(0)	(36.6)	(0)
PSTZ	$R3m\langle 111 \rangle$	0.777	681.4	713.1	5	(681.4)	(0)
	$R3m\langle \bar{1}\bar{1}\bar{1} \rangle$	0.837	794.0	799.6	1	839.5	6
	$Imm2\langle 100 \rangle$	0.709	581.8	(581.8)	(0)	(581.8)	(0)

space group. For each material we follow the system into its local symmetry-constrained ground state for each type of distortion, and we also compute the electric polarization in this state using the Berry-phase method. (Polarizations found by multiplying computed Z^* values times computed displacements differ only slightly from those calculated using the Berry-phase approach.) The results are presented in the first four columns of Table 4.4, where the energies are reported relative to that of the high-symmetry $F\bar{4}3m$ structure. (Note that $\langle 111 \rangle$ denotes the direction from an A atom to a B neighbor, while $\langle \bar{1}\bar{1}\bar{1} \rangle$ points to a B' neighbor.)

We see that for CBTZ and KCZN the $Imm2$ structure is energetically preferred over the $R3m$ structures, and the polarizations are also larger for the $Imm2$ structure. In these materials, the energies and polarizations are also very similar for the structures distorted along $\langle 111 \rangle$ and $\langle \bar{1}\bar{1}\bar{1} \rangle$ directions. On the other hand, the PSTZ system behaves very differently. It is strongly polar, with the depth of the double-well potential, at 0.6-0.8 eV, being more than an order of magnitude

larger than for the other two materials. Furthermore, the $R3m$ structure denoted as $\langle \bar{1}\bar{1}\bar{1} \rangle$ is now the favored structure, being significantly lower in energy than either the $\langle 111 \rangle$ $R3m$ structure or the $Imm2$ structure. This structure also has the largest polarization, at 0.837 C/m^2 .

We thus see that $AA'BB'O_6$ double perovskites can have a rich variety of polar behaviors, ranging from ones that remain nonpolar like KBTN, to those that are weakly polar like CBTZ and KCZN, and finally to the case of the strongly polar PSTZ. In the next subsection we shall see how this diversity of behaviors can be captured in a simple analytical model.

Before doing so, we comment briefly on the nature of the ferroelectricity seen in these tetrahedral ferroelectrics. For this purpose, we have inspected the eigenvectors of the ferroelectric soft modes identified in Table 4.3. Letting ξ_μ be the sum of squares of soft-mode eigenvector components corresponding to atoms of type μ , expressed as percentages, we find $\boldsymbol{\xi} = (\xi_A, \xi_{A'}, \xi_B, \xi_{B'}, \xi_O) = (0.5, 45.7, 1.4, 2.1, 50.3)$ for PbSnTiZrO_6 , $\boldsymbol{\xi} = (0.1, 72.8, 0.2, 0.6, 26.3)$ for KCaZrNbO_6 , and $\boldsymbol{\xi} = (78.5, 0.5, 0.3, 0.6, 20.1)$ for CaBaTiZrO_6 . In all three cases, the ferroelectricity is found to be A-site driven, with very little involvement of B cations. More specifically, it is associated with a displacement of the smaller of the the A-site cations, coupled with some oxygen motion. This seems reasonable in retrospect, since the lattice constant of the overall $AA'BB'O_6$ material will be expanded by the larger A atom, leaving a “rattling cage” environment for the smaller one.

4.4.3 Theoretical modeling

The results of our first-principles calculations of the energies and polarizations of tetrahedral double perovskites can be modeled by expressing the energy as a polynomial in the components of the electric polarization, as in Landau-Devonshire theory. Symmetry considerations exclude certain terms in the expansion, which

is then written as

$$\begin{aligned}
E = & \alpha(P_x^2 + P_y^2 + P_z^2) + \gamma P_x P_y P_z + \\
& \beta(P_x^4 + P_y^4 + P_z^4) + \eta(P_x^2 P_y^2 + P_y^2 P_z^2 + P_z^2 P_x^2) + \\
& \xi P_x P_y P_z (P_x^2 + P_y^2 + P_z^2) + \mathcal{O}(P^6) + \dots
\end{aligned} \tag{4.1}$$

where the energy is measured relative to that of the high-symmetry $F\bar{4}3m$ space group. (Note that the γ and ξ terms would vanish according to cubic symmetry.) We denote the energy and the polarization of the orthorhombic $Imm2$ space group by $E_{\langle 100 \rangle}$ and $P_{\langle 100 \rangle}$ respectively. For the rhombohedral space group $R3m$, we have correspondingly $E_{\langle 111 \rangle}$, $P_{\langle 111 \rangle}$, $E_{\langle \bar{1}\bar{1}\bar{1} \rangle}$ and $P_{\langle \bar{1}\bar{1}\bar{1} \rangle}$. $P_{\langle 111 \rangle}$ and $P_{\langle \bar{1}\bar{1}\bar{1} \rangle}$ represent the positive and negative polarizations of the two minima along the body diagonals. For ordinary ferroelectric materials these polarization values are equal in magnitude, and so are their related energies. In the orthorhombic case we take the z axis to be the symmetry axis, so that $P_x = P_y = 0$ and $P_z = P$. In the rhombohedral case we keep the Cartesian alignment of the axes, such that $P_x = P_y = P_z = P/\sqrt{3}$.

Thus, from our *ab-initio* calculations we have the calculated values of the six quantities $E_{\langle 111 \rangle}$, $E_{\langle \bar{1}\bar{1}\bar{1} \rangle}$, $E_{\langle 100 \rangle}$, $P_{\langle 111 \rangle}$, $P_{\langle \bar{1}\bar{1}\bar{1} \rangle}$, and $P_{\langle 100 \rangle}$ that we can use to determine the free parameters in Eq. (4.1). If we truncate Eq. (4.1) at fifth order as shown, we have six quantities to determine five parameters, thus overconstraining the solution. Similarly, if we truncate Eq. (4.1) at fourth order, we overconstrain more strongly (six constraints and four parameters). Going in the other direction to include sixth order in Eq. (4.1) would be problematic because several invariants appear at sixth order, so that more than six constraints would be needed to determine the system of equations. We therefore attempted the fits with the polynomial truncated at fourth and fifth order. When working at fourth order,

we use all values except $E_{\langle 111 \rangle}$ and $E_{\langle \bar{1}\bar{1}\bar{1} \rangle}$ in the fit, and then test whether we can successfully predict the values of these two quantities. At fifth order, we omit only $E_{\langle \bar{1}\bar{1}\bar{1} \rangle}$, and test this value from the fit.

The comparison of the fitted energies with those computed from the first-principles calculations are presented in Table 4.4. Values that were included in the fit, and are therefore exact by construction, are shown in parentheses. We see that even the fourth-order fit gives encouraging agreement, with a worst-case deviation of about 6%. However, a closer inspection reveals a specific feature of the fourth-order calculation that is qualitatively incorrect, namely that the fitted values of $E_{\langle \bar{1}\bar{1}\bar{1} \rangle}$ are smaller than those of $E_{\langle 111 \rangle}$ for CBTZ and KCZN, while the DFT calculations give the opposite trend. This relates to the fact that these two materials have an anomalous behavior in that the *lower* magnitude of polarization is associated with the *deeper* energy minimum when comparing the $E_{\langle 111 \rangle}$ and $E_{\langle \bar{1}\bar{1}\bar{1} \rangle}$ distortions (PSTZ does not show this anomalous behavior). It turns out that the fourth-order theory does not have enough flexibility to reproduce this behavior; at that level of theory, it can be shown that $|\Delta E_{\langle 111 \rangle}| > |\Delta E_{\langle \bar{1}\bar{1}\bar{1} \rangle}|$ if $|P_{\langle 111 \rangle}| > |P_{\langle \bar{1}\bar{1}\bar{1} \rangle}|$, and vice versa. This discrepancy is removed once we go to the fifth-order theory; as can be seen from Table 4.4, the relative magnitudes of the energies and polarizations are now correct for CBTZ and KCZN, and the discrepancy between the model predictions and *ab-initio* calculations improves substantially. Thus, we conclude that a fifth-order expansion is the minimum complexity needed to give a qualitatively correct description of the energy-polarization relations in the class of AA'BB'O₆ materials under study here. We note, however, that there are still quantitative errors for PSTZ; these can only be removed by going to still higher order, presumably because the larger magnitude of polarization in PSTZ accesses higher terms in the Landau-Devonshire expansion.

4.4.4 Oxygen octahedral rotations

As we have seen in Table 4.3, most of our investigated materials show unstable soft modes corresponding to tilts and rotations of the oxygen octahedra. In our investigation of the ferroelectric states in Sec. 4.4.2, we neglected these modes by relaxing the systems according to symmetry constraints consistent with polar, but not rotational, instabilities. We now consider the effect of these rotations, which may compete with the ferroelectric distortions in determining the ground state of the system.

We use PSTZ as a test case for this purpose. As we saw in Table 4.3, PSTZ shows two unstable sets of modes in the high-symmetry $F\bar{4}3m$ structure, a rotational instability at 182 i cm^{-1} and a polar one at 160 i cm^{-1} . If we follow the polar mode distortion into the polar $R3m\langle\bar{1}\bar{1}\bar{1}\rangle$ structure reported previously in Table 4.4, we find that it is not a local energy minimum. Instead, we find that this structure still has an unstable phonon of frequency 22.7 i cm^{-1} corresponding to rotations of the octahedra about the polar $\langle\bar{1}\bar{1}\bar{1}\rangle$ axis (i.e., like an R -point mode of the ideal 5-atom perovskite structure). Turning on these rotations, the system reaches a stable $R3$ structure at small rotation angles of $\sim 0.46^\circ$ and $\sim 0.79^\circ$ around $\langle\bar{1}\bar{1}\bar{1}\rangle$ for the octahedral rotations centered on B and B' atoms respectively. The phonon mode that was previously unstable is now found to have a positive frequency, while other low-lying mode frequencies and the electric polarization remain almost unchanged. This new phase is energetically approximately equal to the $R3m\langle\bar{1}\bar{1}\bar{1}\rangle$ state. Thus, we find that while the rotations are present in the ground state, they are small and have little influence on the properties of the system.

To check whether this structure is truly the global ground state, we tested what happens if we follow a different route, i.e., starting from the high-symmetry $F\bar{4}3m$ space group and following the path of the unstable octahedral rotation

(mode frequency $182i$ in Table 4.3) without intentionally making any polar distortion. However, because it singles out one of the four $\{111\}$ axes that were previously equivalent, such a rotation immediately converts the system to the *polar* rhombohedral space group $R3$. Relaxation within this space group is then found to lead back to the same structure we found before, in which strong polar distortions predominate over small rotations. Thus, we again conclude that the rotations are unimportant for PSTZ.

While the calculations above are specific to PSTZ, the symmetry analysis is more general and hints at the possibility of obtaining polar samples even if the dominant unstable modes have rotational character. In fact, there is an interesting possibility that even if there are *no* unstable polar modes in the high-symmetry $F\bar{4}3m$ structure, an unstable rotational mode could take the system into a polar space group. This would correspond to the discovery of a new class of improper ferroelectrics, in which the primary order parameter is the antiferrodistortive rotation, but in which a polarization necessarily appears because the selection of a rotation axis in a parent structure without inversion symmetry results in secondary polar distortions along that rotation axis. Moreover, it is interesting that *electric* fields could, at least in principle, be used to control the selection of the *rotational* domains in such a material, at least as far as selecting one of the rotation axes from among the four possible ones.

We already have such cases at our disposal: both KSTN and SCTM have rotational soft modes at the high-symmetry phase, but no polar soft modes. In the case of KSTN, allowing rotation leads to an $R3$ phase which is about 30 meV lower in energy than the high-symmetry structure, and has a polarization of 0.0023 C/m^2 . This value of polarization is indeed tiny, about 1% of that seen in the KCZN case, which has a comparable energy difference between $R3m$ and $F\bar{4}3m$ phases. In the next section we discuss a similar behavior that emerges

from our studies of SCTM.

4.4.5 Magnetic SCTM structures

Recently, Rijnders, Blok and Blank (Rijnders et al. 2010) have succeeded in preparing films of the double perovskite SCTM in rock-salt order using layer-by-layer molecular-beam epitaxy on the (111) surface of LaAlO_3 . To our knowledge, this is the first experimental realization of an $\text{AA}'\text{BB}'$ perovskite system in the double rock-salt arrangement. While their initial characterization of this material does not appear to show a polar character, we were motivated to extend our theoretical calculations to this material in order to make contact with the experiments. We present our results on SCTM in more detail in the present section.

The presence of the magnetic Mn ions makes this material distinct from the others studied so far. Since Sr and Ca are 2+ and Ti is 4+, we find Mn in its 4+ oxidation state. With its d^3 filling in an octahedral environment, this configuration is naturally compatible with a local spin state in which the majority t_{2g} states are filled and other d states are empty. To handle the magnetic nature of the Mn atom, we perform collinear spin-polarized calculations, neglecting the spin-orbit coupling. We consider both ferromagnetic (FM) and antiferromagnetic (AFM) spin arrangements. The Mn atoms reside on an FCC lattice, which is capable of exhibiting several AFM structures, all of which are frustrated to some degree (Phani et al. 1980). We perform calculations on two of the most common AFM variants, the ones of type I and II illustrated in Fig. 4.3(a) and (b) respectively. The spins are aligned ferromagnetically in-plane and antiferromagnetically out-of-plane with respect to (001) planes in the type-I structure, and with respect to (111) planes in the type-II structure.

We first consider the FM spin structure, for which some results were also reported earlier in Tables 4.2-4.3. The resulting material is found to be insulating

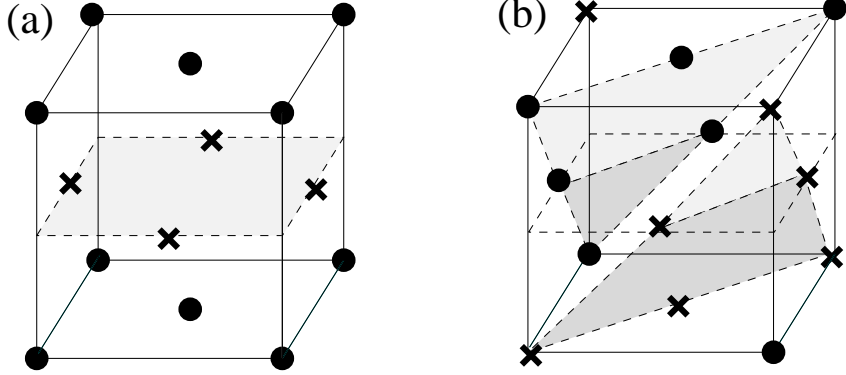


Figure 4.3: (a) Type-I and (b) type-II configuration of SCTM.

Table 4.5: Lattice constants, energy (relative to FM state per 20-atom unit cell) and fraction of parallel nearest-neighbor (NN) and next-nearest-neighbor (NNN) spins for three magnetic structures of SrCaTiMnO_6 .

Structure	Latt. const. (a.u.)	Energy (meV)	NN	NNN
FM	7.15	0	12/12	6/6
AFM (type-I)	7.15	-50	4/12	6/6
AFM (type-II)	7.15	-70	6/12	0/6

with a relaxed lattice constant of 7.15 a.u. in its high-symmetry structure. (It also shows a rotational instability which we have not pursued here.) However, both of the AFM structures considered are lower in energy, as shown in Table 4.5. The AFM arrangement of spins lowers the symmetry from $F\bar{4}3m$ to tetragonal $P\bar{4}m2$ and rhombohedral $R\bar{3}m$ space groups for type I and II ordering, respectively. After relaxation, the new lattice constants still closely resemble that of the high-symmetry structure (e.g., the c/a for the $p\bar{4}m2$ case is 0.9996). It is primarily the motion of the ions off the high-symmetry positions, brought about by the specific spin configurations, that defines the new space groups. Both these AFM cases are found to be insulators, with the type-II arrangement being slightly lower in energy. Table 4.5 also provides a concise summary of the number of parallel nearest-neighbor and next-nearest-neighbor spins out of all such neighbors.

Next, we find the phonon frequencies at the Γ point of this relaxed type-II AFM cell. There is one set of three soft modes, but the eigenmode analysis reveals them to be oxygen zone-boundary phonons, ruling out the possibility of a polar instability. This seems to be consistent with the experimental characterization of Rijnders et al. (2010). However, instead of stopping here, we take the analysis a bit further, following the spirit of the last section on zone-boundary rotation of oxygen octahedra. Following the unstable mode in the $R3m$ phase, we arrive at the polar $R3$ space group, and find it to be lower than the $R3m$ phase by 319 meV (per 20-atom unit cell). As pointed out before, the $R3$ phase is a polar phase and exhibits an improper polarization induced by rotation of the oxygen octahedra. The calculated polarization is found to be very small, about 0.01 C/m², and points along the $\langle 111 \rangle$ direction. A phonon analysis in this phase reveals that two modes still remain soft, indicating that the ground state of the system has not yet been reached. We expect that further relaxation along these soft modes would lead to a lower-symmetry structure with additional octahedral rotations, but still with a very small polarization.

While it lies beyond the scope of the present investigation, we note that it may also be of interest to consider the effects of epitaxial strain on the SCTM system. This could provide more direct contact with the experimental work on epitaxial growth mentioned earlier, as well as possibly making contact with recent work (Lee & Rabe 2010) showing that SrMnO₃, which is one of the parent perovskites of SCTM, can be driven between FM/FE and AFM/PE states via application of epitaxial strain. These considerations are left for future investigations.

4.5 Summary

In summary, we have carried out a first-principles study of the properties of prospective $AA'BB'O_6$ perovskites having double rock-salt order. We find several candidate compounds that are predicted to have ferroelectric instabilities associated with A-site displacements, with PSTZ (PbSnTiZrO_6) being of special interest because of its large spontaneous polarization and peculiar energy landscape having four global minima along $\langle \bar{1}\bar{1}\bar{1} \rangle$ directions and four secondary local minima along $\langle 111 \rangle$ directions. Compounds in this class may also be capable of exhibiting improper ferroelectricity based on rotation of oxygen octahedra, again stemming from the lack of inversion symmetry in the high-symmetry space group. We also predict that epitaxial strain can, under appropriate conditions, induce a polarization in an otherwise paraelectric material of this class. The inclusion of magnetic cations may provide interesting opportunities for the realization of novel magnetoelectric or multiferroic materials.

While initial attempts at the synthesis of such materials have not yet resulted in the demonstration of ferroelectricity, they do provide an existence proof that such synthesis is possible. We hope that the crossing of this hurdle will stimulate attempts at synthesis by other groups, and that eventual success will lead to novel ferroelectric materials having interesting and potentially useful physical properties.

Chapter 5

Half-Heusler semiconductors as piezoelectrics

5.1 Introduction

In the last two chapters we discussed electromechanical properties such as strain response, piezoelectricity and polarization in the context of perovskite oxides, not all of which have been synthesized yet. In this chapter we stick to the theme of studying electromechanical properties *ab initio*, but focus on a different class of compounds, called *half-Heusler* compounds. They have a simple unit cell like the perovskites, although consisting of three atoms, say A , B and C . The ABC half-Heusler compound has a structure like $MgAgAs$, and they are also known as semi-Heusler or Juza-Nowotny compounds (Nowotny & Bachmayer 1950) in the literature. They form a large and varied family, with over 150 distinct ABC half-Heusler compounds reported in the *Inorganic Crystal Structural Database* (ICSD) (Belsky et al. 2002). They exhibit many properties, another similarity with perovskite compounds, although a lot more work remains to be done in this class of materials compared to perovskites.

The half-Heusler structure, shown in Fig. 5.1, belongs to $F\bar{4}3m$ space group and has tetrahedral point symmetry. It can be thought of as a rocksalt lattice formed from two of the three atoms constituting ABC (say, at Wyckoff positions 4a and 4b), while the third atom sits at the tetrahedral interstitial sites (either Wyckoff position 4c or 4d). We are going to discuss their structure and related structures in more detail in the next section. For example, we can visualize

the half-Heusler structure by removing one of the A sublattices from the A_2BC Heusler structure, or by stuffing the interstitial sites of the AC or BC zincblende structure (Kandpal et al. 2006) with another atom.

A German mining engineer and chemist Friedrich Heusler first studied Cu_2MnSn (this class of compounds later being named after him), which showed ferromagnetism (Heusler et al. 1903). Though none of its constituent atoms is ferromagnetic, the alloy shows ferromagnetism through a many-body interaction called the double-exchange mechanism (Zener 1951; de Gennes 1960). A long period of relative inactivity followed after the initial phase of discoveries, but the last few decades have seen a surge of interest initiated by the observation of half-metallic ferromagnetic behavior in half-Heusler compounds (deGroot et al. 1983), which led to more efforts to explore these compounds. Half-Heusler and Heusler compounds can show topological properties (Chadov et al. 2010; Lin et al. 2010), and have potential uses in various applications, such as spintronic-device components (Felser et al. 2007) and high-performance thermoelectrics (Shen et al. 2001; Nolas et al. 2006; Balke et al. 2011) to name a few exotic ones. The wide range of lattice constants and band gaps and the variety of constituent atoms, make the half-Heusler family one of the most versatile class of compounds, thus enabling one to extend the range of its functionality.

Many half-Heusler compounds are metallic, but the growing number of semi-conducting half-Heusler compounds are very important in their own right. Li-containing half-Heusler compounds were predicted to have band gaps on the order of 1 eV according to first-principles calculations performed by Wood et al. (1985). LiMgX and LiZnX (where $X=\text{N, P}$ and As), LiMgSb , and the cell-doubled compounds Li_3AlN_2 , Li_3GaN_2 , and Li_3GaP_2 are some of the most-studied half-Heusler semiconductors. A combination of experimental observations and first-principles investigations (Aliev et al. 1987; Ogut & Rabe 1995) revealed NiSnZr to be a

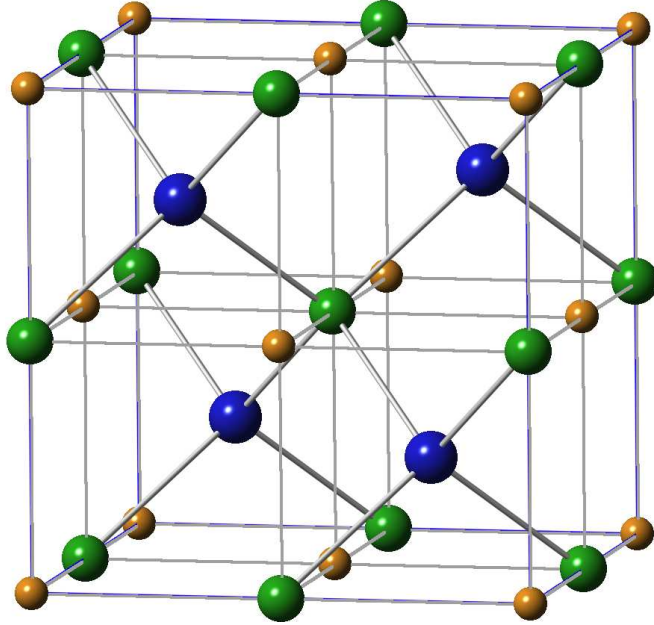


Figure 5.1: The ABC half-Heusler structure type: A (green) and B (orange) are arranged in a rocksalt lattice, with the tetrahedral coordination of C (blue) by A shown.

semiconducting half-Heusler compound, which led to many additional semiconducting systems being identified (Kandpal et al. 2006; Kieven et al. 2010; Gruhn 2010). The ones with bigger gaps, such as LiMgN and LiMgP , may be suitable for solar cell applications (Casper et al. 2009; Kuriyama et al. 2002, 1998).

Insulating half-Heuslers theoretically should have functional properties related to electric polarization, but these properties have not received enough attention. For example, the $F\bar{4}3m$ space group of the half-Heusler structure implies a nonzero d_{14} piezoelectric response, but no measurement of piezoelectricity in these systems has yet been reported to our knowledge. In the current chapter we present our efforts to understand piezoelectricity for this class of compounds using first-principles calculations.

5.2 Structure of half-Heusler and related compounds

We briefly discussed the structure of half-Heusler compounds in the last section, and related it to a stuffed zincblende structure, or a hollowed-out full-Heusler structure (where half the tetrahedrally bonded atoms are missing). In this section we develop this connection in more detail, closely following the discussion in Graf et al. (2009). Here we go beyond the half-Heusler structure and find its connection to other related structures and symmetries. Often these structures are related to one another by substitution of an atom and characterized by the degree of disorder. This is important for real-life synthesis of these systems, as the properties we see can vary greatly depending on the structure. For example, we will see that the ordinarily full-Heusler structure with a chemical formula A_2BC has octahedral point symmetry, where A atoms occupy tetrahedral positions. If we interchange half the A atoms with either B or C atoms, the symmetry is reduced and the new compound belongs to a tetrahedral point group. The first compound has inversion symmetry, and shows no piezoelectric effect, while the tetrahedral point group lacks inversion symmetry and can show a piezoelectric effect.

We schematically represent the half-Heusler structure in Fig. 5.2b, and compare it with the zincblende structure shown in Fig. 5.2a. Both these structures belong to the $F\bar{4}3m$ space group and have tetrahedral point symmetry. At this point we introduce the convention that we follow to identify the arrangement of atoms in these structures. There are two rock-salt sublattices in all of them, each of which could be fully occupied, or half occupied (by the same or different atoms). We will underline the atom(s) forming one of the two sublattices, while the remaining atoms are understood to constitute the other rocksalt sublattice. By this definition, Fig. 5.2a has a structure given by $\underline{A}B$ (although it could have

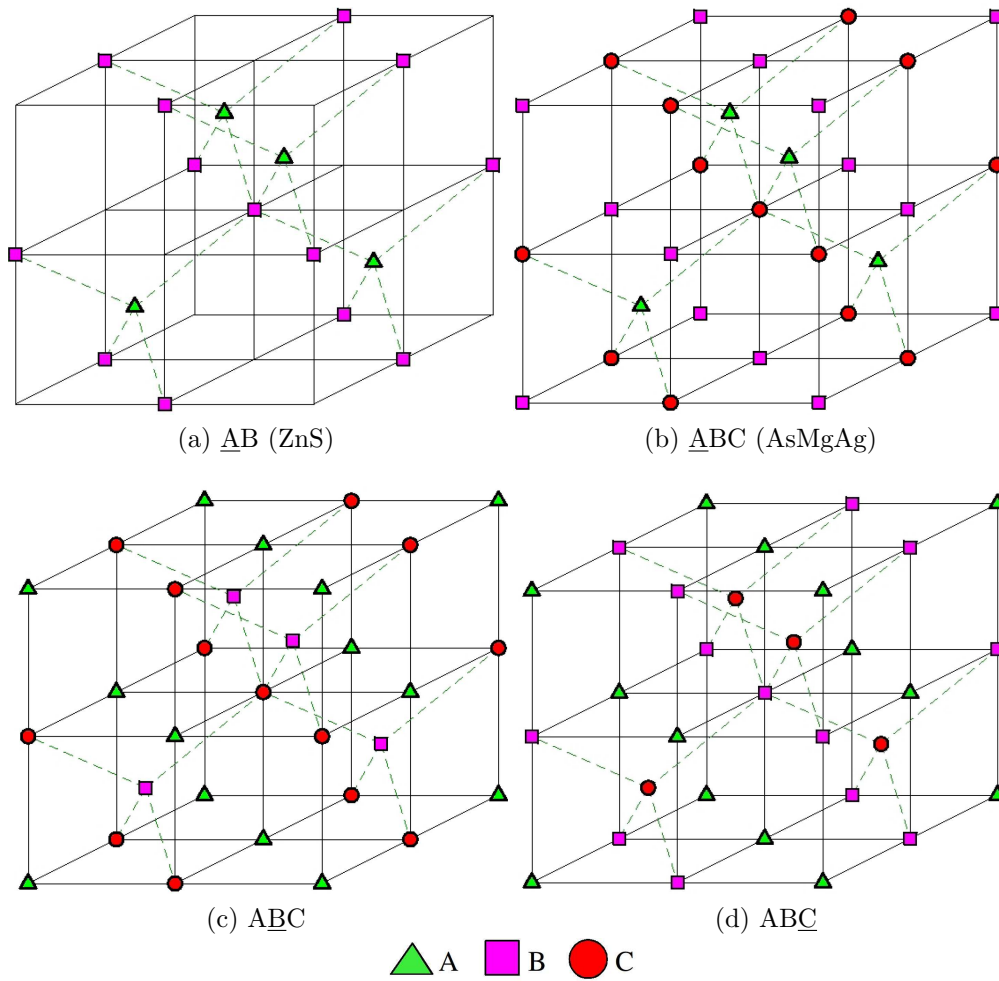


Figure 5.2: Green triangles denote species A, magenta squares B, and red circles C in this and subsequent figures in this section. (a) Zincblende structure and (b)-(d) three configurations of the half-Heusler structure. Compared to ZnS, there are extra red circles forming a rocksalt sublattice with magenta squares to stuff the zincblende structure into a half-Heusler structure. All belong to space group $F43m$. For underline notation, see text.

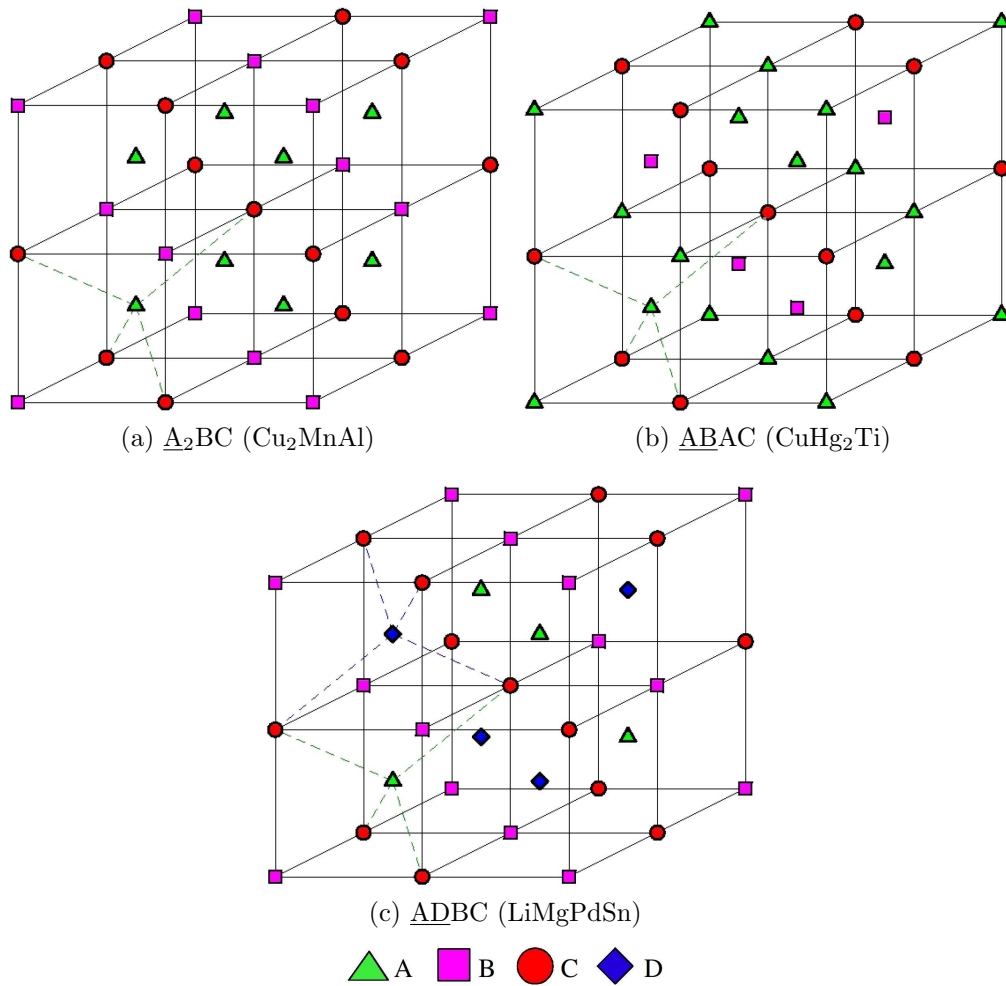


Figure 5.3: Two structures with the chemical formula of full-Heusler compounds: (a) $Fm\bar{3}m$ symmetry and (b) $F\bar{4}3m$ symmetry. (c) Mixed-Heusler structure with $F\bar{4}3m$ symmetry.

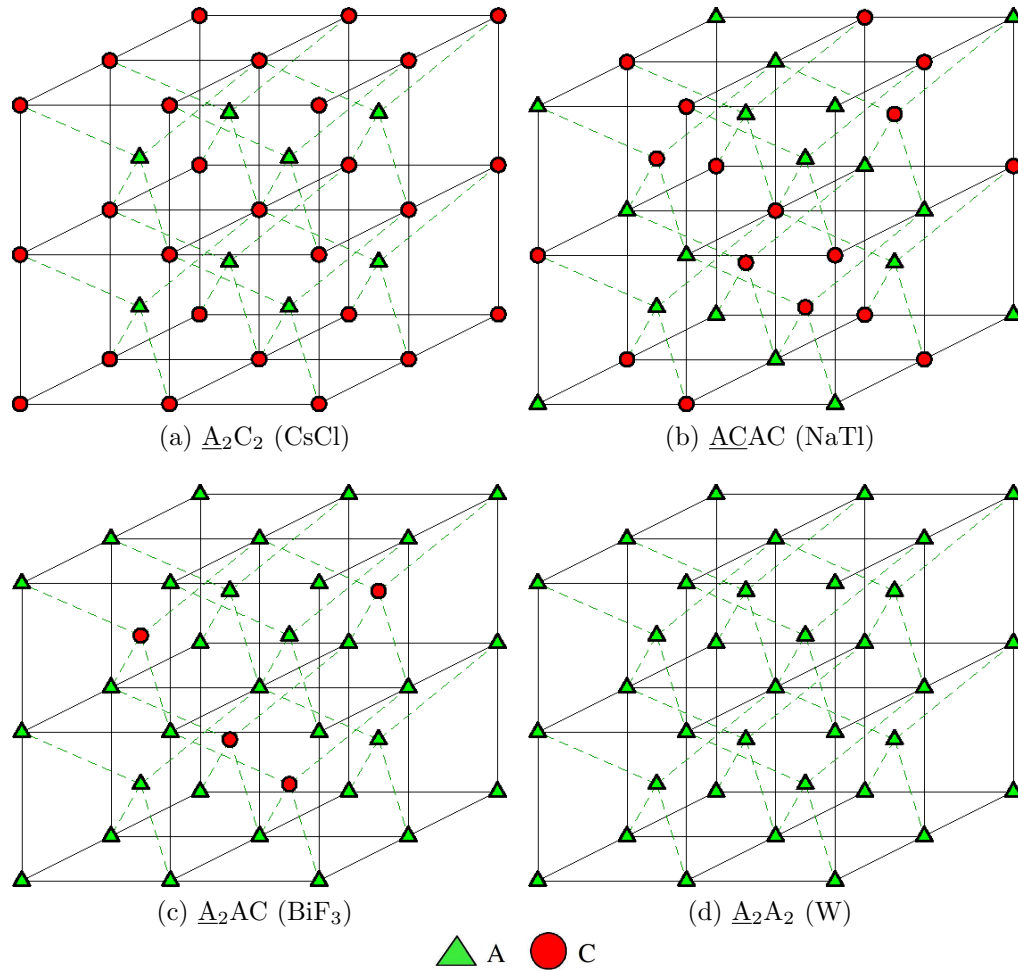


Figure 5.4: Other variants of the same structure type. (a) Space group $Pm\bar{3}m$ (b) Space group $Fd\bar{3}m$ (c) Space group $Fm\bar{3}m$ and (d) Space group $Im\bar{3}m$

been written \underline{AB}), and the structure in Fig. 5.2b is \underline{ABC} (although it also could have been written \underline{ABC} , following our notations in this section, green triangles representing species A, magenta squares B, and red circles C.) We see that in Fig. 5.2b there is a remaining tetrahedral site lying vacant, which we can fill up in two unique ways. If the filling atoms are the same species as the other tetrahedral site (A in this figure), forming a rocksalt sublattice composed of green triangles as in Fig. 5.3a, we get the conventional full-Heusler structure $\underline{A_2BC}$. This has octahedral symmetry and belongs to space group $Fm\bar{3}m$. On the other hand we could introduce a new atom D (blue rhombus) to fill up this void, in which case we will have a structure \underline{ADBC} as shown in Fig. 5.3c. Here we lose the octahedral point symmetry of the previous case, and this structure belongs to the $F\bar{4}3m$ space group again. We loosely call this *mixed-Heusler* structure, or MH. A prototype of this structure is LiMgPdSn. However, there is another variant to the chemical formula A_2BC , as mentioned in the beginning of this section. Instead of having the structure $\underline{A_2BC}$, it could arrange itself as \underline{ABAC} , as in Fig. 5.3b. This structure belongs to the $F\bar{4}3m$ space group, unlike its twin from the $Fm\bar{3}m$ space group.

This could be a good point to stop our discussion on various Heusler structures, but it is too tempting to carry on further and explore a few more related structures. In Fig. 5.3c, if we make A, B and D all same, say A, we have a structure $\underline{A_2AC}$ with chemical formula A_3C , with BiF_3 being a prototype of this compound belonging to the $Fm\bar{3}m$ space group. On the other hand, starting from the zincblende structure \underline{AC} , we have two more possibilities leading to interesting cases: $\underline{A_2C_2}$ (Fig. 5.4a), and \underline{ACAC} (Fig. 5.4b), both having chemical formula A_2C_2 (actually, AC). In the first case each rock-salt sublattice is full and is composed of the same species. In the second case two indistinguishable rock-salt sublattices are interpenetrating. $\underline{A_2C_2}$, with a prototype CsCl, belongs to

Table 5.1: Structure and prototypes for Half-Heusler compounds and other related compounds. Here A and D form one rocksalt sublattice, while B and C form the other rocksalt sublattice. If any site is vacant, we represent that as [X], meaning the position of X is empty.

Site occupancy	General formula	Structure prototype	Space group
A,[D],B,[C]	AB	ZnS	$F\bar{4}3m$
A,[D],B,C	ABC	AsMgAg	$F\bar{4}3m$
A,D,B,C	ADBC	LiMgPdSn	$F\bar{4}3m$
A=D,B,C	A ₂ BC	Cu ₂ MnAl	$Fm\bar{3}m$
A,D=B,C	AB ₂ C	CuHg ₂ Ti	$F\bar{4}3m$
A=D=B,C	A ₃ C	BiF ₃	$Fm\bar{3}m$
A=D,B=C	A ₂ B ₂	CsCl	$Pm\bar{3}m$
A=B,D=C	A ₂ D ₂	NaTl	$Fd\bar{3}m$
A=B=C=D	A ₄	W	$Im\bar{3}m$

the $Pm\bar{3}m$ space group, while \underline{ACAC} (prototype: NaTl) has higher symmetry and belongs to the $Fd\bar{3}m$ space group. Finally, we obtain the topmost structure with highest symmetry in this series when both A and C are the same (say, A), and all sites are filled up as in Fig. 5.4d. This is just the BCC structure, i.e., the structure of tungsten (W), and it belongs to space group $Im\bar{3}m$. We summarize this information in Table 5.1.

Even within a structure one can often expect variations. The half-Heusler structure given by \underline{ABC} has the A atom in the Wyckoff position $4c$, with $4d$ being empty, or vice versa. But atoms A, B and C could be shuffled around, giving rise to alternative configurations \underline{ABC} and \underline{ABC} , as depicted in Fig. 5.2d and Fig. 5.2c respectively. All these configurations belong to the same space group, but they have different total energy and chemical environment. In the following sections we will see how this affects our calculations.

Lastly, here we have mostly discussed a lot about compounds belonging to the

$F\bar{4}3m$ space group, the same high-symmetry class discussed in the last chapter involving $AA'BB'O_6$ perovskite, which gave rise to asymmetric energy-polarization behavior on lowering of the symmetry. Being in this space group has led, theoretically, some of those double perovskite to polarization. But that is not possible here, since ferroelectricity in the present context would mean breaking existing bonds and forming new bonds again, a rather difficult process.

5.3 Computational details

We perform a series of first-principles calculations to find the piezoelectric response and associated properties of half-Heusler compounds. These predictions are first presented for the whole set of combinations we study, followed by an identification of those reported in the ICSD as having half-Heusler structure. Next, we look into combinations predicted to be high-performance, though not reported to exist yet. Through targeted synthesis, including compositional substitution, epitaxial growth or artificial structuring, half-Heusler compounds could be developed as a valuable class of piezoelectric materials.

The ABINIT package (Gonze et al. 2002, 2005, 2009) is used to perform all the first-principles calculations with the local-density approximation (LDA) exchange-correlation functional. The FCC Brillouin zone is sampled with an $8 \times 8 \times 8$ shifted Monkhorst-Pack mesh (Monkhorst & Pack 1976). Troullier-Martins norm-conserving pseudopotentials are employed, with a plane-wave cutoff of 30 Ha. The value of plane-wave cutoff and the k -space mesh size were chosen after careful convergence studies, convergence criteria often being different for different combinations. The above specifications are found to be good for all combinations studied in this chapter.

For the high-throughput search, we consider combinations of three distinct

elements ABC . For each combination, we optimize the lattice constant for each of the three structural variants \underline{ABC} , \underline{ACB} , and \underline{CBA} as shown in Fig. 5.2b-d. Piezoelectrics are insulating, and hence our successful candidates will have to have a band gap. If we blindly take three atoms to form a combination from the total pool of atoms we have (37 of them discussed later in this paragraph), we end up with $37!/(3!34!) = 15540$ possibilities, which is beyond our computational capabilities. However, a more focused search to limit combinations to those with a total of 8 s and p valence electrons yield good results, since we expect this to improve the likelihood of band gap formation (Kandpal et al. 2006). We also require that there be at least one and at most two p -block elements among the three constituents, with the remainder coming from the s and/or d blocks of the periodic table. We use Roman numerals to denote the valences of the constituent elements (including d electrons) to classify the combinations into families with 8 valence electrons (I-I-VI, I-II-V, I-III-IV, II-II-IV, and II-III-III), 18 valence electrons (XI-I-VI, XI-II-V, XI-III-IV, I-XII-V, II-XII-IV, III-XII-III, X-II-VI, X-III-V, and X-IV-IV), or 28 valence electrons (X-XII-VI, XI-XI-VI, XI-XII-V and XII-XII-IV). We consider the following atoms based in part on the availability of good pseudopotentials: I=(Li, Na), II=(Be, Mg, Ca, Sr, Ba), III=(B, Sc, Y, Al, Ga), IV=(C, Si, Ge, Sn, Pb, Ti, Zr, Hf), V=(N, P, As, Sb, Bi), VI=(O, S, Se, Te), X=(Ni, Pd, Pt), XI=(Cu, Ag, Au), and XII=(Zn, Cd). With all these restrictions, we still obtain a long list of 792 candidate combinations to be searched. As a test, we did perform calculation for over 150 cases violating the 8 s and p valence electron rule, and found all of them to be metals.

The band structures are plotted for all the compounds, and the nonmetals are selected for further study. Electronic dielectric constants ϵ_∞ are determined for all the nonmetals. We compute the phonon frequencies and eigenvectors at the zone-center Γ point, along with three additional high-symmetry points ($X =$

$(1/2, 0, 1/2)$, $L = (1/2, 1/2, 1/2)$ and $W = (1/2, 1/4, 3/4)$, defined in reduced coordinates). Any combination exhibiting instability at these points is eliminated.

Linear-response calculations DFPT (Gonze & Lee 1997), as implemented in ABINIT, are carried out to compute Born effective charges, piezoelectric d and e tensors, elastic tensors C and compliance tensors S (Wu et al. 2005; Hamann et al. 2005). The post-processing package ANADDB is used to extract all the numbers from the ABINIT output files. We also use the C_{11} and C_{12} elastic constants, along with C_{44} , to check local elastic stability. The elastic constants for stable compounds should satisfy $C_{11} + 2C_{12} > 0$, $C_{44} > 0$ and $C_{11} - C_{12} > 0$, as described in Karki et al. (1997) and references therein. The electromechanical coupling factor (k_{14} for the class of piezoelectrics we are interested in) is a quantity of central importance in our study. The quantities determined above are sufficient to find k_{14} , which is given by

$$k_{14} = |d_{14}| \sqrt{\frac{C_{44}}{\epsilon_{\text{fs}} \epsilon_0}}, \quad (5.1)$$

as described in Wu et al. (2005), where ϵ_{fs} is the permittivity of free space and ϵ_0 is dimensionless free-stress static dielectric constant. ϵ_0 can be obtained from the free-strain static dielectric constant following Wu et al. (2005):

$$\begin{aligned} (\epsilon_0)_{\alpha\beta} &= \delta_{\alpha\beta} + \chi_{\alpha\beta}, \\ (\epsilon_0)_{\alpha\beta}^{(\eta)} &= \delta_{\alpha\beta} + \chi_{\alpha\beta}^{(\eta)}, \\ \chi_{\alpha\beta} &= \chi_{\alpha\beta}^{(\eta)} + \frac{1}{\epsilon_{\text{fs}}} e_{\alpha j} (C^{-1})_{jk} e_{\beta k}, \end{aligned} \quad (5.2)$$

where quantities (ϵ_0, χ) with superscript η correspond to those obtained under fixed-strain condition (which standard calculations yield), and those without are

the free-stress versions. The static dielectric constant (both free-stress and free-strain) can be obtained from the respective electronic dielectric constant $(\epsilon_\infty)_{\alpha\beta}$ using

$$(\epsilon_0)_{\alpha\beta} = (\epsilon_\infty)_{\alpha\beta} + \sum_{\omega_\mu^2 \neq 0} \frac{\bar{Z}_{\mu\alpha}^* \bar{Z}_{\mu\beta}^*}{\Omega \epsilon_{\text{fs}} \omega_\mu^2}, \quad (5.3)$$

as explained in Born & Huang (1954) (in different units), where $\bar{Z}_{\mu\alpha}^*$ are the mode-effective charges for the mode μ along direction α , Ω is the volume of the unit cell and ω_μ are the phonon frequency at the Γ point for the mode μ .

One main challenge of this work is efficient bookkeeping. Here we managed to create input files, handle output files, and extract numbers to be used in subsequent calculations with the help of *Python* computer language.¹ Interspersed with multiple random checks at various points, this method ensures efficiency while avoiding human errors.

5.4 Results

We start with the properties of all the 792 *ABC* combinations shortlisted earlier for study. For each combination the lattice constant is optimized for all three configurations: \underline{ABC} , \underline{ACB} , and \underline{CBA} . We perform band-structure calculation with the energetically most stable variant (lowest total energy) to check whether our LDA calculations give a nonzero band gap. We find 234 insulators out of the 792 combinations, and all of them have either 8 or 18 valence electrons. All the compounds containing 28 valence electrons are metallic. For the insulators, we calculate phonon frequencies and eigenmodes at four high-symmetry points (Γ , X , L and W). We perform linear-response calculations using ABINIT as described

¹<http://www.python.org/>

in the previous section. This enables us to determine structural instability or elastic instability from the soft modes, or the elastic constants. Thus the number of stable combinations is brought down to 189 from 234 insulators.

We attempt to represent this result visually. A quick look at the list of these 234 nonmetallic candidates (presented in Table A.1 in the Appendix A) tells us that the overwhelming majority of the combinations have the most electronegative atom occupying the Wyckoff $4c$ or $4d$ site, bonding tetrahedrally with the other more electropositive elements. More often than not, the most electronegative element also happens to be the smallest of the three constituents. We are curious to see how these factors play out for the two higher-energy configurations. Which factor wins for cases when the most electronegative element is not the smallest one?

To understand this we define two quantities, ΔZ^* and ΔR , to capture the effect of charge and size of the constituents. For a combination ABC , we define the deviation in electronegativity (a dimensionless quantity) for the tetrahedrally coordinated species (C in this case) as $\Delta\chi = \chi_C - (\chi_A + \chi_B + \chi_C)/3$. Similarly we define $\Delta R = R_C - (R_A + R_B + R_C)/3$. Here we use the Zunger pseudopotential radii (Zunger 1980) for R_X . R_X is the sum of the r_s and r_p radii of atom X, which are the effective size of the quantum cores of s and p symmetry. This total is a good measure of radius of an element in a compound and widely used in electronic-structure community to understand material properties. They also show reasonable transferability, meaning that the same radius of an element can be used when it bonds with different elements to form different compounds. We must mention a small detail here. Generally, the electronegativity of an element depends on the nature of the chemical environment surrounding it, but it shows enough transferability to be used for this purpose.

Fig. 5.5 plots these two quantities for the lowest-energy configuration (red

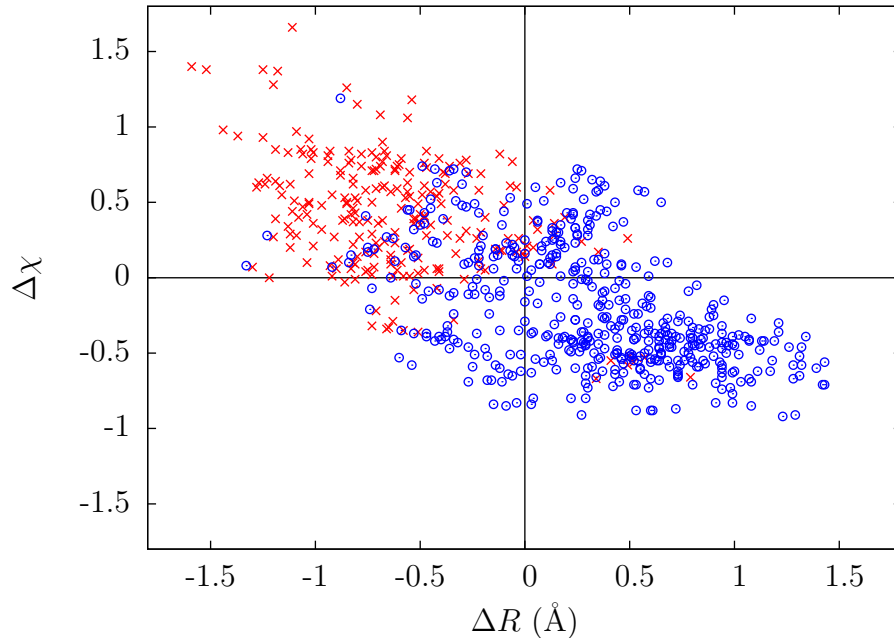


Figure 5.5: Deviation of electronegativity and pseudopotential radius of the tetrahedrally coordinated species of lowest-energy configurations (red crosses) and the two higher-energy configurations (blue circles) for all nonmetallic cases.

crosses) in contrast with the two higher-energy configurations (blue circles) for each nonmetallic combination. We see that the overwhelming majority of lowest-energy configurations have the most electronegative element sitting at the tetrahedral location. They also happen to be smallest in size in most cases. In a similar vein, we go ahead and plot the same two quantities for all 792 combinations in Fig. 5.6, insulators with red crosses and metals with blue circles. While insulators show a strong trend of placing their most electronegative atom in the tetrahedrally coordinated position, metals show no such definite trend.

Since DFT tends to underestimate band gaps, the actual number of nonmetallic combinations will perhaps be somewhat larger than what we have. But this list of 189 combinations are insulating and locally stable in their lowest-energy configurations (of the three possible ABC half-Heusler structures) according to our calculations. The computed band gaps and the lattice constants are shown

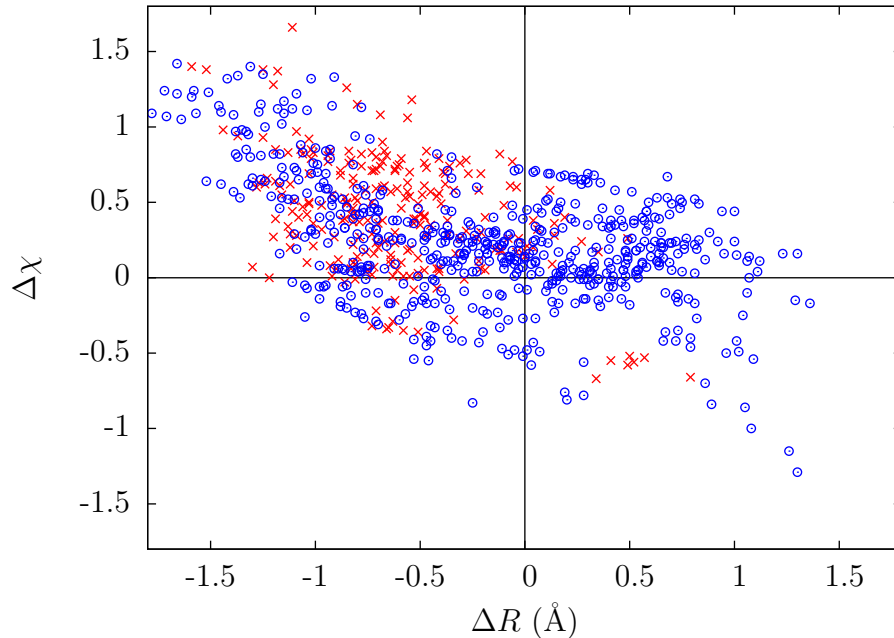


Figure 5.6: Deviation of electronegativity and pseudopotential radius of the tetrahedrally coordinated species for the lowest-energy configurations of insulators (red crosses) and metals (blue circles). All 792 combinations are plotted.

for these 189 compounds in Fig. 5.7. There is no particular correlation between lattice parameter and band gap, and we did not expect any. Both quantities are spread broadly with a few quite far from the cluster formed by the majority. This is good news from the perspective of material design, since a broad array of band gaps and cell constants offers flexibility in selecting the material with the desired gap or lattice constant. For example, a specific optoelectronic application may require placing the compound on a particular substrate, and having materials with very different lattice constants to choose from increases the possibility of coming up with useful composites.

Other quantities like d_{14} , k_{14} , and ϵ_0 are found, either directly from ABINIT, or using the formulas given before. We present a plot of k_{14} vs. $\log d_{14}$ in Fig. 5.8 to show how these quantities in the set of known and hypothetical half-Heusler compounds compare with that of the subset of known compounds,

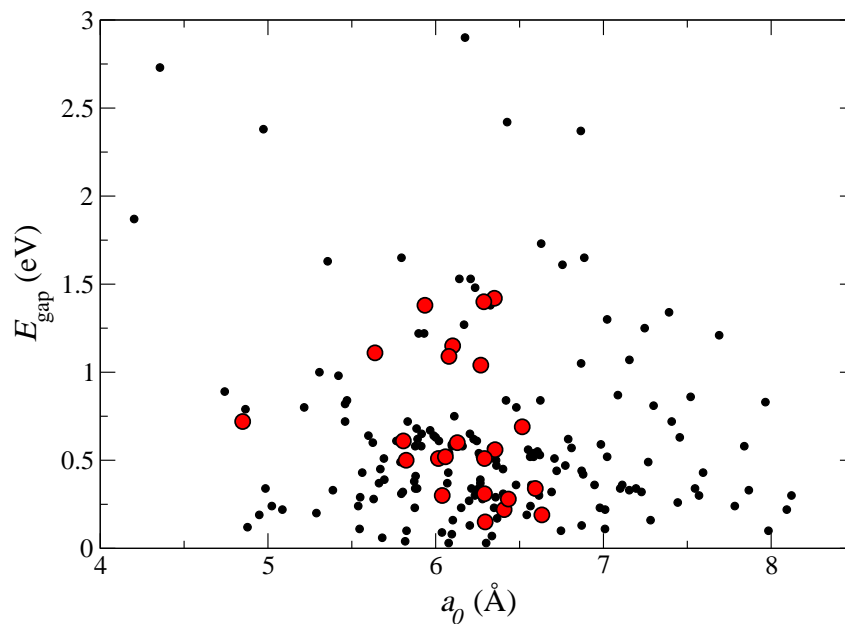


Figure 5.7: Cell parameters (in Å) of insulating ABC combinations as well as their range of band gaps (in eV) are depicted as open black circles. Known combinations, from Table 5.2, are highlighted as filled red circles.

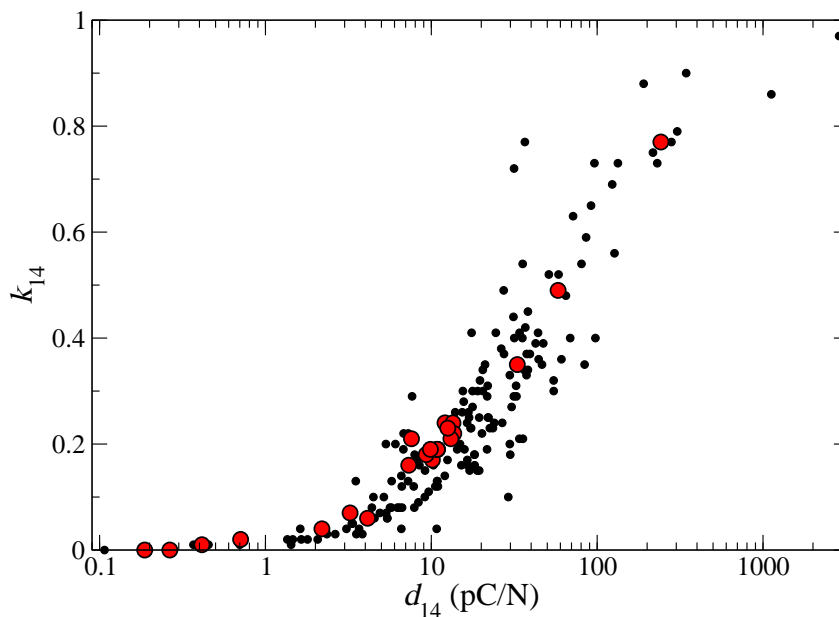


Figure 5.8: Electromechanical coupling factor k_{14} of insulating ABC combinations as a function of piezoelectric constant d_{14} . Known combinations, from Table 5.2, are highlighted as filled red circles

We see that there are 36 combinations in our search set of 792 that have been reported in the ICSD as experimentally obtained structures. We go through the usual procedure for each of them to identify the energetically most stable of the three structures and find that 23 of them, listed in Table 5.2, are insulating according to first-principles calculations.² The lowest-energy configurations as determined by our calculations are indicated in the first column. For five compounds (LiZnAs, AuScSn, NiScSb, PdScSb and PtYSb) refined structures, including R value and temperature factors, are available in ICSD. For all of them our predictions agree with the experimentally observed structure. Most of the computed lattice constants given in Table 5.2 are in very good match with experiments. The lowest computed gap is 0.15 eV for NiScBi to highest at 1.42 eV for PtZrSn. The piezoelectric constants d_{14} , according to this calculation, fall in the range from 2.0 to 14 pC/N. All except five compounds have $d_{14} > 2.6$ pC/N, the experimentally measured d_{14} value of GaAs. NiYSb, PdYSb and PtYSb show the highest values here, which can be attributed to their small bandgap, large ϵ_0 and low elastic constant. Not surprisingly, these three compounds also have the highest values of electromechanical coupling k_{14} , as given in Table 5.2, arising from their large d_{14} and low elastic constant, though limited by relatively big ϵ_0 .

Looking at Fig. 5.8, it can be seen that there are hypothetical compounds with k_{14} and d_{14} values well above those of known compounds (including some with k_{14} close to one and d_{14} up to several hundred). These two quantities show the expected positive correlation, since they are related via Eq. (5.1). We list the twelve compounds with the highest d_{14} values in Table 5.3. As both the polarization-strain response e_{14} and the shear elastic constant C_{44} contribute towards k_{14} , one can end up with a large value either from a high e_{14} , a small C_{44} ,

²The thirteen metallic combinations are LiAlSi, LiGaSi, LiAlGe, BeAlB, CuMgSb, AgMgAs, CuMgBi, AuCaBi, NiYBi, CuCdSb, AgCdSb, AuCdSb, and AuYPb.

Table 5.2: Properties of experimentally synthesized half-Heuslers, grouped by family. Experimental lattice constants are from the ICSD. Also presented are the theoretical lattice constant a , band gap E_{gap} , piezoelectric coefficient d_{14} , electromechanical coupling coefficient k_{14} , and free-stress static dielectric constant ϵ_0 .

ABC	$a_{\text{expt.}}$ (Å)	a (Å)	E_{gap} (eV)	d_{14} (pC/N)	C_{44} (10^{11} Pa)	k_{14}	ϵ_0
<u>LiMgP</u>	6.02	5.94	1.38	3.2	0.46	0.07	11.33
<u>LiMgAs</u>	6.19	6.10	1.15	2.2	0.41	0.04	12.61
<u>LiMgBi</u>	6.74	6.52	0.69	0.3	0.31	0.00	15.76
<u>LiZnN</u>	4.87	4.85	0.72	7.6	0.82	0.18	15.39
<u>LiZnP</u>	5.78	5.64	1.11	12.1	0.57	0.24	15.92
<u>LiZnAs</u>	5.94	5.81	0.61	13.5	0.58	0.24	20.08
<u>LiCdP</u>	6.09	6.02	0.51	0.4	0.44	0.01	19.18
<u>AuScSn</u>	6.42	6.41	0.22	10.2	0.56	0.17	22.57
<u>NiTiSn</u>	5.94	5.82	0.50	0.2	0.90	0.00	29.04
<u>NiZrSn</u>	6.11	6.13	0.60	13.7	0.67	0.22	28.38
<u>NiHfSn</u>	6.08	6.06	0.52	10.9	0.79	0.19	28.38
<u>PdZrSn</u>	6.32	6.35	0.56	13.1	0.61	0.21	25.02
<u>PdHfSn</u>	6.30	6.29	0.51	10.8	0.71	0.19	24.71
<u>PtTiSn</u>	6.16	6.08	1.09	0.7	0.94	0.02	21.92
<u>PtZrSn</u>	6.32	6.35	1.42	9.3	0.74	0.19	20.00
<u>PtHfSn</u>	6.31	6.29	1.40	7.3	0.85	0.16	19.28
<u>NiScSb</u>	6.06	6.04	0.30	12.6	0.70	0.23	22.96
<u>NiScBi</u>	6.19	6.30	0.15	4.1	0.57	0.06	27.99
<u>NiYSb</u>	6.31	6.43	0.28	242.3	0.05	0.77	23.30
<u>PdScSb</u>	6.31	6.29	0.31	10.9	0.59	0.19	21.12
<u>PdYSb</u>	6.53	6.63	0.19	33.0	0.25	0.35	21.81
<u>PtScSb</u>	6.31	6.27	1.04	9.9	0.72	0.19	20.31
<u>PtYSb</u>	6.54	6.59	0.34	58.2	0.21	0.50	24.50

Table 5.3: Top twelve half-Heusler compounds, ranked according to piezoelectric coefficient d_{14} .

ABC	a (Å)	E_{gap} (eV)	d_{14} (pC/N)	C_{44} (10^{11} Pa)	k_{14}	ϵ_0
SrCdSi	7.01	0.11	2878.8	0.01	0.97	24.98
SrAlGa	6.87	0.13	1122.3	0.01	0.86	48.85
NaZnP	6.07	0.37	344.1	0.06	0.90	17.79
NaBGe	5.56	0.43	304.2	0.03	0.79	18.12
MgSrSi	7.09	0.87	280.4	0.04	0.80	20.63
NiYSb	6.43	0.28	242.3	0.05	0.77	23.30
MgSrGe	7.11	0.36	230.4	0.05	0.75	21.95
CuYSi	6.36	0.50	217.0	0.05	0.76	19.87
NaMgN	5.46	0.72	190.6	0.09	0.87	11.33
BeScB	5.39	0.33	133.4	0.13	0.72	23.84
MgSrSn	7.41	0.72	127.2	0.07	0.58	25.56
LiCaP	6.63	1.73	123.2	0.07	0.72	10.82

or both. This manifests in Table 5.3, where C_{44} are small for all the examples.

For experimental synthesis often there are considerations overlooked in purely theoretical studies. Here we try to pay attention to a few factors which would probably be relevant for synthesis. We screen our list to exclude compounds with toxic (Pb, Cd, As) or expensive (Be, Pd, Pt) elements. In addition, we require a DFT band gap above 0.4 eV to limit leakage current through the sample. To encourage clean cation ordering into the lowest-energy variant, we want the energy difference of this structure relative to the higher-energy configurations (Δ_1 and Δ_2) to be high. We arbitrarily choose a value of $\Delta_1 > 0.15$ eV as the difference in energy between the lowest-energy and next-lowest-energy variants. There are still 65 compounds satisfying these criteria, and 59 of them have $d_{14} > 2.6$ pC/N, the experimental value of GaAs, a compound actually used for its piezoelectric properties. We present all the 65 compounds in Table 5.4.

Table 5.4: Best sixty five remaining half-Heusler compounds, ranked according to piezoelectric coefficient d_{14} . None of the initial top twelve presented in Table 5.3 remain after considering band gap, stability, cost and toxicity.

ABC	a (Å)	E_{gap} (eV)	d_{14} (pC/N)	C_{44} (10^{11} Pa)	k_{14}	ϵ_0	Space group
LiY <u>C</u>	5.833	0.72	58.527	0.169	17.54	0.52	-
CuY <u>Ge</u>	6.362	0.47	55.308	0.186	20.18	0.49	$P6_3/mmc$
AgY <u>Si</u>	6.551	0.56	47.326	0.143	18.79	0.40	$P\bar{6}2m$
MgCa <u>Si</u>	6.790	0.62	43.998	0.192	18.17	0.43	$Pnma$
MgCa <u>Ge</u>	6.810	0.57	42.563	0.190	19.25	0.41	$Pnma$
NaSc <u>C</u>	5.766	0.61	38.240	0.316	21.12	0.44	-
LiY <u>Si</u>	6.584	0.54	38.211	0.169	19.91	0.35	$P\bar{6}2m$
LiY <u>Ge</u>	6.584	0.52	37.497	0.169	20.41	0.34	$P\bar{6}2m$
ZnSc <u>B</u>	5.630	0.28	36.869	0.316	23.70	0.41	-
AgY <u>Ge</u>	6.563	0.52	36.248	0.173	19.35	0.34	-
MgZn <u>C</u>	5.216	0.80	35.538	0.497	20.14	0.51	-
NaAl <u>Si</u>	6.256	0.34	35.417	0.268	19.25	0.41	$P4/nmm$
NiSc <u>P</u>	5.790	0.49	34.069	0.302	19.75	0.41	$Pnma$
CaSr <u>Ge</u>	7.570	0.30	33.937	0.121	24.27	0.25	$Pnma$
MgCa <u>Sn</u>	7.100	0.34	32.615	0.192	21.78	0.31	$Pnma$
Li <u>BC</u>	4.202	1.87	31.526	0.743	9.05	0.69	-
NaMg <u>P</u>	6.326	1.38	31.281	0.261	11.34	0.45	-
CaSr <u>Sn</u>	7.867	0.33	29.933	0.123	26.53	0.21	$Pnma$
CaSr <u>Si</u>	7.546	0.34	29.746	0.130	22.44	0.23	$Pnma$
NaMg <u>Sb</u>	6.867	1.05	29.738	0.206	15.14	0.35	$P4/nmm$
NiZr <u>Ge</u>	5.988	0.64	27.413	0.462	24.77	0.37	-
NiZr <u>Si</u>	5.967	0.67	26.401	0.511	23.90	0.38	-
CuSc <u>C</u>	5.460	0.82	24.491	0.489	17.79	0.40	-
NaSc <u>Ge</u>	6.621	0.53	23.529	0.227	23.07	0.24	-
NaSc <u>Si</u>	6.607	0.55	22.534	0.236	22.23	0.24	-
NiHf <u>Si</u>	5.892	0.62	20.423	0.641	23.04	0.34	-
NiHf <u>Ge</u>	5.914	0.58	19.653	0.628	24.03	0.32	-
NaSc <u>Sn</u>	6.947	0.36	19.457	0.179	27.92	0.16	-
NaSr <u>Sb</u>	7.690	1.21	18.257	0.105	11.11	0.19	-
CuB <u>Zr</u>	5.662	0.37	16.889	0.585	29.79	0.24	-
NaSr <u>P</u>	7.155	1.07	16.493	0.130	10.07	0.20	$P\bar{6}2m$
LiAg <u>S</u>	5.889	0.34	14.329	0.253	15.04	0.19	-
NiZr <u>Sn</u>	6.129	0.60	13.658	0.670	28.38	0.22	$F\bar{4}3m$
LiZn <u>As</u>	5.807	0.61	13.511	0.577	20.08	0.24	$F\bar{4}3m$
NiSc <u>Sb</u>	6.039	0.30	12.575	0.695	22.96	0.23	$F\bar{4}3m$
LiZn <u>P</u>	5.638	1.11	12.093	0.571	15.92	0.24	$F\bar{4}3m$
LiSc <u>C</u>	5.420	0.98	11.098	0.440	17.16	0.19	-
AgB <u>Zr</u>	5.872	0.38	10.953	0.285	28.73	0.12	-

Continued on next page

Table 5.4 – continued from previous page

ABC	a (Å)	E_{gap} (eV)	d_{14} (pC/N)	C_{44} (10^{11} Pa)	k_{14}	ϵ_0	Space group
<u>NiHfSn</u>	6.058	0.52	10.905	0.787	28.38	0.19	$F\bar{4}3m$
<u>LiScSi</u>	6.257	0.54	10.835	0.265	20.78	0.13	-
<u>LiScGe</u>	6.264	0.52	10.572	0.262	21.12	0.12	-
<u>NaCaN</u>	6.111	0.75	10.294	0.252	11.06	0.16	-
<u>NiTiSi</u>	5.599	0.64	8.168	0.920	24.87	0.16	$Pnma$
<u>LiGaC</u>	4.742	0.89	7.656	1.390	12.65	0.26	-
<u>LiZnN</u>	4.849	0.72	7.595	0.822	15.39	0.18	$F\bar{4}3m$
<u>CuAlC</u>	4.985	0.34	6.783	1.513	26.25	0.17	-
<u>NiTiGe</u>	5.625	0.60	6.595	0.955	25.61	0.13	$Pnma$
<u>NaYC</u>	6.075	0.43	6.423	0.330	20.72	0.09	-
<u>AgBHf</u>	5.795	0.31	6.241	0.377	26.00	0.08	-
<u>LiMgN</u>	4.973	2.38	6.074	0.732	9.65	0.18	$Pnma^*$
<u>AgScSi</u>	6.213	0.34	5.743	0.356	21.26	0.08	-
<u>AgScGe</u>	6.234	0.30	5.350	0.359	21.48	0.07	-
<u>LiCaI</u>	4.866	0.79	5.320	1.250	12.32	0.18	-
<u>LiCuTe</u>	5.878	0.58	5.172	0.587	19.06	0.10	-
<u>AgScC</u>	5.694	0.39	4.897	0.322	20.12	0.07	-
<u>LiCuS</u>	5.471	0.84	3.502	1.387	11.93	0.13	-
<u>LiMgP</u>	5.936	1.38	3.237	0.458	11.33	0.07	$F\bar{4}3m$
<u>NaCaP</u>	6.886	1.65	3.079	0.211	9.82	0.05	-
<u>LiMgBi</u>	6.721	0.44	2.634	0.265	17.98	0.03	-
<u>NaCaSb</u>	7.391	1.34	2.065	0.161	10.96	0.03	-
<u>NaCaBi</u>	7.520	0.86	1.643	0.145	11.58	0.02	-
<u>NaYSi</u>	6.870	0.44	1.461	0.227	21.14	0.02	-
<u>NaYGe</u>	6.879	0.42	1.428	0.220	22.15	0.02	-
<u>LiMgSb</u>	6.516	0.69	0.265	0.314	15.76	0.00	$F\bar{4}3m$
<u>NiTiSn</u>	5.824	0.50	0.187	0.900	29.04	0.00	$F\bar{4}3m$

Before ending this section, let us present one more analysis of ΔR vs. $\Delta\chi$ distribution (Fig. 5.9), this time for the lowest-energy configurations of all non-metallic cases (red crosses), the 65 piezoelectrics listed in Table 5.4 (blue circles), and the unstable combinations listed in Table 5.5 (green triangles). We see that the most candidates of the latter two categories are those which have a small and strongly negative element in the combination, since most of them are seen to cluster in the region spanned by the positive- $\Delta\chi$ and the negative ΔR semi-axes. This behavior is understandable, however, since good piezoelectrics (having

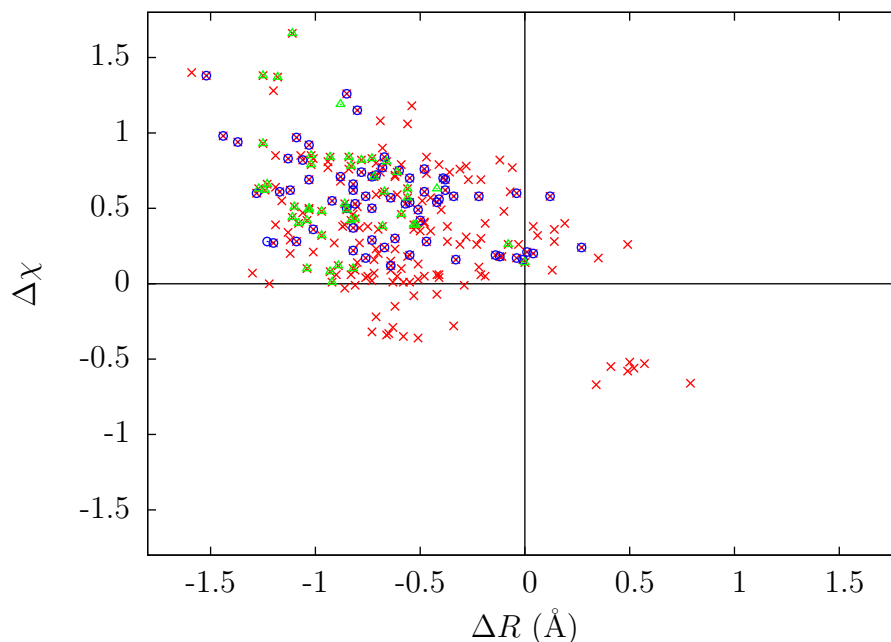


Figure 5.9: Deviation of electronegativity and pseudopotential radius of the tetrahedrally coordinated species for the lowest-energy configurations of all insulators (red crosses), the best-ranked sixty five combinations (blue circles), and the unstable combinations (green triangles).

a large d_{14}) typically have a small C_{44} .

5.4.1 Further investigation

It is surprising that half-Heusler compounds have not been reported for their piezoelectric properties yet. Once a low-conducting single-crystal sample is synthesized for a particular half-Heusler compound, the piezoelectric effect should be measurable for it. In principle these could be measured by using piezoresponse force microscopy (PFM), or by looking at the strain response to an applied electric field. Measurements of the dielectric response and elastic coefficients, for which we do not find any data either, would provide further confirmation of the theoretical predictions, and a more exhaustive characterization of the polarization-related properties of these otherwise popular class of compounds.

Hence it is critical for future investigation of the half-Heusler piezoelectrics to test the possibility of experimentally realizing the desired compounds in the half-Heusler structure, along with measurement of piezoelectric properties of those which are already reported to exist in the half-Heusler structures. Information about bulk equilibrium ABC phases can be obtained from the ICSD. When no entry is found in ICSD corresponding to a combination, it could either mean that no stable bulk phase exists with that stoichiometry of a half-Heusler (for example, it may phase separate into a collection of binary compounds), or simply that the composition in question has not been looked into. There are several other structures that ABC combinations are also reported to exist in, apart from the half-Heusler structure. Nine combinations listed in Table 5.4 are reported in the ICSD with other structures: MgSrSi, MgCaSi and MgCaGe reportedly have structures in the $Pnma$ space group, while NaBaP, AgYSi and LiYSi are reported to have structures with $P\bar{6}2m$ symmetry. The latter space group happens to be piezoelectric, so these compounds provide have an alternative path to new piezoelectrics. Moreover, 13 of the original 792 combinations are reported in more than one space group, namely LiMgN, LiSrP, LiBaP, LiAlGe, CuMgAs, AgCaBi, CuScSn, CuYSn, AuScSn, CaZnSn, PdTiGe, NaAgO and LiAuS. Of these, only AuScSn is reported to have the half-Heusler structure.

This wide range of structural variety makes further investigation of these systems for piezoelectricity and other functional behavior full of possibilities. Because of polymorphism, one may succeed in intentionally stabilizing one of several competing structures, or switching between them using external stresses, fields, or other perturbations. Furthermore, these systems with their possible variations may even let us combine piezoelectricity with other functional properties, including magnetism, to produce multifunctional materials. This is of fundamental scientific interest, and with good luck, might even lead to groundbreaking

technological applications. Indeed, our current work is along this direction. First-principles calculations for various possible structures belonging to different space groups could be used to identify the one having lowest energy.

A related aspect we intend to investigate involves studying the combinations which show elastic instability. In Table 5.5 we present the lowest phonon frequency at the X , L and W points along with the elastic constants C_{11} , C_{12} and C_{44} for all unstable combinations. We do not see any soft mode at the zone center, so the lowest mode there is a set of zero frequency acoustic modes, which we do not include in the table. The first thing to notice is the unusual resistance of these compounds towards zone-center instability. We suspect that this is related to the fact that there are three available configurations to choose from for the half-Heusler structure. It offers enough flexibility to constituent atoms to choose positions which would accommodate them without pushing each other around much. Incidentally, we have done more calculations which suggest that this class of compounds is highly resistant to zone-center instability. We have looked into hundreds of full-Heusler combinations (ABAC -type belonging to the $F\bar{4}3m$ and A_2BC -type belonging to the $Fm\bar{3}m$ space group) and several hundred more mixed-Heusler combinations (ABCD structure type, three configurations belonging to $F\bar{4}3m$ space group), and found no clear case of zone-center instability. Furthermore, we choose a small set of seven half-Heusler compounds and epitaxially constrain them in a plane perpendicular to the body diagonal of the conventional unit cell. This brings down the symmetry from cubic to rhombohedral, and the new structures belong to space group $R\bar{3}m$. This space group can show polarization, and we see that polarization develops as we move away from zero strain, as shown in Fig. 5.10. However, it is easy to see that the polarization that develops with moderate strain ($<2\%$) is not significant (and the response is quite linear). In other words, this behavior just reflects its piezoelectric response.

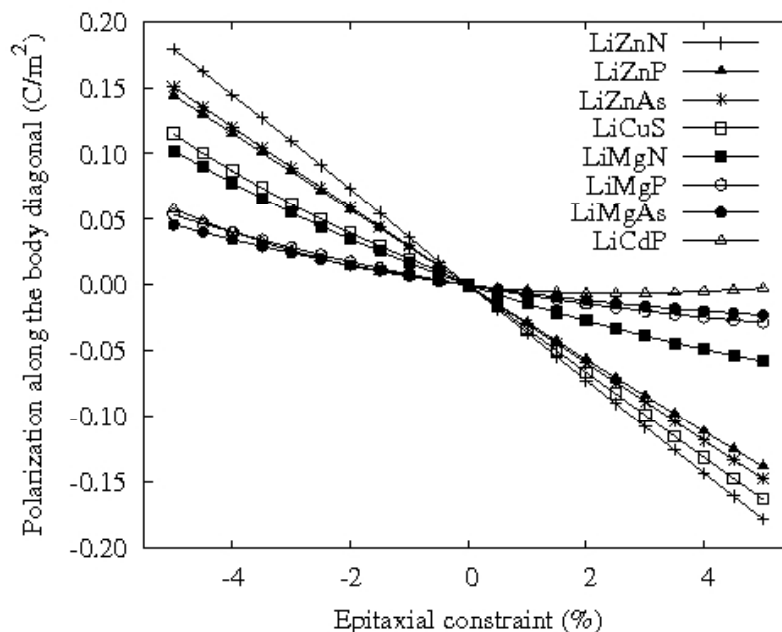


Figure 5.10: Induced polarization in epitaxially constrained half-Heusler compounds.

This indicates how stable the elements are in their high-symmetry positions, and why it may be so difficult to dislodge them. This polarization developed here is not a route to ferroelectricity, by the way, since it is not switchable.

The other interesting thing we note is how rare it is to have a soft mode at the L point for all these unstable combinations. We have an instability at the L point only in two cases, CuBC and BeCdC , out of over forty cases. We are yet to understand this in the context of the physical structure of half-Heuslers. It is easy to realize why studying these results is relevant. In material science we often find enhanced properties close to a related structural phase transition. Here we have a similar situation. We already found that a small positive C_{44} increases the value of the electromechanical coupling factor k_{14} , making it a much better piezoelectric. On the other hand, a decreasing C_{44} indicates that the structure is getting to a point where it can no longer withstand shear stress, and instability sets in as C_{44} becomes negative. One goal of material design is to identify such tipping points,

and predictably control compounds from reaching those, maximizing response in the process.

We are also interested to understand what stable structures these instabilities lead to. To investigate that we can introduce distortions by hand consistent with the soft-mode eigenvectors to find a lower-symmetry structure, followed by structure-relaxation calculations, while making sure that the new structure is stable and shows no more soft modes. Could the end result be one of the space groups featured in the rightmost column of Table 5.5, as reported in ICSD for those combinations? We hope answering these questions would broaden our understanding of the half-Heusler class of compounds.

Table 5.5: List of unstable half-Heusler compounds. Phonon frequency at Γ point is not included, since in no instability is found at Γ for any of the combinations. The minimum phonon frequency is noted for the X , L and W point.

ABC	C_{11}	C_{44} (10^{11} Pa)	C_{12}	$\omega_{\min}^{(X)}$	$\omega_{\min}^{(L)}$ (cm^{-1})	$\omega_{\min}^{(W)}$	Space group
LiNaO	1.36	-0.16	0.39	-119.5	141.6	-134.1	-
NaCuS	2.14	-1.00	0.50	-87.0	15.4	-85.8	-
NaCuTe	0.89	-0.04	0.06	69.9	79.1	75.4	$P4/nmm$
LiCaN	1.27	-0.27	0.22	-136.9	116.3	-146.2	$Pnma$
LiSrN	1.23	-0.35	0.28	-131.8	70.0	-137.4	-
LiSrP	0.68	-0.06	0.22	-55.1	62.8	-57.6	$P\bar{6}2m^*$
LiSrAs	0.61	-0.03	0.20	-36.1	51.4	-38.0	-
LiBaP	0.57	-0.17	0.20	-77.0	35.8	-78.6	$P\bar{6}2m^*$
LiBaAs	0.52	-0.13	0.19	-58.7	33.1	-60.0	$P\bar{6}2m$
BeNaN	2.80	-2.79	0.39	-329.0	54.1	-337.3	$P\bar{6}2m$
BeNaP	1.79	-0.01	0.23	26.0	186.3	76.1	$P\bar{6}2m$
MgCuP	0.23	0.26	0.50	86.4	80.7	85.7	$P\bar{6}2m$
CaCuP	0.91	-1.13	0.23	-110.5	21.7	-111.2	$P\bar{6}2m$
CaAgP	1.16	-0.08	0.31	-43.7	74.6	-47.0	$P\bar{6}2m$
SrAgP	0.90	-0.36	0.33	-60.8	37.0	-59.9	$P\bar{6}2m$
CuYC	3.13	-0.75	0.16	-101.5	118.5	-109.9	-
YAuSi	1.65	-0.01	0.52	-44.1	65.0	-54.2	-
NaBC	3.61	-2.31	0.23	-338.9	196.6	-340.1	-
CuBC	9.58	-7.43	3.18	-306.8	-161.9	-285.2	-
NaBSi	2.70	-0.03	0.07	36.5	239.1	-42.6	-
NaAl	2.78	-0.26	0.14	-110.7	243.6	-133.8	-

Continued on next page

Table 5.5 – continued from previous page

ABC	C_{11}	C_{44} (10^{11}Pa)	C_{12}	$\omega_{\min}^{(X)}$	$\omega_{\min}^{(L)}$ (cm^{-1})	$\omega_{\min}^{(W)}$	Space group
<u>NaCGa</u>	2.75	-0.40	0.19	-98.2	163.8	-113.5	-
<u>BeMgC</u>	3.91	-0.21	0.16	-130.5	263.1	-163.1	-
<u>BeCaC</u>	1.91	-1.43	0.14	-253.3	94.0	-257.1	-
<u>BeZnC</u>	4.09	-0.07	0.84	-52.9	144.5	-35.0	-
<u>BeSrSi</u>	1.33	-0.23	0.11	-83.6	100.4	-64.4	-
<u>BeCdC</u>	2.71	-5.21	0.79	-195.0	-60.3	-189.8	-
<u>BeBaSi</u>	1.10	-0.39	0.09	-98.6	68.7	-85.1	-
<u>BeBaGe</u>	1.03	-0.32	0.09	-80.8	67.9	-68.6	-
<u>BeBaSn</u>	1.02	-0.17	0.07	-50.1	79.5	-39.0	-
<u>MgCaC</u>	1.68	-0.09	0.09	-79.0	169.5	-96.5	-
<u>MgBaSi</u>	0.68	-0.08	0.16	-41.5	61.8	-41.4	$P4/nmm$
<u>MgBaSn</u>	0.53	-0.01	0.16	7.0	44.2	10.6	$P4/nmm$
<u>CaZnSi</u>	1.19	-0.07	0.22	-53.8	109.6	-60.2	$P6_3/mmc$
<u>CaZnGe</u>	1.01	-0.04	0.20	-38.6	83.6	-45.5	$P6_3/mmc$
<u>BeYB</u>	2.19	-0.29	0.33	-96.2	129.1	-94.7	-
<u>ZnYB</u>	2.63	-0.09	0.20	-53.4	152.6	-68.1	-
<u>CaBAl</u>	1.83	-0.11	0.05	-80.0	178.6	-93.9	-
<u>SrBAl</u>	1.54	-0.34	0.07	-103.0	120.2	-103.0	-
<u>CaBGa</u>	1.79	-0.23	0.07	-83.4	125.6	-89.3	-
<u>SrBGa</u>	1.48	-0.42	0.09	-95.1	95.9	-92.2	-
<u>NiZrC</u>	4.04	-0.59	1.06	-109.6	119.9	-130.0	-
<u>NiHfC</u>	4.17	-0.33	1.15	-79.7	107.4	-100.5	-
<u>NiYAs</u>	1.57	-0.24	0.69	-57.1	57.2	-46.0	-
<u>YPdP</u>	1.65	-0.23	0.68	-63.1	60.7	-69.1	-

With the right group-theoretical analysis one can identify systems with piezoelectric structures or other desired properties as low-energy alternatives. The suitable candidates, even if in metastable state, could be stabilized using compositional substitution or epitaxial strain.

5.5 Summary

To summarize, we have performed high-throughput first-principles calculations as a guide to a rational-design approach, and demonstrated semiconducting half-Heusler compounds as a class of piezoelectric materials not investigated previously. We have presented the results of our calculations first for all the non-metallic combinations, followed by identifying compounds already reported in the half-Heusler structure. We have analyzed our results further to extend them for future work, especially to explore related structures showing desirable properties. The work is still underway at the time of preparation of this thesis, and we hope that our results will be able to guide experimental efforts and further investigation of high-performance half-Heusler compounds. The breadth of this work may excite materials scientists to look for ways to combine piezoelectric properties with other known properties of Heuslers, especially magnetic properties, to develop new multifunctional materials.

Bibliography

- Aliev, F. G., Brandt, N. B., Kozyr'kov, V. V., Moshchalkov, V. V., Skolozdra, R. V., Stadnyk, Y. V., & Pecharskii, V. K. 1987, *J. Exp. Theor. Phys. Lett.*, 45, 684
- Ascher, E., Rieder, H., Schmid, H., & Stössel, H. 1966, *J. Appl. Phys.*, 37, 1404
- Balke, B., Barth, J., Schwall, M., Fecher, G. H., & Felser, C. 2011, *Journal of Electronic Materials*, 40, 702
- Baroni, S., de Gironcoli, S., Dal Corso, A., & Giannozzi, P. 2001, *Rev. Mod. Phys.*, 73, 515
- Baroni, S., Giannozzi, P., & Testa, A. 1987, *Phys. Rev. Lett.*, 59, 2662
- Béa, H., et al. 2009, *Phys. Rev. Lett.*, 102, 217603
- Belik, A. A., et al. 2006, *Chem. Mater.*, 18, 798
- Belsky, A., Hellenbrandt, M., Karen, V. L., & Luksch, P. 2002, *Acta Cryst.*, B58, 364
- Berry, M. V. 1984, *Proceedings of the Royal Society of London. A. Mathematical and Physical Sciences*, 392, 45
- Bloch, F. 1929, *Zeitschrift fur Physik*, 52, 555
- Blöchl, P. E. 1994, *Phys. Rev. B*, 50, 17953
- Born, M., & Huang, K. 1954, *Dynamical Theory of Crystal Lattices* (Oxford University Press, Oxford), we used Eq. (33.28) from this book.
- Burton, B. P., & Cockayne, E. 1999, *Phys. Rev. B*, 60, R12542
- Casper, F., Seshadri, R., & Felser, C. 2009, *Phys. Status Solidi A*, 206, 1090
- Ceperley, D. 1978, *Phys. Rev. B*, 18, 3126
- Ceperley, D. M., & Alder, B. J. 1980, *Phys. Rev. Lett.*, 45, 566
- Chadov, S., Qi, X., Kubler, J., Fecher, G. H., Felser, C., & Zhang, S. C. 2010, *Nature Mater.*, 9, 541
- Chen, L., Nagarajan, V., Ramesh, R., & Roytburd, A. L. 2003, *J. Appl. Phys.*, 94, 5147

- Davies, P., Wu, H., Borisevich, A., Molodetsky, I., & Farber, L. 2008, *Annual Reviews of Materials Research*, 38, 369
- de Gennes, P. G. 1960, *Phys. Rev.*, 118, 141
- deGroot, R. A., Mueller, F. M., vanEngen, P. G., & Buschow, K. H. J. 1983, *Phys. Rev. Lett.*, 50, 2024
- Diéguez, O., Rabe, K. M., & Vanderbilt, D. 2005, *Phys. Rev. B*, 72, 144101
- Diéguez, O., & Vanderbilt, D. 2006, *Phys. Rev. Lett.*, 96, 056401
- Ducau, M., Suh, K., Senegas, J., & Darriet, J. 1992, *Materials Research Bulletin*, 27, 1115
- Ederer, C., & Spaldin, N. A. 2005, *Phys. Rev. Lett.*, 95, 257601
- Felser, C., Fecher, G. H., & Balke, B. 2007, *Angew. Chem. Int. Ed.*, 46, 668
- Fennie, C. J., & Rabe, K. M. 2006, *Phys. Rev. Lett.*, 97, 267602
- Fock, V. 1930, *Zeitschrift für Physik A Hadrons and Nuclei*, 61, 126
- Fu, H., & Bellaïche, L. 2003, *Phys. Rev. Lett.*, 91, 057601
- Fu, H., & Cohen, R. E. 2000, *Nature*, 403, 281
- Georges, A., Kotliar, G., Krauth, W., & Rozenberg, M. J. 1996, *Rev. Mod. Phys.*, 68, 13
- Gonze, X., & Lee, C. 1997, *Phys. Rev. B*, 55, 10355
- Gonze, X., et al. 2002, *Comput. Mater. Sci.*, 25, 478
- . 2005, *Z. Kristall.*, 220, 558
- . 2009, *Computer Physics Communications*, 180, 2582 , 40 YEARS OF CPC: A celebratory issue focused on quality software for high performance, grid and novel computing architectures
- Graf, T., Casper, F., Winterlik, J., Balke, B., Fecher, G. H., & Felser, C. 2009, *Zeitschrift für anorganische und allgemeine Chemie*, 635, 976
- Grigoriev, A., Sichel, R., Lee, H. N., Landahl, E. C., Adams, B., Dufresne, E. M., & Evans, P. G. 2008, *Phys. Rev. Lett.*, 100, 027604
- Gruhn, T. 2010, *Phys. Rev. B*, 82, 125210
- Hamann, D. R., Wu, X., Rabe, K. M., & Vanderbilt, D. 2005, *Phys. Rev. B*, 71, 035117
- Hartree, D. R. 1928, *Proc. Cambridge Phil. Soc.*, 24, 89,111,426

- Heusler, F., Stark, W., & E, H. 1903, *Verh. d. DPG*, 5, 220
- Hohenberg, P., & Kohn, W. 1964, *Phys. Rev.*, 136, B864
- Hylleraas, E. 1930, *Zeitschrift fr Physik A Hadrons and Nuclei*, 65, 209
- Hylleraas, E. A. 1929, *Zeitschrift fr Physik A Hadrons and Nuclei*, 54, 347
- Íñiguez, J., & Vanderbilt, D. 2002, *Phys. Rev. Lett.*, 89, 115503
- Kandpal, H. C., Felser, C., & Seshadri, R. 2006, *J. Phys. D.*, 39, 776
- Karki, B. B., Ackland, G. J., & Crain, J. 1997, *Journal of Physics: Condensed Matter*, 9, 8579
- Kieven, D., Lenk, R., Naghavi, S., Felser, C., & Gruhn, T. 2010, *Phys. Rev. B.*, 81, 075208
- King, G., & Woodward, P. M. 2010, *J. Mater. Chem.*, 20, 5785
- King-Smith, R. D., & Vanderbilt, D. 1993, *Phys. Rev. B*, 47, 1651
- Knapp, M. C., & Woodward, P. M. 2006, *Journal of Solid State Chemistry*, 179, 1076
- Kohn, W., & Sham, L. J. 1965, *Phys. Rev.*, 140, A1133
- Kuriyama, K., Kushida, K., & Taguchi, R. 1998, *Solid State Comm.*, 108, 429
- Kuriyama, K., Nagasawa, K., & Kushida, K. 2002, *J. Cryst. Growth*, 237-239, 2019
- Lee, H. N., Christen, H. M., Chisholm, M. F., Rouleau, C. M., & Lowndes, D. H. 2005, *Nature*, 433, 395
- Lee, J. H., & Rabe, K. M. 2010, *Phys. Rev. Lett.*, 104, 207204
- Lin, H., Wray, A., Xia, Y., Xu, S., Jia, S., Cava, R. J., Bansil, A., & Hasan, M. Z. 2010, *Nature Mater.*, 9, 546
- M. Fuchs, M. S. 1999, *Comput. Phys. Commun.*, 119, 67
- Martin, R. 2004, *Electronic Structure: Basic Theory and Practical Methods* (Cambridge University Press, Oxford)
- Mermin, N. D. 1965, *Phys. Rev.*, 137, A1441
- Ming, X., Meng, X., Hu, F., Wang, C.-Z., Huang, Z.-F., Fan, H.-G., & Chen, G. 2009, *J. Phys.: Condens. Matter*, 21, 295902
- Monkhorst, H. J., & Pack, J. D. 1976, *Phys. Rev. B*, 13, 5188

- Nagarajan, V., et al. 2002, *Appl. Phys. Lett.*, 81, 4215
- Nelmes, R. J. 1974, *Journal of Physics C: Solid State Physics*, 7, 3840
- Nolas, G. S., Poon, J., & Kanatzidis, M. 2006, *MRS Bulletin*, 31, 199
- Nowotny, H., & Bachmayer, K. 1950, *Monatsch. Chem.*, 81, 488
- Nunes, R. W., & Gonze, X. 2001, *Phys. Rev. B*, 63, 155107
- Ogut, S., & Rabe, K. M. 1995, *Phys. Rev. B.*, 51, 10443
- Payne, M. C., Teter, M. P., Allan, D. C., Arias, T. A., & Joannopoulos, J. D. 1992, *Rev. Mod. Phys.*, 64, 1045
- Perdew, J. P., & Wang, Y. 1992, *Phys. Rev. B*, 45, 13244
- Perdew, J. P., & Zunger, A. 1981, *Phys. Rev. B*, 23, 5048
- Perez-Mato, J. M., Aroyo, M., García, A., Blaha, P., Schwarz, K., Schweifer, J., & Parlinski, K. 2004, *Phys. Rev. B*, 70, 214111
- Phani, M. K., Lebowitz, J. L., & Kalos, M. H. 1980, *Phys. Rev. B*, 21, 4027
- Rabe, K., & Ghosez, P. 2007, in *Modern Ferroelectrics.*, ed. C. Ahn & K. Rabe (Springer-Verlag), 117–172
- Rabe, K. M. 2005, *Current Opinion in Solid State and Materials Science*, 9, 122
- Ramer, N. J., & Rappe, A. M. 1999, *Phys. Rev. B*, 59, 12471
- Resta, R. 1994, *Rev. Mod. Phys.*, 66, 899
- Resta, R., & Vanderbilt, D. 2007, in *Physics of Ferroelectrics: A Modern Perspective*, 1st edn., ed. K. M. Rabe, C. H. Ahn, & J.-M. Triscone (Springer Publishing Company, Incorporated), 31–68
- Rijnders, G., Blok, J., & Blank, D. 2010, <http://meetings.aps.org/link/-BAPS.2010.MAR.P24.10>.
- Roy, A., Bennett, J. W., Rabe, K. M., & Vanderbilt, D. 2011, arXiv:1107.5078v1
- Roy, A., Stengel, M., & Vanderbilt, D. 2010, *Phys. Rev. B*, 81, 014102
- Roy, A., & Vanderbilt, D. 2011, *Phys. Rev. B*, 83, 134116
- Sai, N., Meyer, B., & Vanderbilt, D. 2000, *Phys. Rev. Lett.*, 84, 5636
- Sai, N., Rabe, K. M., & Vanderbilt, D. 2002, *Phys. Rev. B*, 66, 104108
- Sarma, D. D. 2001, *Current Opinion in Solid State and Materials Science*, 5, 261

- Schmid, H. 1970, *Physica Status Solidi (B)*, 37, 209
- Shen, Q., Chen, L., Goto, T., Hirai, T., Yang, J., Meisner, G. P., & Uher, C. 2001, *Appl. Phys. Lett.*, 79, 4165
- Souza, I., Íñiguez, J., & Vanderbilt, D. 2002, *Phys. Rev. Lett.*, 89, 117602
- Stachiotti, M. G., Rodriguez, C. O., Ambrosch-Draxl, C., & Christensen, N. E. 2000, *Phys. Rev. B*, 61, 14434
- Stengel, M., & Spaldin, N. A. 2006, *Phys. Rev. B*, 73, 075121
- . 2007, *Phys. Rev. B*, 75, 205121
- Stengel, M., Spaldin, N. A., & Vanderbilt, D. 2009a, *Nature Physics*, 5, 304
- Stengel, M., Vanderbilt, D., & Spaldin, N. A. 2009b, *Nature Materials*, 8, 392
- . 2009c, *Phys. Rev. B*, 80, 224110
- Taylor, P. L., & Heinonen, O. 2002, *A Quantum Approach to Condensed Matter Physics* (Cambridge University Press, Oxford)
- Tinte, S., Rabe, K. M., & Vanderbilt, D. 2003, *Phys. Rev. B*, 68, 144105
- Tsai, M.-H., Tang, Y.-H., & Dey, S. K. 2003, *Journal of Physics: Condensed Matter*, 15, 7901
- Umari, P., & Pasquarello, A. 2002, *Phys. Rev. Lett.*, 89, 157602
- Vanderbilt, D. 1990, *Phys. Rev. B*, 41, 7892
- Vanderbilt, D., & Resta, R. 2006, in *Conceptual foundations of materials properties: A standard model for calculation of ground- and excited-state properties*, 1st edn., ed. S. G. Louie & M. L. Cohen (Elsevier, The Netherlands), 139–163
- Warusawithana, M. P., Colla, E. V., Eckstein, J. N., & Weissman, M. B. 2003, *Phys. Rev. Lett.*, 90, 036802
- Wood, D. M., Zunger, A., & deGroot, R. 1985, *Phys. Rev. B*, 31, 2570
- Wu, X., Stengel, M., Rabe, K. M., & Vanderbilt, D. 2008, *Phys. Rev. Lett.*, 101, 087601
- Wu, X., Vanderbilt, D., & Hamann, D. R. 2005, *Phys. Rev. B*, 72, 035105
- Zein, N. E. 1984, *Sov. Phys. Solid State*, 26, 1825
- Zener, C. 1951, *Phys. Rev.*, 82, 403
- Zhong, W., King-Smith, R. D., & Vanderbilt, D. 1994, *Phys. Rev. Lett.*, 72, 3618
- Zunger, A. 1980, *Phys. Rev. B*, 22, 5839

Appendix A

Here we present two tables containing results from our calculation for all non-metallic combinations, including those showing instabilities.

Table A.1: Lattice parameter, band gap, Born effective charges, static dielectric constant and space group as reported in ICSD if available. The unstable combinations are marked with †.

ABC	a (Å)	E_g (eV)	Z_A^* (e)	Z_B^* (e)	Z_C^* (e)	ϵ_0	Space group
†LiNaO	5.253	2.74	0.95	0.80	-1.75	7.37	-
LiNaS	6.175	2.90	1.00	0.84	-1.84	7.12	$P4/nmm$
LiNaSe	6.426	2.42	1.01	0.84	-1.86	7.50	$Pnma$
LiNaTe	6.865	2.37	1.04	0.88	-1.92	8.21	$Pnma$
LiCuS	5.471	0.84	1.07	0.92	-1.99	11.93	-
LiCuSe	5.691	0.51	1.08	1.05	-2.13	13.81	-
LiCuTe	5.878	0.58	1.26	0.33	-1.59	19.06	-
LiAgS	5.889	0.34	1.16	1.22	-2.38	15.04	-
LiAgSe	6.096	0.08	1.18	1.33	-2.52	17.00	-
LiAgTe	6.266	0.39	1.38	0.82	-2.21	21.49	-
†NaCuS	5.952	0.01	0.77	1.36	-2.13	24.19	-
†NaCuTe	6.217	0.67	0.92	0.96	-1.88	16.06	$P4/nmm$
NaAgS	6.203	0.13	0.88	1.41	-2.29	14.55	-
NaAgTe	6.543	0.19	1.06	1.19	-2.26	16.85	-
LiBeN	4.356	2.73	0.77	1.62	-2.39	9.91	-
LiBeP	5.307	1.00	0.86	1.41	-2.28	11.44	$P4/nmm$
LiBeAs	5.356	1.63	1.15	0.71	-1.86	14.28	$P4/nmm$
LiBeSb	5.670	0.45	1.16	-0.30	-0.86	18.23	$P6_3mc$
LiBeBi	6.019	0.61	1.32	0.48	-1.81	22.99	-
LiMgN	4.973	2.38	0.79	1.69	-2.48	9.65	$Pnma^*$
LiMgP	5.936	1.38	0.87	1.78	-2.65	11.33	$F\bar{4}3m$
LiMgAs	6.101	1.15	0.90	1.78	-2.67	12.61	$F\bar{4}3m$
LiMgSb	6.516	0.69	0.97	1.83	-2.80	15.76	$F\bar{4}3m$
LiMgBi	6.721	0.44	1.02	1.81	-2.83	17.98	-
†LiCaN	5.908	1.39	0.85	1.72	-2.57	12.82	$Pnma$
LiCaP	6.629	1.73	0.89	1.75	-2.64	10.82	-

Continued on next page

Table A.1 – continued from previous page

ABC	a (Å)	E_g (eV)	Z_A^* (e)	Z_B^* (e)	Z_C^* (e)	ϵ_0	Space group
<u>LiCaAs</u>	6.756	1.61	0.90	1.70	-2.60	11.11	-
<u>LiCaSb</u>	6.691	0.32	0.52	2.37	-2.89	19.41	-
<u>LiCaBi</u>	7.246	1.25	0.92	1.58	-2.49	11.89	$Pnma$
<u>LiZnN</u>	4.849	0.72	0.92	1.89	-2.81	15.39	$F\bar{4}3m$
<u>LiZnP</u>	5.638	1.11	0.99	1.80	-2.80	15.92	$F\bar{4}3m$
<u>LiZnAs</u>	5.807	0.61	1.04	1.89	-2.93	20.08	$F\bar{4}3m$
<u>LiZnSb</u>	6.037	0.09	1.26	0.84	-2.13	29.29	$P6_3mc$
[†] <u>LiSrN</u>	6.107	0.55	0.97	1.68	-2.64	13.39	-
[†] <u>LiSrP</u>	6.943	1.53	0.99	1.71	-2.70	11.38	$P\bar{6}2m^*$
[†] <u>LiSrAs</u>	7.081	1.24	1.01	1.65	-2.65	11.63	-
<u>LiSrSb</u>	6.979	0.23	0.67	2.73	-3.40	23.14	$Pnma$
<u>LiSrBi</u>	7.154	0.33	0.70	2.78	-3.48	25.37	$Pnma$
<u>LiCdP</u>	6.016	0.51	1.10	2.01	-3.11	19.18	$F\bar{4}3m$
<u>LiCdSb</u>	6.479	0.36	1.27	2.01	-3.30	29.13	-
[†] <u>LiBaP</u>	7.291	0.91	1.10	1.66	-2.76	13.20	$P\bar{6}2m^*$
[†] <u>LiBaAs</u>	7.422	0.70	1.11	1.59	-2.70	13.16	$P\bar{6}2m$
<u>LiBaSb</u>	7.281	0.16	0.80	2.99	-3.79	28.34	$P6_3/mmc$
<u>LiBaBi</u>	7.443	0.26	0.83	2.99	-3.81	29.24	-
[†] <u>BeNaN</u>	5.080	1.45	1.73	0.60	-2.32	13.57	-
[†] <u>BeNaP</u>	5.653	2.04	1.34	0.79	-2.13	11.30	-
<u>BeNaAs</u>	5.796	1.65	1.28	0.80	-2.08	12.82	-
<u>BeNaSb</u>	6.096	0.59	0.70	0.83	-1.53	15.38	-
<u>BeNaBi</u>	6.357	0.29	1.09	0.91	-2.01	20.36	-
<u>BeCuP</u>	5.293	0.78	1.75	0.66	-2.40	21.93	-
<u>NaMgN</u>	5.460	0.72	0.66	1.73	-2.39	11.33	-
<u>NaMgP</u>	6.326	1.38	0.74	1.85	-2.59	11.34	-
<u>NaMgAs</u>	6.481	0.80	0.74	1.87	-2.61	12.82	$P4/nmm$
<u>NaMgSb</u>	6.867	1.05	0.81	1.92	-2.73	15.14	$P4/nmm$
<u>NaCaN</u>	6.111	0.75	0.79	1.71	-2.50	11.06	-
<u>NaCaP</u>	6.886	1.65	0.85	1.76	-2.61	9.82	-
<u>NaCaAs</u>	7.022	1.30	0.86	1.73	-2.58	10.30	-
<u>NaCaSb</u>	7.391	1.34	0.90	1.76	-2.66	10.96	-
<u>NaCaBi</u>	7.520	0.86	0.89	1.63	-2.52	11.58	-
<u>NaZnP</u>	6.069	0.37	0.65	2.09	-2.74	17.79	$P4/nmm$
<u>NaZnSb</u>	6.366	0.17	0.84	1.65	-2.52	28.75	$P4/nmm$
<u>NaSrN</u>	6.301	0.03	0.90	1.61	-2.51	11.88	-
<u>NaSrP</u>	7.155	1.07	0.95	1.71	-2.66	10.07	$P\bar{6}2m$
<u>NaSrAs</u>	7.299	0.81	0.96	1.66	-2.62	10.50	$P\bar{6}2m$
<u>NaSrSb</u>	7.690	1.21	1.00	1.73	-2.73	11.11	-
<u>NaSrBi</u>	7.840	0.58	1.00	1.58	-2.58	11.76	-
<u>NaBaP</u>	7.455	0.63	1.04	1.66	-2.70	11.02	$P\bar{6}2m$

Continued on next page

Table A.1 – continued from previous page

ABC	a (Å)	E_g (eV)	Z_A^* (e)	Z_B^* (e)	Z_C^* (e)	ϵ_0	Space group
NaBaAs	7.594	0.43	1.05	1.60	-2.65	11.27	-
NaBaSb	7.966	0.83	1.08	1.65	-2.73	11.52	-
NaBaBi	8.121	0.30	1.09	1.49	-2.58	12.09	$P\bar{6}2m$
†MgCuP	5.738	0.70	1.97	0.91	-2.88	19.95	$P\bar{6}2m$
†CaCuP	6.443	0.27	1.55	1.12	-2.67	20.22	$P\bar{6}2m$
†CaAgP	6.623	0.21	1.58	1.21	-2.79	17.82	$P\bar{6}2m$
†SrAgP	6.828	0.08	1.42	1.36	-2.78	19.56	$P\bar{6}2m$
LiScC	5.420	0.98	0.52	2.85	-3.36	17.16	-
LiScSi	6.257	0.54	0.49	2.82	-3.31	20.78	-
LiScGe	6.264	0.52	0.46	2.74	-3.20	21.12	-
LiScPb	6.708	0.51	0.44	2.38	-2.82	20.79	-
LiYC	5.833	0.72	0.54	2.79	-3.33	17.54	-
LiYSi	6.584	0.54	0.52	2.83	-3.35	19.91	$P\bar{6}2m$
LiYGe	6.584	0.52	0.50	2.76	-3.25	20.41	$P\bar{6}2m$
LiYPb	6.985	0.59	0.47	2.40	-2.87	19.63	-
NaScC	5.766	0.61	0.70	2.85	-3.55	21.12	-
NaScSi	6.607	0.55	0.72	2.79	-3.50	22.23	-
NaScGe	6.621	0.53	0.70	2.73	-3.42	23.07	-
NaScSn	6.947	0.36	0.71	2.81	-3.52	27.92	-
NaScPb	7.022	0.52	0.66	2.45	-3.11	23.89	-
NaYC	6.075	0.43	0.70	2.87	-3.57	20.72	-
NaYSi	6.870	0.44	0.72	2.83	-3.56	21.14	-
NaYGe	6.879	0.42	0.71	2.78	-3.49	22.15	-
NaYSn	7.194	0.34	0.71	2.92	-3.64	27.47	-
NaYPb	7.267	0.49	0.68	2.49	-3.17	22.21	-
ScCuC	5.460	0.82	2.56	0.22	-2.78	17.79	-
ScAgC	5.694	0.39	2.35	0.52	-2.86	20.12	-
ScAgSi	6.213	0.34	2.38	0.05	-2.42	21.26	-
ScAgGe	6.234	0.30	2.20	0.12	-2.32	21.48	-
ScAuSi	6.243	0.31	1.47	-1.95	0.48	20.45	-
ScAuGe	6.279	0.28	1.31	-1.82	0.51	25.71	-
ScAuSn	6.408	0.22	1.25	-2.53	1.28	22.57	-
†CuYC	5.918	0.11	0.68	2.22	-2.90	22.18	-
CuYSi	6.360	0.50	0.19	2.42	-2.61	19.87	$P6_3/mmc$
CuYGe	6.362	0.47	0.24	2.23	-2.47	20.18	$P6_3/mmc$
YAgSi	6.551	0.56	2.34	0.31	-2.64	18.79	$P6_3/mmc$
YAgGe	6.563	0.52	2.13	0.38	-2.51	19.35	$P6_3/mmc$
†YAuSi	6.506	0.47	1.96	0.46	-2.42	22.18	$P6_3/mmc$
YAuSn	6.747	0.10	1.03	-1.75	0.72	26.08	$P6_3/mmc$
LiBC	4.202	1.87	0.80	1.21	-2.01	9.05	-
†NaBC	4.984	1.31	0.38	1.17	-1.55	11.74	-

Continued on next page

Table A.1 – continued from previous page

ABC	a (Å)	E_g (eV)	Z_A^* (e)	Z_B^* (e)	Z_C^* (e)	ϵ_0	Space group
\dagger CuBC	4.548	1.17	0.71	1.22	-1.93	23.72	-
LiBSi	4.948	0.19	0.80	-2.34	1.54	14.09	-
\dagger NaBSi	5.508	0.42	0.47	-1.06	0.59	14.34	-
LiBGe	5.023	0.24	0.86	-2.36	1.51	15.28	-
NaBGe	5.562	0.43	0.44	-1.06	0.62	18.12	-
NaAlSi	6.256	0.34	0.61	1.56	-2.17	19.25	$P4/nmm$
NaAlGe	6.300	0.15	0.55	1.57	-2.13	25.55	$P4/nmm$
TiCuB	5.289	0.20	3.75	-0.95	-2.80	31.33	$P4/nmm$
TiCuAl	5.818	0.04	3.00	-3.44	0.43	51.25	$P4/nmm$
TiCuGa	5.681	0.06	2.77	-3.29	0.51	44.73	$P4/nmm$
TiAgB	5.538	0.24	3.54	-0.69	-2.85	32.36	$P4/nmm$
TiAgAl	6.102	0.16	2.65	-3.14	0.48	39.29	$P4/nmm$
TiAuB	5.546	0.11	3.62	-1.17	-2.45	39.43	$P4/nmm$
TiAuAl	6.097	0.58	2.42	-3.46	1.04	26.49	$P4/nmm$
TiAuGa	6.000	0.63	2.23	-3.37	1.13	25.98	$P4/nmm$
CuZrB	5.662	0.37	-0.85	3.99	-3.14	29.79	$P4/nmm$
CuHfB	5.550	0.29	-0.93	3.95	-3.02	27.19	$P4/nmm$
ZrAgB	5.872	0.38	3.77	-0.64	-3.13	28.73	$P4/nmm$
ZrAuB	5.878	0.34	3.58	-0.89	-2.69	28.10	$P4/nmm$
ZrAuAl	6.401	0.45	2.32	-3.22	0.90	25.94	$P4/nmm$
AgHfB	5.795	0.31	-0.70	3.72	-3.02	26.00	$P4/nmm$
AgHfAl	6.335	0.07	-3.59	3.49	0.04	60.21	$P4/nmm$
HfAuB	5.804	0.32	3.57	-0.94	-2.63	25.76	$P4/nmm$
HfAuAl	6.330	0.57	2.44	-3.39	0.95	25.27	$P4/nmm$
HfAuGa	6.245	0.61	2.21	-3.26	1.06	25.19	$P4/nmm$
LiCaI	4.866	0.79	0.64	-2.93	2.29	12.32	-
\dagger NaCaI	5.436	0.97	0.49	-2.62	2.13	14.71	-
CuCaI	4.985	0.34	0.73	-3.42	2.69	26.25	-
LiCGa	4.742	0.89	0.66	-2.97	2.32	12.65	-
\dagger NaCGa	5.329	0.53	0.40	-2.58	2.18	16.46	-
CuCGa	4.878	0.12	0.96	-3.73	2.76	33.39	-
NaSiGa	6.077	0.03	0.61	-1.78	1.14	28.83	-
\dagger BeMgC	4.902	0.92	1.28	1.60	-2.89	13.10	-
\dagger BeCaC	5.732	1.29	1.34	1.40	-2.73	16.97	-
\dagger BeZnC	4.770	1.13	1.75	1.69	-3.44	23.94	-
\dagger BeSrSi	6.482	0.01	-0.10	2.15	-2.05	29.91	-
\dagger BeCdC	5.215	0.08	1.93	2.18	-4.12	63.87	-
\dagger BeBaSi	6.843	0.27	0.06	2.51	-2.56	46.30	-
\dagger BeBaGe	6.875	0.15	0.11	2.44	-2.55	51.69	-
\dagger BeBaSn	7.045	0.10	-0.55	2.61	-2.08	66.59	-

Continued on next page

Table A.1 – continued from previous page

ABC	a (Å)	E_g (eV)	Z_A^* (e)	Z_B^* (e)	Z_C^* (e)	ϵ_0	Space group
\dagger MgCaC	6.073	0.79	1.57	1.44	-3.01	18.15	-
MgCaSi	6.790	0.62	1.60	1.46	-3.06	18.17	$Pnma$
MgCaGe	6.810	0.57	1.60	1.33	-2.93	19.25	$Pnma$
MgCaSn	7.100	0.34	1.58	1.38	-2.95	21.78	$Pnma$
MgCaPb	7.227	0.32	1.65	1.04	-2.69	22.01	-
MgZnC	5.216	0.80	1.70	1.65	-3.35	20.14	-
MgSrSi	7.086	0.87	1.79	1.38	-3.17	20.63	$Pnma$
MgSrGe	7.112	0.36	1.83	1.20	-3.03	21.95	$Pnma$
MgSrSn	7.407	0.72	1.79	1.35	-3.14	25.56	$Pnma$
\dagger MgBaSi	7.393	0.02	2.01	1.13	-3.13	23.27	$P4/nmm$
\dagger MgBaSn	7.681	0.12	1.97	1.13	-3.09	26.88	$P4/nmm$
\dagger CaZnSi	6.580	0.62	1.14	1.75	-2.89	23.48	$P6_3/mmc$
\dagger CaZnGe	6.598	0.05	0.91	1.86	-2.77	26.54	$P6_3/mmc$
CaSrSi	7.546	0.34	1.91	1.93	-3.84	22.44	$Pnma$
CaSrGe	7.570	0.30	1.89	1.90	-3.78	24.27	$Pnma$
CaSrSn	7.867	0.33	1.93	2.03	-3.97	26.53	$Pnma$
CaSrPb	7.984	0.10	1.78	1.75	-3.52	24.12	$Pnma$
CaCdSi	6.773	0.47	1.17	1.72	-2.89	22.40	-
CaCdSn	7.010	0.22	0.99	1.59	-2.59	26.96	$P\bar{6}2m$
CaBaSi	7.783	0.24	1.98	1.72	-3.70	21.66	$Pnma$
CaBaSn	8.093	0.22	2.02	1.92	-3.94	26.22	$Pnma$
SrCdSi	7.009	0.11	0.95	1.96	-2.90	24.98	-
BeScB	5.387	0.33	0.32	2.74	-3.05	23.84	-
\dagger BeYB	5.773	0.25	0.31	2.87	-3.16	29.33	-
MgScB	5.826	0.10	1.05	3.06	-4.12	44.53	-
ScZnB	5.630	0.28	2.44	0.67	-3.10	23.70	-
ScCdB	5.875	0.23	2.31	0.69	-3.00	22.93	-
\dagger ZnYB	6.076	0.47	0.86	2.40	-3.25	27.22	-
YCdB	6.266	0.37	2.27	0.81	-3.08	25.52	-
\dagger CaBAl	6.067	0.24	1.24	-2.48	1.25	21.03	-
\dagger SrBAl	6.416	0.51	1.18	-2.52	1.35	29.11	-
\dagger CaBGa	5.964	0.32	1.09	-2.40	1.32	22.03	-
\dagger SrBGa	6.330	0.03	0.85	-2.33	1.50	32.04	-
SrAlGa	6.870	0.13	1.18	0.45	-1.63	48.85	-
TiNiC	5.086	0.22	4.33	-2.43	-1.90	35.31	-
TiNiSi	5.599	0.64	2.70	-4.01	1.31	24.87	-
TiNiGe	5.625	0.60	2.63	-3.98	1.36	25.61	-
TiNiSn	5.824	0.50	2.57	-4.32	1.76	29.04	-
TiNiPb	6.199	0.27	2.44	-3.81	1.37	33.44	-
TiPdSi	5.886	0.68	2.53	-3.70	1.16	23.26	-
TiPdGe	5.916	0.65	2.46	-3.68	1.22	24.48	-

Continued on next page

Table A.1 – continued from previous page

ABC	a (Å)	E_g (eV)	Z_A^* (e)	Z_B^* (e)	Z_C^* (e)	ϵ_0	Space group
TiPdSn	6.080	0.54	2.39	-4.00	1.62	27.18	-
TiPdPb	6.421	0.30	2.29	-3.52	1.23	33.61	-
TiPtSi	5.898	1.22	2.73	-4.68	1.95	20.26	-
TiPtGe	5.931	1.22	2.64	-4.64	2.00	21.23	-
TiPtSn	6.079	1.09	2.64	-4.99	2.34	21.92	-
TiPtPb	6.419	0.84	2.35	-4.49	2.14	27.27	-
\dagger NiZrC	5.508	0.22	-1.80	3.98	-2.18	28.06	-
NiZrSi	5.967	0.67	-3.60	2.62	0.97	23.90	-
NiZrGe	5.988	0.64	-3.59	2.56	1.04	24.77	-
NiZrSn	6.129	0.60	-3.97	2.41	1.56	28.38	$F\bar{4}3m$
NiZrPb	6.402	0.31	-3.51	2.42	1.09	28.60	-
\dagger NiHfC	5.414	0.01	-1.61	3.75	-2.15	26.82	-
NiHfSi	5.892	0.62	-3.62	2.66	0.96	23.04	-
NiHfGe	5.914	0.58	-3.61	2.61	1.01	24.03	-
NiHfSn	6.058	0.52	-4.09	2.51	1.58	28.38	$F\bar{4}3m$
NiHfPb	6.348	0.23	-3.57	2.57	0.99	28.93	-
ZrPdSi	6.204	0.65	2.54	-3.30	0.76	21.15	-
ZrPdGe	6.226	0.62	2.46	-3.29	0.83	22.46	-
ZrPdSn	6.354	0.56	2.29	-3.68	1.38	25.02	-
ZrPdPb	6.616	0.30	2.34	-3.22	0.89	28.02	-
ZrPtSi	6.208	1.53	2.60	-4.23	1.63	19.03	-
ZrPtGe	6.235	1.48	2.50	-4.19	1.69	20.26	-
ZrPtSn	6.350	1.42	2.45	-4.62	2.17	20.00	-
ZrPtPb	6.624	0.84	2.25	-4.11	1.86	23.80	-
PdHfSi	6.136	0.61	-3.36	2.61	0.75	20.53	-
PdHfGe	6.160	0.58	-3.36	2.56	0.80	22.25	-
PdHfSn	6.291	0.51	-3.84	2.42	1.42	24.71	$F\bar{4}3m$
PdHfPb	6.565	0.24	-3.36	2.57	0.79	29.77	-
HfPtSi	6.141	1.53	2.58	-4.25	1.67	18.25	-
HfPtGe	6.169	1.27	2.49	-4.21	1.72	19.83	-
HfPtSn	6.287	1.40	2.46	-4.71	2.25	19.28	-
HfPtPb	6.571	0.36	2.33	-4.19	1.86	25.29	-
ScNiP	5.790	0.49	2.37	-2.46	0.09	19.75	-
ScNiAs	5.880	0.41	2.24	-2.52	0.28	22.12	-
ScNiSb	6.039	0.30	1.78	-3.25	1.47	22.96	-
ScNiBi	6.295	0.15	2.01	-2.56	0.55	27.99	-
ScPdP	6.023	0.53	2.69	-0.89	-1.81	21.03	-
ScPdAs	6.152	0.23	2.37	-1.89	-0.48	27.89	-
ScPdSb	6.291	0.31	1.77	-2.87	1.09	21.12	-
ScPtSb	6.269	1.04	1.62	-3.86	2.24	20.31	-
\dagger NiYAs	6.311	0.05	-1.60	2.44	-0.85	29.89	-

Continued on next page

Table A.1 – continued from previous page

ABC	a (Å)	E_g (eV)	Z_A^* (e)	Z_B^* (e)	Z_C^* (e)	ϵ_0	Space group
<u>NiYSb</u>	6.433	0.28	-2.53	1.77	0.75	23.30	$F\bar{4}3m$
[†] <u>YPdP</u>	6.383	0.02	2.45	-0.38	-2.08	19.10	$F\bar{4}3m$
<u>YPdSb</u>	6.633	0.19	1.93	-2.06	0.13	21.81	$F\bar{4}3m$
<u>YPtSb</u>	6.594	0.34	1.39	-2.86	1.46	24.50	$F\bar{4}3m$

Table A.2: Piezoelectric constant, elastic constants, lowest phonon frequency at X , L and W points, and electromechanical coupling factor. The unstable combinations are marked with [†].

ABC	d_{14} (pC/N)	C_{11}	C_{44} (10^{11} Pa)	C_{12}	$\omega_{\min}^{(X)}$	$\omega_{\min}^{(X)}$ (cm^{-1})	$\omega_{\min}^{(X)}$	k_{14}
[†] <u>LiNaO</u>	105.694	1.36	-0.16	0.39	-119.5	141.6	-134.1	-
<u>LiNaS</u>	96.304	0.70	0.08	0.24	74.2	99.3	67.6	0.74
<u>LiNaSe</u>	71.617	0.58	0.10	0.21	64.5	66.3	63.9	0.65
<u>LiNaTe</u>	56.098	0.42	0.09	0.18	52.7	44.9	56.4	0.53
<u>LiCuS</u>	3.502	2.90	1.39	1.44	104.4	88.8	107.4	0.13
<u>LiCuSe</u>	7.936	3.08	0.63	0.72	81.2	61.2	89.2	0.18
<u>LiCuTe</u>	5.172	2.23	0.59	0.48	97.8	67.5	113.2	0.10
<u>LiAgS</u>	14.329	0.94	0.25	0.53	56.6	51.5	60.6	0.19
<u>LiAgSe</u>	6.662	0.80	0.25	0.49	48.7	39.4	54.3	0.09
<u>LiAgTe</u>	19.453	0.75	0.36	0.53	55.0	35.3	64.9	0.26
[†] <u>NaCuS</u>	46.728	2.14	-1.00	0.50	-87.0	15.4	-85.8	-
[†] <u>NaCuTe</u>	124.689	0.89	-0.04	0.06	69.9	79.1	75.4	-
<u>NaAgS</u>	51.119	0.89	0.19	0.44	55.9	61.2	54.1	0.53
<u>NaAgTe</u>	4.279	0.79	0.27	0.40	60.0	48.9	62.0	0.06
<u>LiBeN</u>	36.662	4.39	0.64	0.22	222.6	385.7	182.3	0.70
<u>LiBeP</u>	17.492	1.70	0.60	0.36	201.5	159.4	211.9	0.39
<u>LiBeAs</u>	1.621	1.60	0.73	0.35	164.6	126.8	179.2	0.04
<u>LiBeSb</u>	0.453	1.45	0.68	0.22	111.0	95.3	128.0	0.01
<u>LiBeBi</u>	3.315	1.01	0.48	0.26	75.7	62.0	87.5	0.05
<u>LiMgN</u>	6.074	2.68	0.73	0.27	196.6	258.7	189.9	0.18
<u>LiMgP</u>	3.237	1.17	0.46	0.30	166.1	132.3	176.9	0.07
<u>LiMgAs</u>	2.189	1.00	0.41	0.28	116.1	87.4	129.2	0.04
<u>LiMgSb</u>	0.265	0.71	0.31	0.26	70.9	50.7	86.1	0.00
<u>LiMgBi</u>	2.634	0.59	0.27	0.22	51.0	37.1	62.2	0.03
[†] <u>LiCaN</u>	65.627	1.27	-0.27	0.22	-136.9	116.3	-146.2	-
<u>LiCaP</u>	123.196	0.76	0.07	0.22	49.8	94.4	42.6	0.72
<u>LiCaAs</u>	85.728	0.68	0.08	0.20	50.9	69.5	48.7	0.62
<u>LiCaSb</u>	5.416	0.70	0.24	0.22	74.9	79.5	84.6	0.06
<u>LiCaBi</u>	44.390	0.46	0.10	0.17	41.0	38.4	43.0	0.40
<u>LiZnN</u>	7.595	3.29	0.82	0.53	121.5	162.0	112.9	0.18

Continued on next page

Table A.2 – continued from previous page

ABC	d_{14} (pC/N)	C_{11}	C_{44} (10^{11} Pa)	C_{12}	$\omega_{\min}^{(X)}$	$\omega_{\min}^{(X)}$ (cm^{-1})	$\omega_{\min}^{(X)}$	k_{14}
<u>LiZnP</u>	12.093	1.28	0.57	0.37	119.5	94.9	123.7	0.24
<u>LiZnAs</u>	13.511	1.29	0.58	0.44	94.1	68.3	105.4	0.24
<u>LiZnSb</u>	1.355	1.20	0.59	0.42	80.5	56.5	100.2	0.02
[†] <u>LiSrN</u>	46.804	1.23	-0.35	0.28	-131.8	70.0	-137.4	-
[†] <u>LiSrP</u>	153.713	0.68	-0.06	0.22	-55.1	62.8	-57.6	-
[†] <u>LiSrAs</u>	252.820	0.61	-0.03	0.20	-36.1	51.4	-38.0	-
<u>LiSrSb</u>	3.837	0.72	0.14	0.15	49.2	72.6	60.5	0.03
<u>LiSrBi</u>	6.592	0.62	0.13	0.14	41.9	57.5	50.9	0.05
<u>LiCdP</u>	0.414	1.12	0.44	0.41	76.4	66.1	82.2	0.01
<u>LiCdSb</u>	9.642	0.74	0.34	0.34	38.8	29.0	59.5	0.11
[†] <u>LiBaP</u>	69.476	0.57	-0.17	0.20	-77.0	35.8	-78.6	-
[†] <u>LiBaAs</u>	83.768	0.52	-0.13	0.19	-58.7	33.1	-60.0	-
<u>LiBaSb</u>	29.106	0.71	0.04	0.12	22.4	57.3	40.2	0.11
<u>LiBaBi</u>	10.770	0.63	0.05	0.11	24.1	51.9	37.1	0.05
[†] <u>BeNaN</u>	19.506	2.80	-2.79	0.39	-329.0	54.1	-337.3	-
[†] <u>BeNaP</u>	2052.813	1.79	-0.01	0.23	26.0	186.3	76.1	-
<u>BeNaAs</u>	91.789	1.58	0.10	0.21	71.6	141.0	93.0	0.65
<u>BeNaSb</u>	12.524	1.40	0.26	0.15	90.4	106.3	99.9	0.17
<u>BeNaBi</u>	20.208	1.00	0.24	0.17	69.7	69.7	72.5	0.22
<u>BeCuP</u>	5.874	4.91	1.11	1.64	20.1	15.0	95.8	0.14
<u>NaMgN</u>	190.591	2.05	0.09	0.27	46.8	214.0	-46.7	0.87
<u>NaMgP</u>	31.281	1.04	0.26	0.26	129.7	125.4	122.0	0.45
<u>NaMgAs</u>	31.649	0.90	0.24	0.24	106.1	87.0	105.6	0.42
<u>NaMgSb</u>	29.738	0.66	0.21	0.23	75.4	56.8	82.1	0.35
<u>NaCaN</u>	10.294	1.09	0.25	0.25	99.6	141.9	102.1	0.16
<u>NaCaP</u>	3.079	0.70	0.21	0.21	111.9	101.4	111.6	0.05
<u>NaCaAs</u>	2.347	0.63	0.19	0.20	100.0	75.4	102.9	0.03
<u>NaCaSb</u>	2.065	0.50	0.16	0.18	73.9	54.2	79.7	0.03
<u>NaCaBi</u>	1.643	0.44	0.14	0.16	54.5	41.0	58.3	0.02
<u>NaZnP</u>	344.071	1.18	0.06	0.36	47.6	98.6	38.1	0.90
<u>NaZnSb</u>	23.940	0.97	0.27	0.24	91.5	71.9	93.1	0.24
<u>NaSrN</u>	18.240	1.15	0.12	0.21	67.2	106.3	66.6	0.19
<u>NaSrP</u>	16.493	0.65	0.13	0.19	75.4	77.3	74.7	0.20
<u>NaSrAs</u>	16.506	0.58	0.12	0.18	67.7	62.6	68.5	0.19
<u>NaSrSb</u>	18.257	0.45	0.11	0.17	56.2	47.1	58.9	0.19
<u>NaSrBi</u>	18.905	0.40	0.09	0.15	44.4	36.8	46.7	0.18
<u>NaBaP</u>	68.785	0.56	0.05	0.18	43.0	57.1	42.2	0.45
<u>NaBaAs</u>	60.882	0.50	0.06	0.17	41.1	48.8	41.1	0.41
<u>NaBaSb</u>	54.636	0.40	0.06	0.15	38.5	39.0	39.7	0.38
<u>NaBaBi</u>	54.678	0.36	0.05	0.14	0.0	0.0	33.5	0.36

Continued on next page

Table A.2 – continued from previous page

ABC	d_{14} (pC/N)	C_{11}	C_{44} (10^{11} Pa)	C_{12}	$\omega_{\min}^{(X)}$	$\omega_{\min}^{(X)}$ (cm^{-1})	$\omega_{\min}^{(X)}$	k_{14}
$\dagger\text{MgCuP}$	45.182	0.23	0.26	0.50	86.4	80.7	85.7	-
$\dagger\text{CaCuP}$	30.631	0.91	-1.13	0.23	-110.5	21.7	-111.2	-
$\dagger\text{CaAgP}$	197.529	1.16	-0.08	0.31	-43.7	74.6	-47.0	-
$\dagger\text{SrAgP}$	62.731	0.90	-0.36	0.33	-60.8	37.0	-59.9	-
LiScC	11.098	2.31	0.44	0.42	165.0	198.4	153.8	0.19
LiScSi	10.835	0.99	0.27	0.36	122.8	110.7	116.5	0.13
LiScGe	10.572	0.97	0.26	0.35	99.6	85.7	96.7	0.12
LiScPb	7.891	0.65	0.21	0.30	56.8	46.3	56.1	0.08
LiYC	58.527	1.80	0.17	0.35	81.1	129.4	71.7	0.52
LiYSi	38.211	0.89	0.17	0.31	78.7	83.4	72.9	0.35
LiYGe	37.497	0.87	0.17	0.30	70.3	71.0	65.6	0.34
LiYPb	26.777	0.62	0.16	0.26	47.9	42.7	45.5	0.25
NaScC	38.240	1.84	0.32	0.39	119.5	178.7	100.8	0.44
NaScSi	22.534	0.92	0.24	0.31	132.3	111.7	122.0	0.24
NaScGe	23.529	0.89	0.23	0.30	112.8	85.9	109.4	0.24
NaScSn	19.457	0.66	0.18	0.28	79.1	59.1	82.4	0.16
NaScPb	17.019	0.61	0.18	0.23	59.2	46.4	60.6	0.16
NaYC	6.423	1.47	0.33	0.35	100.9	124.4	101.4	0.09
NaYSi	1.461	0.83	0.23	0.28	97.8	87.7	91.7	0.02
NaYGe	1.428	0.81	0.22	0.27	93.0	74.8	88.0	0.02
NaYSn	3.534	0.62	0.18	0.25	71.9	54.9	71.3	0.03
NaYPb	1.794	0.58	0.17	0.21	56.9	44.4	57.3	0.02
ScCuC	24.491	5.35	0.49	1.04	-44.0	161.8	-72.0	0.40
ScAgC	4.897	3.13	0.32	0.58	26.6	127.9	-3.3	0.07
ScAgSi	5.743	1.57	0.36	0.59	83.3	91.0	73.5	0.08
ScAgGe	5.350	1.51	0.36	0.59	85.2	80.7	75.7	0.07
ScAuSi	16.431	1.51	0.43	0.94	63.8	58.2	60.1	0.25
ScAuGe	17.247	1.40	0.42	0.90	64.9	55.3	61.7	0.23
ScAuSn	10.152	1.59	0.56	0.84	84.0	65.4	82.0	0.17
$\dagger\text{CuYC}$	31.278	3.13	-0.75	0.16	-101.5	118.5	-109.9	-
CuYSi	216.955	1.82	0.05	0.66	-66.8	84.4	-74.5	0.76
CuYGe	55.308	1.49	0.19	0.72	-51.1	73.4	-59.7	0.49
YAgSi	47.326	1.50	0.14	0.45	31.4	93.6	-13.6	0.4
YAgGe	36.248	1.46	0.17	0.44	39.8	82.3	22.6	0.34
$\dagger\text{YAuSi}$	1073.519	1.65	-0.01	0.52	-44.1	65.0	-54.2	-
YAuSn	32.429	1.27	0.24	0.66	45.5	51.4	42.6	0.31
LiBC	31.526	6.36	0.74	0.06	272.7	436.4	255.7	0.69
$\dagger\text{NaBC}$	12.164	3.61	-2.31	0.23	-338.9	196.6	-340.1	-
$\dagger\text{CuBC}$	9.585	9.58	-7.43	3.18	-306.8	-161.9	-285.2	-
LiBSi	6.804	3.47	1.26	0.12	289.1	276.4	296.1	0.21

Continued on next page

Table A.2 – continued from previous page

ABC	d_{14} (pC/N)	C_{11}	C_{44} (10^{11} Pa)	C_{12}	$\omega_{\min}^{(X)}$	$\omega_{\min}^{(X)}$ (cm^{-1})	$\omega_{\min}^{(X)}$	k_{14}
$\dagger\text{NaBSi}$	271.114	2.70	-0.03	0.07	36.5	239.1	-42.6	-
LiBGe	7.268	3.18	1.16	0.15	182.7	175.3	196.6	0.21
NaBGe	304.158	2.43	0.03	0.07	58.7	169.5	36.9	0.79
NaAlSi	35.417	1.20	0.27	0.24	129.7	124.5	123.8	0.41
NaAlGe	37.596	1.11	0.26	0.22	99.9	90.5	98.9	0.37
TiCuB	3.358	5.20	0.71	0.97	102.4	168.7	68.7	0.05
TiCuAl	6.635	3.89	1.46	1.62	158.9	132.4	0.0	0.12
TiCuGa	21.939	1.30	0.55	0.92	143.6	119.5	128.4	0.25
TiAgB	10.879	3.45	0.42	0.71	68.2	134.5	56.9	0.13
TiAgAl	15.845	1.45	0.54	0.93	111.1	87.6	101.3	0.19
TiAuB	3.667	3.89	0.44	0.89	51.2	95.1	19.0	0.04
TiAuAl	9.162	1.80	0.65	1.06	100.4	79.6	95.1	0.15
TiAuGa	10.829	1.82	0.65	1.23	94.3	73.3	87.1	0.18
CuZrB	16.889	5.87	0.59	1.10	21.5	163.5	-59.8	0.24
CuHfB	39.290	3.85	0.23	0.68	47.2	122.9	-22.5	0.36
ZrAgB	10.953	3.36	0.28	0.59	36.1	137.8	-28.0	0.12
ZrAuB	21.666	3.60	0.20	0.70	-26.9	96.2	-57.0	0.19
ZrAuAl	21.717	1.70	0.46	0.98	74.7	67.4	67.4	0.29
AgHfB	6.241	3.50	0.38	0.67	39.3	122.4	10.3	0.08
AgHfAl	11.439	1.55	0.49	0.96	72.3	62.7	63.1	0.29
HfAuB	12.055	3.74	0.33	0.80	14.9	96.9	-41.6	0.14
HfAuAl	16.727	1.84	0.58	1.05	74.4	63.4	67.9	0.26
HfAuGa	21.888	1.77	0.50	1.16	64.4	56.1	57.0	0.31
LiCaAl	5.320	3.72	1.25	0.19	261.8	299.3	249.8	0.18
$\dagger\text{NaCaAl}$	100.986	2.78	-0.26	0.14	-110.7	243.6	-133.8	-
CuCaAl	6.783	4.32	1.51	2.02	76.7	132.7	86.2	0.17
LiCGa	7.656	4.09	1.39	0.27	179.9	199.0	176.7	0.26
$\dagger\text{NaCGa}$	72.234	2.75	-0.40	0.19	-98.2	163.8	-113.5	-
CuCGa	27.299	6.04	0.99	2.41	47.5	109.1	89.3	0.45
NaSiGa	18.178	1.22	0.26	0.24	85.5	91.4	85.5	0.18
$\dagger\text{BeMgC}$	139.763	3.91	-0.21	0.16	-130.5	263.1	-163.1	-
$\dagger\text{BeCaC}$	25.881	1.91	-1.43	0.14	-253.3	94.0	-257.1	-
$\dagger\text{BeZnC}$	570.453	4.09	-0.07	0.84	-52.9	144.5	-35.0	-
$\dagger\text{BeSrSi}$	7.216	1.33	-0.23	0.11	-83.6	100.4	-64.4	-
$\dagger\text{BeCdC}$	29.317	2.71	-5.21	0.79	-195.0	-60.3	-189.8	-
$\dagger\text{BeBaSi}$	5.601	1.10	-0.39	0.09	-98.6	68.7	-85.1	-
$\dagger\text{BeBaGe}$	9.992	1.03	-0.32	0.09	-80.8	67.9	-68.6	-
$\dagger\text{BeBaSn}$	54.671	1.02	-0.17	0.07	-50.1	79.5	-39.0	-
$\dagger\text{MgCaC}$	196.206	1.68	-0.09	0.09	-79.0	169.5	-96.5	-
MgCaSi	43.998	0.92	0.19	0.19	91.7	113.5	82.6	0.43

Continued on next page

Table A.2 – continued from previous page

ABC	d_{14} (pC/N)	C_{11}	C_{44} (10^{11} Pa)	C_{12}	$\omega_{\min}^{(X)}$	$\omega_{\min}^{(X)}$ (cm^{-1})	$\omega_{\min}^{(X)}$	k_{14}
MgCaGe	42.563	0.89	0.19	0.18	80.4	86.2	74.1	0.41
MgCaSn	32.615	0.69	0.19	0.20	67.2	60.1	66.9	0.31
MgCaPb	30.495	0.60	0.18	0.18	53.0	45.4	53.7	0.28
MgZnC	35.538	3.25	0.50	0.30	82.4	166.6	57.8	0.51
MgSrSi	280.394	0.81	0.04	0.17	38.2	84.4	32.7	0.80
MgSrGe	230.449	0.78	0.05	0.16	37.6	71.0	33.5	0.75
MgSrSn	127.153	0.60	0.07	0.17	41.0	53.0	40.1	0.58
†MgBaSi	177.367	0.68	-0.08	0.16	-41.5	61.8	-41.4	-
†MgBaSn	837.671	0.53	-0.01	0.16	7.0	44.2	10.6	-
†CaZnSi	260.605	1.19	-0.07	0.22	-53.8	109.6	-60.2	-
†CaZnGe	384.812	1.01	-0.04	0.20	-38.6	83.6	-45.5	-
CaSrSi	29.746	0.69	0.13	0.15	53.8	84.2	62.4	0.23
CaSrGe	33.937	0.66	0.12	0.14	49.4	70.8	58.7	0.25
CaSrSn	29.933	0.54	0.12	0.15	60.6	54.9	60.9	0.21
CaSrPb	35.650	0.49	0.11	0.13	48.2	41.7	47.4	0.24
CaCdSi	80.427	1.08	0.14	0.21	46.0	86.6	35.9	0.56
CaCdSn	46.454	0.78	0.17	0.23	51.6	56.1	47.4	0.36
CaBaSi	97.623	0.59	0.06	0.15	44.3	65.2	45.4	0.47
CaBaSn	84.006	0.47	0.07	0.15	46.7	47.0	45.4	0.42
SrCdSi	2878.781	0.85	0.01	0.20	-13.1	74.7	-18.9	0.97
BeScB	133.369	2.74	0.13	0.39	60.5	198.2	21.2	0.72
†BeYB	81.378	2.19	-0.29	0.33	-96.2	129.1	-94.7	-
MgScB	15.177	2.22	0.46	0.22	92.2	204.6	114.3	0.16
ScZnB	36.869	2.86	0.32	0.32	73.2	175.8	43.7	0.41
ScCdB	7.839	2.70	0.44	0.33	58.3	131.4	58.4	0.11
†ZnYB	201.930	2.63	-0.09	0.20	-53.4	152.6	-68.1	-
YCdB	64.798	2.42	0.16	0.21	24.5	127.8	-26.1	0.48
†CaBAl	154.976	1.83	-0.11	0.05	-80.0	178.6	-93.9	-
†SrBAl	60.742	1.54	-0.34	0.07	-103.0	120.2	-103.0	-
†CaBGa	83.977	1.79	-0.23	0.07	-83.4	125.6	-89.3	-
†SrBGa	51.970	1.48	-0.42	0.09	-95.1	95.9	-92.2	-
SrAlGa	1122.313	0.89	0.01	0.14	23.9	72.3	32.9	0.86
TiNiC	8.366	4.42	0.31	1.38	11.4	165.5	-79.1	0.08
TiNiSi	8.168	2.93	0.92	1.16	180.7	154.0	166.2	0.16
TiNiGe	6.595	2.60	0.96	1.20	154.6	139.5	153.2	0.13
TiNiSn	0.187	2.76	0.90	1.05	124.6	123.6	129.0	0.00
TiNiPb	22.128	1.87	0.41	0.97	57.4	68.5	61.0	0.25
TiPdSi	8.482	2.01	0.76	1.35	134.0	102.3	124.8	0.16
TiPdGe	7.244	2.06	0.75	1.34	129.0	93.5	121.6	0.13
TiPdSn	4.382	2.11	0.73	1.18	118.2	92.5	119.3	0.08

Continued on next page

Table A.2 – continued from previous page

ABC	d_{14} (pC/N)	C_{11}	C_{44} (10^{11} Pa)	C_{12}	$\omega_{\min}^{(X)}$	$\omega_{\min}^{(X)}$ (cm^{-1})	$\omega_{\min}^{(X)}$	k_{14}
TiPdPb	9.136	1.44	0.36	1.01	52.3	52.7	55.5	0.10
TiPtSi	5.766	2.62	0.94	1.48	121.8	97.0	115.6	0.13
TiPtGe	4.476	2.52	0.90	1.44	121.1	92.3	115.3	0.10
TiPtSn	0.708	2.63	0.94	1.30	122.1	93.1	120.9	0.02
TiPtPb	14.899	1.76	0.46	1.06	57.6	57.8	59.0	0.20
[†] NiZrC	2.804	4.04	-0.59	1.06	-109.6	119.9	-130.0	-
NiZrSi	26.401	2.55	0.51	1.11	92.3	108.8	82.5	0.38
NiZrGe	27.413	2.32	0.46	1.02	89.5	106.4	81.6	0.37
NiZrSn	13.658	2.45	0.67	0.94	104.4	114.3	101.3	0.22
NiZrPb	0.107	1.81	0.56	0.89	85.4	76.8	88.1	0.0
[†] NiHfC	10.972	4.17	-0.33	1.15	-79.7	107.4	-100.5	-
NiHfSi	20.423	2.57	0.64	1.20	85.6	90.4	77.6	0.34
NiHfGe	19.653	2.51	0.63	1.15	84.4	88.2	77.2	0.32
NiHfSn	10.905	2.51	0.79	1.00	97.8	99.3	93.1	0.19
NiHfPb	0.264	2.04	0.63	0.98	82.4	71.4	84.0	0.00
ZrPdSi	19.015	1.88	0.52	1.19	91.0	81.0	83.0	0.30
ZrPdGe	17.722	1.80	0.53	1.16	92.9	78.2	85.0	0.28
ZrPdSn	13.121	1.95	0.61	1.06	107.8	86.7	100.9	0.21
ZrPdPb	4.543	1.48	0.48	0.95	72.3	59.6	75.2	0.06
ZrPtSi	21.081	2.34	0.54	1.24	80.0	78.7	74.8	0.35
ZrPtGe	17.721	2.23	0.56	1.21	84.0	78.2	79.1	0.30
ZrPtSn	9.311	2.42	0.74	1.14	103.4	86.7	97.8	0.19
ZrPtPb	0.700	1.79	0.56	0.99	74.5	63.1	75.7	0.01
PdHfSi	15.673	1.99	0.63	1.28	84.8	70.5	77.8	0.28
PdHfGe	15.356	1.89	0.62	1.24	85.7	67.9	78.8	0.26
PdHfSn	10.814	2.07	0.71	1.13	98.4	77.7	91.0	0.19
PdHfPb	5.631	1.53	0.49	0.99	70.0	54.8	74.2	0.08
HfPtSi	15.496	2.47	0.68	1.33	82.8	74.1	77.7	0.30
HfPtGe	13.933	2.35	0.69	1.30	85.6	73.0	80.6	0.27
HfPtSn	7.312	2.57	0.85	1.21	101.3	81.5	95.7	0.16
HfPtPb	0.368	1.86	0.58	1.04	72.6	60.4	74.8	0.01
ScNiP	34.069	1.99	0.30	0.95	81.7	107.4	85.1	0.41
ScNiAs	20.450	2.11	0.45	0.89	99.3	112.6	100.2	0.30
ScNiSb	12.575	2.58	0.70	0.80	110.0	120.5	107.6	0.23
ScNiBi	4.126	1.83	0.57	0.71	88.7	80.7	89.0	0.06
ScPdP	5.430	1.90	0.25	0.90	57.7	87.8	44.8	0.06
ScPdAs	17.375	1.53	0.47	1.02	93.5	72.4	91.2	0.23
ScPdSb	10.863	1.76	0.59	0.90	114.6	85.3	110.7	0.19
ScPtSb	9.872	2.27	0.72	0.97	102.8	84.9	99.7	0.19
[†] NiYAs	31.119	1.57	-0.24	0.69	-57.1	57.2	-46.0	-

Continued on next page

Table A.2 – continued from previous page

ABC	d_{14} (pC/N)	C_{11}	C_{44} (10^{11} Pa)	C_{12}	$\omega_{\min}^{(X)}$	$\omega_{\min}^{(X)}$ (cm^{-1})	$\omega_{\min}^{(X)}$	k_{14}
<u>NiYSb</u>	242.272	1.68	0.05	0.57	15.2	88.6	13.8	0.77
<u>†YPdP</u>	26.924	1.65	-0.23	0.68	-63.1	60.7	-69.1	-
<u>YPdSb</u>	32.978	1.43	0.25	0.69	55.0	67.2	55.4	0.35
<u>YPtSb</u>	58.165	1.81	0.21	0.72	41.8	64.5	41.0	0.50

Curriculum Vita

Anindya Roy

- 2008 - 2011** Graduate Assistant, Department of Physics and Astronomy,
Rutgers University
- 2006 - 2008** Teaching Assistant, Department of Physics and Astronomy,
Rutgers University
- 2006** MSc in Physics, Indian Institute of Technology Bombay, India
- 2004** BSc in Physics, Jadavpur University, Kolkata, India

Publications

- Roy A., Bennett J. W., Rabe K. M., Vanderbilt D., “Half-Heusler semiconductors as piezoelectrics”, arXiv:1107.5078v1, submitted to Phys. Rev. Lett.
- Roy A., Vanderbilt D., “Theory of prospective perovskite ferroelectrics with double rocksalt order”, Phys. Rev. B. **83**, 134116 (2011), arXiv:1012.5070v1
- Roy A., Stengel M., Vanderbilt D., “First-principles study of high-field piezoelectricity in tetragonal PbTiO_3 ”, Phys. Rev. B **81**, 014102 (2010), arXiv:0910.0271v1